UNIVERSITÀ DEGLI STUDI DI TORINO

Dipartimento di Biotecnologie Molecolari e Scienze per la Salute

Ph.D. Program in Biomedical Sciences and Oncology

Cycle XXXII

Academic Years 2016-2020

Elucidating the role of Phosphoinositide 3-Kinase-C2-Alpha in vesicular trafficking as well as in modulating glucose homeostasis

Candidate: Abhishek Derle

Supervisor: Prof. Emilio Hirsch

PhD coordinator: Prof. Emilio Hirsch

Index

Abstract

PI3K signalling axis is involved in several processes such as proliferation, survival and metabolism. Emerging evidences highlight the involvement of class II enzymes in a multitude of different signalling pathways however their specific function in the cell is still unclear. Recent genetic and biochemical studies have pointed out the non-redundant roles of α isoform of class II PI3Ks (PI3K-C2α), which produces PtdIns3P and PtdIns(3,4)P2, critical regulators of membrane dynamics and vesicular trafficking. To be effective, these trafficking routes requires regulated recruitment of membrane tethers, lipid kinases and phosphatases in time and space. Accordingly, directional transport of recycling cargo from early endosomes (EE) to the endocytic recycling compartment (ERC) relies on PtdIns(3)*P* hydrolysis and activation of the small GTPase Rab11. However, how these events are coordinated is yet unclear. By using a novel genetically-encoded FRET biosensor for Rab11, we report that generation of endosomal PtdIns(3)*P* by PI3K-C2α controls the activation of Rab11. Active Rab11, in turn, prompts the recruitment of the phosphatidylinositol 3-phosphatase myotubularin 1 (MTM1), eventually enabling the release of recycling cargo from the EE and its delivery toward the ERC. Our findings thus define that delivery of recycling cargo toward the ERC requires spatial and sequential coupling of Rab11 activity with PtdIns(3)*P* turnover.

On the other hand, to evaluate the organismal role of PI3KC2α, various mouse models have been generated till date. All of these mouse models were either developed using gene trap technique, which still expressed a truncated version of the protein or exhibited embryonic lethality after a whole body homozygous inactivation of the whole protein or its kinase dead mutant. Therefore, in the present study, in order to bypass this hurdle of embryonic lethality and to appreciate the role of PI3KC2α in postnatal physiology at organismal level, we systemically targeted its expression in adult mice. CAGGCre-ER mice, carrying a tamoxifen-inducible Cre recombinase, were crossed with *Pi3kc2a*$^{fl/fl}$ mice. The systemic deletion of PI3K-C2α strongly impaired the survival of *Pi3kc2a*$^{fl/fl}$*Cre*$^{+}$ (KO) mice. We demonstrated that our KO mice exhibited severe hepatic damage and hypoketotic hypoglycemia due to defects in endogenous glucose production and mitochondrial fatty acid β-oxidation.

Introduction

Phosphatidylinositol 3-kinases (PI3Ks) are a conserved family of lipid kinases that, by generating 3' phosphorylated phosphoinositides as intracellular secondary messengers, regulate several biological processes including intracellular signal transduction and vesicular trafficking pathways (Bhattacharya et al., 2016; Vanhaesebroeck et al., 2010). Eight PI3K isoforms have been identified in mammals and they are now grouped into three classes according to their primary structure and *in vitro* substrate specificity. Class I PI3K isoforms (p110α, p110β, p110γ, p110δ), following stimulation, transiently generate phosphatidylinositol 3,4,5-triphosphate on intracellular membranes, subsequently recruiting signaling molecules including AKT. Through its downstream effectors, AKT plays an important role in regulating several signaling cascades that control critical cellular functions, such as cell growth, motility, survival and metabolism. Its imbalance can lead to development of various diseases such as cancer, inflammation, autoimmunity, with emerging potential roles in metabolic and cardiovascular disorders (Fruman et al., 2017; Vanhaesebroeck et al., 2016). In contrast to Class I PI3Ks, which have been extensively studied thus far for their role in normal physiology and diseases, Class II PI3Ks functions are recently emerging. The three enzymes of Class II i.e., PI3K-C2α, PI3K-C2β, and PI3K-C2γ are monomers of high molecular weight ranging from 166 to 190 kDa due to their extended N- and C- terminal arms. Multiple protein and lipid binding domains present in these terminal arms facilitate their multi-molecular association as well as their targeting to various intracellular membranes (Falasca and Maffucci, 2012).

Class II PI3Ks show a broad expression pattern, where PI3K-C2α and PI3K-C2β are almost ubiquitously expressed while PI3K-C2γ expression is restricted to liver, pancreas and kidney (Braccini et al., 2015b; El Sheikh et al., 2003). Similar to Class I PI3Ks, they possess a Ras binding domain and a PI3K catalytic core, however, they lack the obligatory regulatory subunit. Structurally, PI3KC2α shares clathrin-binding and coiled-coil domains in the N-terminal segment with PI3K-C2β, but not with PI3K-C2γ. However, the C-terminus extensions are more conserved between all class II isoforms and invariably contain a PX domain (Phox homology domain) and a second C2 domain. Data suggests that Class II PI3Ks can be activated by wide range of stimuli, such as growth factors, RTKs, GPCRs and adhesion molecules (Falasca and Maffucci, 2012; Jean and Kiger, 2014). However, the precise mechanism by which these enzyme associate with these upstream signals which, in turn, stimulate their lipid kinase activity *in vivo* still remains unclear. These isoforms generate distinct lipid products by phosphorylating the D3

position of inositol ring of phosphatidylinositol (PtdIns) and thereby activating different downstream effectors. *In-vitro* studies have implicated that Class II PI3Ks produce both PtdIns(3)*P* and PtdIns(3,4)*P2* on these spatially defined intracellular compartments, with PtdIns being the most preferential substrate. By converting PtdIns lipid to PtdIns(3)*P* on endosomal and autophagic membranes, the class II isoforms lead to recruitment as well as activation of effector proteins containing FYVE or PX lipid-binding domains. Moreover, by converting PtdIns(4)*P* to PtdIns(3,4)*P*2, they co-ordinate the localization of effector proteins containing the PH domain (Nigorikawa et al., 2014; Schink et al., 2016). Through these lipid products, Class II enzymes have been involved in regulating multiple intracellular membrane trafficking events including endocytosis, recycling and exocytosis (Bilanges and Posor, 2019; Campa et al., 2015; Gulluni et al., 2019; Mazza and Maffucci, 2011).

Particularly, recent genetic and biochemical studies have revealed non-redundant roles of the α isoform of class II PI3Ks in regulating these membrane trafficking events through production of PtdIns(3)*P* and PtdIns(3,4)*P*2 in specific subcellular compartments. At plasma membrane, PI3K-C2α act as a crucial mediator of clathrin-mediated endocytosis, via production of PtdIns(3,4)*P*2 on clathrin coated pits. This event promotes recruiting the machinery necessary for clathrin dissociation and maturation of vesicles into early endosomes (Posor et al., 2013). PI3K-C2α has also been found to be required for proper assembly and function of the primary cilium by producing PtdIns(3)*P* pool on pericentriolar recycling endosomes (PRE) at the base of primary cilium which, in turn, activates the small GTPase Rab11(Franco et al., 2014b). On the other hand, PI3K-C2α is also involved in exocytic pathways by controlling clathrin vesicle formation and stability in secretory vesicles formed at golgi (Gaidarov et al., 2001; Gaidarov et al., 2005). In flies, the only class II homologue, Pi3k68D is important for PtdIns3*P* production on endosomal compartment and thereby regulating the sorting of vesicles from endocytic compartment to the plasma membrane (Velichkova et al., 2010b). Similarly, in human endothelial cells (HUVEC), PI3K-C2α promotes sorting of endosomal vesicles towards the plasma membrane via regulation of PtdIns(3)*P*. This process is required for RhoA dependent targeting of VE-cadherin to tight junctions (Yoshioka et al., 2012). Accordingly, down-regulation of PI3K-C2α induces reduction of PtdIns(3,4)*P*2 and PtdIns(3)*P* levels in the cells which, in turn, leads to dysfunctions in endocytic signaling routes as well as defects in maturation, sorting and motility of endosomal membranes, respectively (Falasca et al., 2007;

Schink et al., 2013). These broad alterations underline critical role of PI3K-C2α in vesicular trafficking.

PI3K-C2α in vesicular trafficking

Intracellular trafficking of endocytosed molecules ensures the delivery of plasma membrane components and receptor-associated ligands to several cellular compartments. After internalization, such molecules can be either degraded or re-used by returning to the plasma membrane (Maxfield and McGraw, 2004). This recycling pathway restores the composition of plasma membrane and is mediated by vesicular carriers that transfer endocytosed material from peripherally located early endosomes (PE) to the endocytic recycling compartment (ERC), a juxtanuclear tubulovesicular compartment (Cullen, 2008; Jovic et al., 2010; Mellman and Nelson, 2008). To be effective, this transport route requires regulated recruitment of molecular motors, membrane tethers, as well as lipid kinases and phosphatases in time and space(Franco et al., 2014a; Franco et al., 2016; Horgan et al., 2010a, b; Jovic et al., 2014; Ketel et al., 2016; Takahashi et al., 2012; Winter et al., 2012). Such engagement is partly accomplished by key determinants of functional identity of organelles including phosphatidylinositol 3-phosphate (PtdIns(3)*P*) and the small GTPase Rab11 (Franco et al., 2014a; Ren et al., 1998; Sonnichsen et al., 2000; Traer et al., 2007; Ullrich et al., 1996).

PtdIns(3)*P* is the major phosphoinositide residing on early endosomes where it serves as a membrane recognition site for the recruitment of proteins, thereby mediating endosomal fusion and maturation (Balla, 2013; Simonsen et al., 1998). PtdIns(3)*P* homeostasis is controlled by the coordinated action of lipid kinases and phosphatases. In particular, while phosphorylation of (PtdIns) to PtdIns(3)*P* requires members of the class II and class III phosphatidylinositol 3-kinase (PI3K) enzymes(Backer, 2008; Braccini et al., 2015a; Campa et al., 2015; Franco et al., 2016), termination of PtdIns(3)*P* signaling relies on Myotubularins (MTMs), lipid phosphatases that convert PtdIns(3)*P* to (PtdIns) (Cao et al., 2008; Cao et al., 2007; Hnia et al., 2012; Jean et al., 2012). Although endosome maturation and recycling of endocytosed cargos requires control of PtdIns(3)*P* levels by the action of lipid kinases and phosphatases (Jean et al., 2012; Ketel et al., 2016; Velichkova et al., 2010a), the mechanism responsible for the regulated recruitment of these lipid metabolizing enzymes on endosomes remains largely unknown.

Extensive investigations demonstrated that members of the Rab protein family are coordinators of membrane domain formation and vesicle trafficking dynamics controlling the recruitment of endocytic regulators such as lipid kinases or phosphatases (Wandinger-Ness and Zerial, 2014). In particular, trafficking of endocytosed cargos toward the ERC is mediated by Rab11, a small GTPase enriched on ERC membranes and activated by signaling downstream of PI3K-C2α-derived PtdIns(3)*P* pool (Campa et al., 2015; Campa and Hirsch, 2017; Franco et al., 2014a; Franco et al., 2016). In its active GTP-bound form, Rab11 mediates recycling and sorting of endocytosed membrane components through the ERC(Horgan et al., 2010b; Lu et al., 2015; Ren et al., 1998; Ullrich et al., 1996). However, whether the changes in Rab11 activity might determine the efficiency of membrane trafficking by controlling the phosphoinositide composition of endosomes is still unclear.

To monitor changes in Rab11 activity in living cells we developed a genetically-encoded FRET biosensor of active Rab11 named Activation Sensor Rab11 (AS-Rab11). Using this biosensor, we demonstrated that the increase in Rab11 activity on PtdIns(3)P^+ peripheral endosomes is important to control the release of recycling cargoes, via a circuit involving sequential clathrin/PI3K-C2α-mediated PtdIns(3)*P* burst and subsequent Rab11/MTM1-dependent PtdIns(3)*P* hydrolysis.

PI3K-C2α in glucose homeostasis

Apart from its role in regulating intracellular trafficking, several cell based and *in-vivo* studies has established the importance of PI3KC2α in regulating various cell biological as well as organismal functions. For instance, in pancreatic β cells, PI3KC2α depletion impairs glucose stimulated insulin release as well as insulin granule exocytosis (Dominguez et al., 2011; Leibiger et al., 2010). At the same time, it also allows the β cells to switch from glucose responsive differentiated state to a proliferative state by rerouting the signaling cascade (Leibiger et al., 2015). In addition to these cell type specific roles, PI3KC2α is also involved in performing generic cell biological functions across several cell types. For example, it has been demonstrated that PI3KC2α, apart from responding to insulin stimulation, contributes to insulin stimulated GLUT4 translocation to plasma membrane and subsequent glucose uptake (Falasca et al., 2007) (Brown et al., 1999). Down-regulation of PI3KC2α also leads to defects in neurosecretory

granule release and autophagy in adrenal glands and human bone osteosarcoma epithelial cells, respectively (Merrill et al., 2017; Meunier et al., 2005). Moreover, PI3KC2α exerts its protein scaffolding activity in stabilizing mitotic spindle assembly by simultaneously interacting with a microtubule associated protein TACC3 and clathrin (Gulluni et al., 2017b).

On the other hand, in order to evaluate the organismal roles of PI3KC2α, various mouse models have been generated till date. The first models, developed using a gene trap mutagenesis technique, were incomplete knock-outs as they still expressed a truncated version of the protein (Harris et al., 2011; Mountford et al., 2015). In other two models, homozygous inactivation of PI3KC2α has resulted in embryonic lethality around embryonic day 10.5 to 11.5, with multiple defects underlying this phenotype. These embryos show defects is angiogenesis as well as in primary ciliary elongation and function (Franco et al., 2014b; Yoshioka et al., 2012). On the other hand, the heterozygous deletion impairs platelet function with delay in thrombus formation. Additionally, mouse model with homozygous inactivation of kinase activity shows embryonic lethality, while the heterozygous mice show hypothalamic leptin resistance and glucose intolerance at an old age (Alliouachene et al., 2016). All of these mouse models were either developed using gene trap technique, which still expressed a truncated version of the protein or exhibited embryonic lethality after a whole body homozygous inactivation of the whole protein or its kinase dead mutant. Therefore, in the present study, in order to bypass this hurdle of embryonic lethality and to appreciate the role of PI3KC2α in postnatal physiology at organismal level, we decided to generate a tamoxifen inducible, conditional PI3KC2α knock-out mouse model using knock-out first strategy. Using these mice, homozygous inactivation of PI3KC2α was possible at any developmental stage of choice by deleting the target exon using the Cre/lox system.

Previous reports have demonstrated the roles of other class II isoforms in glucose metabolism. PI3K-C2β kinase dead mice show enhanced insulin sensitivity and glucose tolerance in metabolic tissues. On the other hand, PI3K-C2γ inhibition leads to selective reduction of Akt2 activity in liver which specifically inhibits liver glycogen accumulation and initiates development of hyperlipidemia and insulin resistance with age (Alliouachene et al., 2015; Braccini et al., 2015b). Apart from this, given the involvement of PI3KC2α in insulin signaling (Brown et al., 1999; Ursø et al., 1999), we focused our initial characterization on accessing these

conditional knock-out mice for systemic glucose homeostasis. Although these mice exhibited defect in glucose homeostasis, no significant changes in organismal glucose and insulin tolerance were observed. However, we noticed that homozygous inactivation of PI3KC2α resulted in hepatic damage and hypoketotic hypoglycemia due to defects in endogenous glucose production and mitochondrial fatty acid β-oxidation.

Chapter I

Elucidating the role of PI3K-C2α in vesicular trafficking

Materials and Methods

Antibodies

The following antibodies were used in this study: mouse-anti-PI3K-C2α (BD Biosciences 611046, western blotting (WB) 1:500), mouse-anti-Rab11 (BD Biosciences 610656, WB 1:1000), rabbit-anti-MTM1 (SIGMA HPA010008, WB 1:1000), mouse-anti-FLAG (SIGMA clone M2, WB 1:2000), mouse-anti-GFP (ABCAM ab127417, WB 1:1000), rabbit-anti-VPS34 (Novus Biologicals NB110-87320SS, WB 1:1000), mouse-anti-MTMR4 (Santa Cruz sc-373922, WB 1:500), mouse-anti-MTMR6 (ABCAM ab69875, WB 1:1000), mouse-anti-MTMR9 (Santa Cruz sc-514366, WB 1:1000), rabbit-anti-FIP2 (ABCAM ab76892, WB 1:1000), rabbit-anti-FIP4 (Biorbyt orb215321, WB 1:1000). Anti-mouse IgG (ab131368, WB 1:5000) Anti-Rabbit IgG (A0545 SIGMA, 1:5000). anti mouse/rabbit IgG Alexa fluor 488/568 (IF 1:1000).

SiRNA and plasmid transfection

All siRNAs used in this study were 21-, 23-, or 27-base oligonucleotides including 3′-dTdT overhangs. For silencing, the following siRNAs were used targeting the human isoform: PI3K-C2α 5'-GGCAAGATATGTTAGCTTT-3', MTM1 5'-GATGCAAGACCCAGCGTAA-3′. The scrambled control siRNA used throughout this study corresponded to the sequence 5'-ATGAGTTAGATGCGTTCTA-3'.

COS-7 cells were transfected with siRNA using Lipofectamin 2000 (Invitrogen) according to the manufacturer's protocol. To achieve optimal knockdown efficiency, two rounds of silencing were performed. Cells were transfected on day 1, expanded on day 2, seeded for the experiment on day 3, and the experiment was performed on day 4.

For transient overexpression of proteins in silenced cells, plasmids were transfected on day 4 12 h before analysis using Lipofectamin 2000 (Invitrogen). For transient overexpression of proteins in untreated cells, plasmids were transfected 12 h before analysis using Lipofectamin 2000 (Invitrogen).

Recombinant protein production

GST-Rab11a recombinant protein was generated by cloning Rab11a cdna in pGex vector. Protein expression was induced by addition of isopropyl β-D–thiogalactoside (IPTG, 0.1 mM) at room temperature for 6 hours.

Recombinant proteins (GST-Rab11a, GST-Rab5a, GST-Rab7a) were purified (elution 10 mM glutathione, PBS), dialyzed, frozen in liquid nitrogen, and stocked (50% glycerol in Tris-HCl 50 mM 5 mM MgCl2, 100 mM NaCl) at −80°C. His-Flag-tagged MTM1 was generated according to previously established protocol (Hnia et al., 2012). In brief, Flagged MTM1 was clone in Pqe vector and bacteria were grown in 2X-YT (1% Yeast extract, 221 1% bactotryptone, 2,5mM NaOH and 0.5% NaCl) enriched medium until mid-log phase. Induction was performed with 1mM IPTG at 16°C for 12 hr. Soluble protein fraction was purified, dyalized, and stocked (50% glycerol in Tris-HCl 50 mM 5 mM MgCl2, 100 mM NaCl, 0.5% Triton).

Plasmids

The biosensor was built in sequential cloning steps using monomeric version of fluorescent proteins (A206K mutation) to avoid signal artifacts during FRET quantitation caused by multimerization of biosensor molecules into limited diffusional space, such as in membrane and vesicular compartments. Rab11 binding domain (RBD11) was fused with RBD11-circularly permutated Venus (mcpVenus) at residue 195, while cyan fluorescent protein (mECFP)-Rab11a fusions were first constructed. Two repetition of a linker encoding for a 17-mer unstructured soluble and proteinase-K sensitive polypeptide (GSTSGSGKPGSGEGSTK) (Whitlow et al., 1993) was then cloned by PCR that allow to maximize the FRET change between the active and inactive state. To construct RBD11-cpVenus, polymerase chain reaction (PCR) was used to amplify amino-acids 649-756 of FIP3 using the primers: 5'–CTAGCTAGCATGGGCCTGCAGGAGTACCACA–3' and 5'–GCTCTAGAATGGGCACCCGCGACG–3', and pGEX- FIP3 RBD11 as a template (Franco et al., 2014a). mcpVenus was amplified using the primers: 5'–GGTAGTGGTGAATTCATGCTCGGAGCAGTCCTGA–3' and 5'–ATCCCCTCGAGAGCACGGGGCCGTCGCCGAT–3' using ICUE3 FRET probe (DiPilato and Zhang, 2009) as a template. Both fragments were then digested, gel purified, and subcloned in PGEM 3tEasy vector (Promega). The resulting fragment contained, from the 5'-end: a NheI site, RBD11, a EcoRI site, a linker (GGSG), and mcpVenus. This was cloned. To construct mECFP-Rab11a, a construct encoding mECFP was amplified with the primers: 5'–AAGCGGCCGCATGGTGAGCAAGGGCGAGGAGCTG–3' and 5'–GGTGCCCATTCTAGAAGTTCCCACGGGGGTACCAGCCTTGTACAGCTCGT–3'. Rab11a

was amplified with the primers: 5'–GCTCTAGAATGGGCACCCGCGACG–3' and 5'–GCGGATCCAATGCCTTAGATGTTCTGACAGCACTGC–3' using a Rab11a expression construct as a template. Both fragments were then digested gel purified and subcloned in PGEM 3tEasy vector (Promega). The resulting fragment contained, from the 5'-end: a NotI site, a mECFP, a linker (GTPVGT), XbaI site, Rab11a and a BamHI site. In the next step, the 3' end of RBD11-mcpVenus was flanked with zero, one or two copies of a sequence encoding a 17-mer, (GSTSGSGKPGSGEGSTK) generated by polymerase chain reaction (PCR). For that purpose, seven annealed 5' phopsorilated oligos: 5'–TCGAGGGGAGGCAGC–3', 5'–GGCCGCTGCCTCCCC–3' and 5'-TCGAGGGGATCAACTTCAGGATCAGGAAAACCCGGCTCCGGCGAGGGATCAACTAAAAGC–3' and 5'–GGCCGCTTTTAGTTGATCCCTCGCCGGAGCCGGGTTTTCCTGATCCTGAAGTTGATCCCC–3' and 5'–TATATATATATATATACTCGAGGGATCAACTTCAGGATCAGGAAAACCCGGCTCCGGCGAGGG–3'and 5'–CCGGGCTTGCCGCTGCCGGAAGTAGAGCCTTTAGTTGATCCCTCGCCGGAGCCGGG–3' and 5'–TATATATATATGCGGCCGCTTTTAGTTGATCCTTCTCCTGATCCGGGCTTGCCGCTGCCG-3' that encode the linker sequence flanked at the 5' by a XhoI and at the 3' by a NotI restriction site were ligated and subcloned in PGEM 3tEasy vector (Promega). To assemble the biosensor all the subcloned fragments were digested with the single cutter enzyme inserted at 5' and 3'-end, gel purified and cloned in pcDNA3.1(-myc/His) vector (Invitrogen), thus originating the following fusion protein containing from the N-terminus RBD11-cpVenu-2x17-mer linker-mECFP-Rab11a. The constructs were fully sequenced to ensure fidelity of the PCR reactions. Constituvely active (AS-Rab11^{Q70L}), dominant negative (AS-Rab11^{S25N}), a second constitutive active form (AS-Rab11^{S20V}) , an RBD mutant (AS-Rab11$^{RBD\ mutant}$ in which the "RBD domain" of FIP3 carries a 3 aminoacids mutation abrogating binding of active Rab11)(Eathiraj et al., 2006), a nucleotide free form (AS-Rab11^{N124I}) and a mutant lacking GDI interaction (AS-Rab11^{N206X}, in which Asn-206 was changed to a stop codon, eliminating Rab11 prenylation/GDI binding site) versions of this biosensor were then engineered by site directed mutagenesis (Quikchange kit, Stratagene) using the following primers: 5'-GATATGGGACACAGCAGGGCTAGAGCGATATCGAGC-3', 5'-

GCTCGATATCGCTCTAGCCCTGCTGTGTCCCATATC-3’ and 5’-GATTCTGGTGTTGGAAAGAATAATCTCCTGTCTCG-3’, 5’-CGAGACAGGAGATTATTCTTTCCAACACCAGAATC-3’ and 5’-GTTGTCCTTATTGGAGATGTTGGTGTTGGAAAGAGTA-3’, 5’-TACTCTTTCCAACACCAACATCTCCAATAAGGACAAC-3’ and 5’-CAACTTCCGCCTGCAGGACGCCGCCGCCAGGATCATCGTGGCCATCAT-3’, 5’-ATGATGGCCACGATGATCCTGGCGGCGGCGTCCTGCAGGCGGAAGTTG-3’ and 5’-GTTATCATGCTTGTGGGCATTAAGAGTGATCTACGTCATCTC-3’, 5’-GAGATGACGTAGATCACTCTTAATGCCCACAAGCATGATAAC-3’ and 5’-ATGTTCCACCAACCACTGAATAAAAGCCAAAGGTGCAGTGCTG-3’, 5’-CAGCACTGCACCTTTGGCTTTTATTCAGTGGTTGGTGGAACAT-3’. Red fluorescent tagged version of Rab5, Rab4, Rab11 and Rab7 was generated by PCR and cloned into pmRFP-c1 plasmid.

The plasmid encoding RabGDI and GST-Rab7 were kindly provided by Cecilia Bucci from University of Salento. To allow the expression in mammalian cells the DNA sequence ecoding RabGDI and flanked by EcoRI site at 5’ –end and BamHI site at 3’-end was subcloned in pcDNA3.1(-myc/His) vector (Invitrogen). A FLAG tag (DYKDDDDK) was inserted by digestion of pcDNA3.1(-myc/His)-RabGDI with EcoRI followed by calf intestinal phosphatase (CIP) treatment and gel purification. The opened plasmid was ligated with a linker sequence encoding the FLAG epitope obtained by annealing two 5’phosphorylated oligos with the following sequence: 5’–AATTCATGGACTACAAAGACGATGACGACAAGC-3’ and 5’–AATTGCTTGTCGTCATCGTCTTTGTAGTCCATG–3’. The plasmid encoding hSH3BP5 was kindly gifted by Ken Sato from University of Gunma. A FLAG- N-terminal tag was added by PCR and the product of this reaction was cloned in pcDNA3.1(-myc/His) vector, thus generating a FLAG-hSH3BP5. The plasmid encoding TBC1D9B was kindly provided by Gerard Apodaca from University of Pittsburgh. A FLAG- N-terminal tag was added by PCR and the product of this reaction was cloned in pcDNA3.1(-myc/His) vector, thus generating a FLAG-TBC1D9B. The plasmid encoding mCherry-FYVE(2X) (pCI-neo-mCh-2XFYVE) was kindly gift by Matteo Bonazzi from University of Montpellier. The plasmid encoding TIAM1 was kindly gifted by Giorgio Scita and Andrea Palamidessi from IFOM in Milan. The plasmid encoding Rabex-5 was

kindly gifted by Sara Sigismund from IFOM in Milan. The plasmid encoding RN-3 was kindly gifted by Letizia Lanzetti from IRCC in Candiolo.

Fluorometry assay

$2*10^5$ HEK 293T cells were plated in a 6-well plate and transfected using Lipofectamine 2000 (Invitrogen) according to manufacturer's instructions. In experiments in which the biosensor was co-transfected with a negative or positive regulator, the biosensor/regulator DNA ratio was 1/4. The total amount of transfected DNA was kept to 500 ng. 36 hours post-transfection, cells were lysed in lysis buffer (50 mM Tris-HCl, pH 7.4, 10 mM MgCl2, 100 mM NaCl, 1% Tritorn X-100, proteinase inhibitors) and clarified lysate was placed in a fluorometer cuvette. The lysates were analyzed using a Fluoromax-4 Horiba fluorometer. The lysates were excited at 433 nm and an emission scan was acquired from 450 to 550 nm. To normalize for biosensor concentration a second measurement was made by directly exciting YFP at 505 nm and measuring its emission at 525 nm.

Immunoprecipitation assay for interaction of AS-Rab11 with SH3BP5 or AS-Rab11 with TBC1D9B

HEK 293T cells growing in 10-cm dishes were transfected with DNA mixtures containing 10 µg of pcDNA3.1(-myc/His)-Flag- SH3BP5 or 10 µg of pcDNA3.1(-myc/His)-AS-Rab11 or both, using calcium phosphate method. 48 h after transfection, cultures were harvested and homogenized in 0.5 ml of lysis buffer (50 mM Tris-HCl, pH 7.4, 0.2 mM GDP, 10 mM $MgCl_2$, 100 mM NaCl, 1% Tritorn X-100, 50 mM sodium fluoride, 1 mM phenylmethylsulfonyl fluoride). Cytosol was obtained by centrifuging the lysates at 20,000g for 30 min at 4 °C and protein concentration was determined by Bradford method. 1 mg of cytosol was incubated with FLAG M2 antibody (SIGMA, S.Louis, Missouri, USA) or with 1 µg of anti-GFP antibody (ABCAM, Cambridge, UK) for 2 hours and incubated on a rotating rack for 1 hour at 4 °C with Protein-G sepharose beads (GE, Buckinghamshire, UK). Samples were collected by centrifugation and washed six-times with phosphate wash buffer (10 mM NaH_2Po_4, 137 mM NaCl, and 2.7 mM KCl). Bound FLAG-SH3BP5, FLAG-TBC1D9B or GFP-AS-Rab11 protein complexes were then eluted by adding Laemmli sample buffer. SDS-PAGE and western blotting followed standard procedures. Similar approach was employed for the RabGAP TBC1D9B using the following lysis buffer: 50

mM Tris-HCl, pH 7.4, 0.2 mM GTP, 10 mM $MgCl_2$, 100 mM NaCl, 1% Triton X-100, 50 mM sodium fluoride, 1 mM phenylmethylsulfonyl fluoride).

Immunoprecipitation assay for interaction of AS-Rab11 with GDI

HEK 293T cells growing in 10-cm dishes were transfected with DNA mixtures containing 10 µg of pcDNA3.1(-myc/His)-Flag-RabGDI or 10 µg of pcDNA3.1(-myc/His)-AS-Rab11 or both, using calcium phosphate method. 48 h after transfection, cultures were harvested and gently homogenized in 0.5 ml of lysis buffer (50 mM Tris-HCl, pH 7.4, 0.2 mM GDP, 10 mM $MgCl_2$, 50 mM sodium fluoride, 1 mM phenylmethylsulfonyl fluoride). Cytosol was obtained by centrifuging the lysates at 20,000g for 30 min at 4 °C and protein concentration was determined by Bradford method. 1 mg of cytsol was incubated with FLAG M2 antibody (SIGMA, S.Louis, Missouri, USA) or with 1 µg of anti-GFP antibody (ABCAM, Cambridge, UK) for 2 hours and incubated on a rotating rack for 1 hour at 4 °C with Protein-G sepharose beads (GE, Buckinghamshire, UK). Samples was collected by centrifugation and washed six-times with phosphate wash buffer (10 mM NaH_2Po_4, 137 mM NaCl, and 2.7 mM KCl). Bound FLAG-GDI or GFP-AS-Rab11 protein complexes were then eluted by adding Laemmli sample buffer. SDS-PAGE and western blotting followed standard procedures.

Radiolabeling of intracellular nucleotides and identification of the nucleotide-bound forms of AS-Rab11.

HEK293T cells cultured in 6 well plate dishes and transfected for 48 h were radiolabeled for 4 h with ^{32}P (6.0 MBq per dish) in phosphate-free DMEM (Invitrogen, Cat. Number 11971025). The expression levels of AS-Rab11 proteins and mutant forms were assessed by immunoblot analysis with the anti-GFP antibody (ABCAM, Cambridge, UK). The labeled cells ($7x10^5$ cells) were lysed with 0.3 ml of an ice-cold solubilizing buffer consisting of 40 mM Tris–HCl (pH 7.5), 100 mM NaCl, 20 mM $MgCl_2$, 1 mM Na_3VO_4, 1 mM dithiothreitol, 1% (w/v) Triton X-100, and 2 µg/ml aprotinin and clarified. The precleared lysates were incubated with anti-GFP antibody-immobilized Protein G–Sepharose beads (GE Healthcare) at 4 C for 30 min. After extensive washing of the immunocomplexes, associated nucleotides were separated by thin layer chromatography and quantified with a Amersham Hyperfilm MP (GE Healthcare).

Guanine nucleotide exchange assay

HEK 293T cells growing in 10-cm dishes were transfected with DNA mixtures containing 10 µg of pEGFP-Rab11a or 10 µg of pcDNA3.1(-myc/His)-AS-Rab11, using calcium phosphate method. At 48 h after transfection, cultures were harvested and homogenized in 1 ml of lysis buffer (50 mM HEPES, pH 7.6, and 1% (v/v) Triton-x100, 100 mM NaCl, protease inhibitors). Cytosol was obtained by centrifuging the lysates at 20,000g for 20 min at 4 °C and protein concentration of clarified lysates was determined by Bradford method. 1 mg of protein was immunoprecipitated using 1 µg of anti-GFP antibody (ABCAM, Cambridge, UK) for 1 hours and incubated on a rotating rack for 1 hour at 4 °C with Protein-G sepharose beads (GE, Buckinghamshire, UK). Samples were collected by centrifugation and washed six-times with buffer A containing 50 mM HEPES, pH 7.6, 1 mM DTT and 20 mM EDTA and incubated for 20 min at 25 °C, to remove Mg^{2+} and nucleotide bound to the Rab11 GTPases. The treatments of the samples with buffer A were repeated three times more. To determine the GDP binding affinities to Rab11 GTPases, [3H]GDP at a specific activity of 6000 cpm/µM was incubated with the respective apo-GTPases at 25 °C for 1 h in buffer B containing 50 mM HEPES, pH 7.6, 100 mM NaCl, 2.5 mM $MgCl_2$ and 1 mM DTT. Samples were collected by centrifugation and washed six-times with buffer C containing 50 mM HEPES, pH 7.6, 100 mM NaCl, 10 mM $MgCl_2$ to stop the binding reaction, and the radionucleotides remaining bound to the Rab GTPases were quantified by scintillation counting. To measure the GDP/GTP exchange from Rab11 GTPases, the immunoprecipitated apo-GTPases were first complexed with [3H]GDP or in buffer B. After 60 min a binding equilibrium was reached, the dissociation reactions were initiated by the addition of 500 µM GTPγS to the incubation mixtures. At the indicated time intervals, samples were collected by centrifugation and washed six-times with buffer C to stop the exchange reaction. The radionucleotides remaining bound to the Rab GTPases were quantified by scintillation counting.

Rab11-activity pull down assay

Cells were washed in ice-cold PBS and lysed in 1 ml of MLB buffer (25 mM HEPES [pH 7.5], 150 mM NaCl, 1% Igepal CA-630, 10% glycerol, 25 mM NAF, 10 mM MgCl2, 1 mM EDTA, 1mM sodium orthovanadate, and protease inhibitor cocktail). Supernatant was collected after 15 min centrifugation at 13,000 rpm. A total of 1 mg of protein extract was incubated with 30 µg of recombinant protein coupled with glutathione S-transferase agarose (GE, Buckinghamshire, UK).

The reaction mixture was gently rocked for 1 hr at 4°C. Beads were washed four times with lysis buffer. Samples were resuspended in Laemmli buffer for SDS-PAGE and immunoblot analysis. Endogenous content of total Rab11 in cell lysates was measured by loading 50 μg of total extracts in a different gel followed by immunoblot and used to normalize measurements of active Rab11. For quantification analysis, pictures were taken ensuring that intensity was within the linear range and the Quantity One 1-D analysis software (Bio-Rad) was used.

Rab11-effectors pull-down assay

50 μg of GST-Rab11 and corresponding molar amount of GST recombinant proteins were coupled to with glutathione S-transferase agarose (GE, Buckinghamshire, UK) and gently rocked for 1 hr at 4°C. Samples were collected by centrifugation and washed six-times with buffer A containing 50 mM HEPES, pH 7.6, 1 mM DTT and 20 mM EDTA and incubated for 20 min at 25 °C, to remove Mg^{2+} and nucleotide bound to the Rab11 GTPases. The treatments of the samples with buffer A were repeated three more times. GDP or GTPγS was added at a final concentration of 2mM and incubated with the respective apo-GTPases at 25 °C for 1 h in buffer B containing 50 mM HEPES, pH 7.6, 100 mM NaCl, 2.5 mM $MgCl_2$ and 1 mM DTT. Samples were collected by centrifugation and washed six-times with buffer C containing 50 mM HEPES, pH 7.6, 100 mM NaCl, 10 mM $MgCl_2$ to stop the binding reaction. Proteins on beads were incubated with either 1 ml of cell lysate made from a confluent dish of COS-7 cells lysed in 1 ml of MLB buffer (25 mM HEPES [pH 7.5], 150 mM NaCl, 1% Igepal CA-630, 10% glycerol, 25 mM NAF, 10 mM MgCl2, 1 mM EDTA, 1mM sodium orthovanadate, and protease inhibitor cocktail), or with recombinant purified protein diluted in GST-binding buffer (20 mM Tris-HCl [pH 7.4], 100 mM NaCl, 5 mM MgCl2, 0.5% Triton X-100, 5 mg/ml BSA). After 1 hr, beads were washed with MLB or GST-binding buffer and proteins solubilized by boiling in LDS sample buffer.

Transferrin recycling assay

$2 * 10^5$ COS-7 cells were plated in a 6-well plate. After 24 hours, cells were starved for two hours in serum-free DMEM containing 0.1% BSA at 37°C, 5% CO_2, and then, where required, pretreated with 0.1% DMSO as control or with Vps34-IN1 1 uM for 30 min. 20 ug/ml of of alexa Fluor 647- conjugated human Transferrin (Invitrogen) were added for 30 min. After 37°C PBS washing, DMEM containing 0.1% BSA at 37°C, 5% CO_2 was added at various length times. Cells

were then washed twice with cold PBS and acid stripping solution (150 mM NaCl, 2 mM $CaCl_2$ and 25 mM CH_3COONa, pH 4.5) was added for 4 min. For FACS analysis cells were detached with PBS 0.5 mM EDTA and fixed in 4% paraformaldehyde for 10 min. After resuspension in PBS, fluorescence flow cytometry was performed using a FACScalibur instrument. 20,000 cells were collected for each sample. The MFI of the cell population was recorded for each time point. Data were normalized to the time 0 MFI. For immunofluorescence analysis, cells were fixed in 4% paraformaldehyde for 10 min and imaged by confocal microscopy.

Internal Transferrin quantitation

$2* 10^5$ COS-7 wild-type (or interfered) cells were plated in a 6-well plate. After 24 hours, cells were starved for two hours in serum-free DMEM containing 0.1% BSA at 37°C, 5% CO_2, and then, where required, pretreated with 0.001% DMSO as control or with Vps34-IN1 1 uM for 30 min. 20 ug/ml of alexa Fluor 647- conjugated human Transferrin (Invitrogen) were added for 30 minutes to allow continuous uptake and recycling of labelled ligands. Cells were then washed twice with cold PBS and acid stripping solution (150 mM NaCl, 2 mM $CaCl_2$ and 25 mM CH_3COONa, pH 4.5) was added for 4 min. Cells were detached with PBS 0.5 mM EDTA and fixed in 4% paraformaldehyde for 10 min. After resuspension in PBS, fluorescence flow cytometry was performed using a FACScalibur instrument. 20,000 cells were collected for each sample. The MFI of the cell population was recorded for each time point. Data were normalized to control MFI values. For immunofluorescence analysis, cells were fixed in 4% paraformaldehyde for 10 min and imaged by confocal microscopy.

Cell Imaging

Cells were grown on µ-Dish $^{35mm, high}$ imaging dishes (Ibidi). Imaging was performed in CO_2 independent medium, Dulbecco's modified Eagle's medium without fetal bovine serum (GIBCO). Time-lapse series were acquired at 37°C on an inverted confocal Leica SP8 microscope with AOBS, equipped with 40X O2/Oil immersion objective, NA 1.30. The temperature was controlled by a climate box covering the set up. Hyd detectors (Leica) allowed the simultaneous detection of mECFP and mcpVenus or/and mCherry/mRFP, respectively. Fluorescent dyes were imaged sequentially in frame-interlace mode to eliminate cross talk between the channels. mECFP was excited with a 458-nm laser line and imaged at 470–500-nm bandpass emission filters. mcpVenus

was exited with the 514-nm Argon laser line and imaged through a 525-550-nm bandpass emission filter. mCherry/mRFP was excited with the 568-nm Helium Neon laser line and imaged through a 580-650-nm bandpass emission filter. Alexa 647 dye was excited with the 633 nm Helium Neon laser line and imaged through a 650-700-nm bandpass emission filter. Serial sections were acquired satisfying the Nyquist criteria for sampling and processed using Matlab (MathWorks, MA, USA) and ICY software (http://icy.bioimageanalysis.org). Signals were referred to as individual structures if they comprised of a continuous patch of intensity values 50 (in a range of 0–255). At least two sections per cell were counted, ensuring that peripheral and perinuclear structures were equally taken into account. mECFP was bleached 5–10 times (2 s/scan) with zoom (x 15) with 100% laser power of the 458 nm Argon laser line. At the beginning of each experiment the number of bleaching steps that were sufficient to bleach mECFP was assessed and was kept constant all through. Acquisition was performed at zoom (x 11), in a region of 26 μm in side. The ROI has been chosen in order to contain the photobleached ERC and the surrounding intracellular region, and over a sufficiently large and homogeneous region to be able to visualize moving vesicles towards it. Exposure times and readout were fixed as follows: 200–300 ms for each channel followed by a 60-ms readout delay for the experiment in Figures 3a-f, i, 4b-g), resulting in timelapse sequences of roughly one frames per second. The timelapse sequences of roughly one frame per 30 seconds was used in Figures 3g, h, Supplementary Fig. 4a, 5a, b, d. Images obtained were merged and exported as a single TIFF file.

Image/video processing and data analysis

Image processing and analysis for total FRET activation in the cell were carried out with the Matlab software (MathWorks, MA, USA) integrated with Image Processing and Bioformats Toolbox. Following Gaussian smoothing, the image was converted to binary through thresholding, then median filtering, morphological closing and holes filling were applied to eliminate noisy pixels and smooth the images. The final mask was obtained computing the distance transform of the binary image and using it as the input for a Watershed transform, thus enabling to discriminate and separate different contiguous endosomes from one to another. The threshold mask was then applied to sensitized FRET and CFP images and background subtraction was performed according to previous published protocol (Broussard et al., 2013). Finally, FRET activity ratio was calculated by dividing the unsaturated sensitized FRET pixels by the CFP pixels (Jares-Erijman and Jovin,

2003; Kardash et al., 2011). To measure the dependence of FRET ratio on the distance from the nucleus, endosomes present in each frame included in the threshold mask were binned according to the distance of their centroid from the nuclear membrane.

Video processing and analysis for particle tracking and vesicle intensity profile were carried out with ImageJ, ICY (de Chaumont et al., 2012) and R studio. Following background subtraction and Gaussian smoothing the CFP, FRET sensitized, YFP and red fluorescence were treated to eliminate noisy pixels and smooth the images. The FRET ratio for each frame was computed by dividing FRET sensitized signal by CFP signal. The videos were then imported in ICY for spot detection and particle tracking procedure performed on the YFP signal (Chenouard et al., 2013). Intensity profile for FRET ratio, YFP and FYVE2X were exported together with trajectory for each detected vesicle. Vesicle intensity profiles were then aligned in R studio according to their speed profile and direction. The vesicle mean FRET ratio was adjusted by substracting cytoplasmic mean FRET ratio. MatLab code is fully available on GitHub.

Statistical analysis

For biochemichal, immunocytochemistry and microscopy-based experiments a minimum of three independent experiments (n) was performed and statistically significant estimates for each sample were obtained. For microscopy based quantification, cells were chosen arbitrarily according to the fluorescent signal in a separate channel, which was not used for quantification where it was possible. Values were presented as means ± SEM. *P* values were calculated using two-tailed Student's *t* test and one- or two-way ANOVA followed by Bonferroni's multiple comparison posttest (GraphPad Software). Statistical significance is indicated as follows: $*P < 0.05$, $**P < 0.01$, and $***P < 0.005$.

Results

Development of a Rab11 FRET biosensor.

The activation cycle of Rab11 is essential to mediate the delivery of internalized plasma membrane components from PE to ERC (Maxfield and McGraw, 2004; Welz et al., 2014). To monitor the spatial and temporal regulation of Rab11 nucleotide exchange in living cells, a genetically encoded fluorescence resonance energy transfer (FRET)-based probe, named Activation Sensor Rab11 (AS-Rab11), was developed (Figure 1a, Supplementary Figs.1a, b). The probe includes the C-terminal region of FIP3 binding active Rab11 only (Eathiraj et al., 2006), a circular permuted version of a modified monomeric yellow fluorescent protein (mcpVenus), a proteinase K-sensitive linker, a monomeric cyan fluorescent protein (mECFP) and human Rab11a (Figure 1a). In this probe design, an increase in GTP-loading of Rab11 promotes the binding of the C-terminal region of FIP3 to Rab11a, thus modifying the orientation of the two fluorophores and thereby increasing FRET which is represented by the 525 nm/475 nm (FRET/CFP) emission ratio (Miyawaki and Tsien, 2000; Pertz et al., 2006)(Figure 1a). The positioning of Rab11 at the C-terminal end of AS-Rab11 allows correct functioning of the Rab11 C-terminal sequences required for membrane insertion (Figure 1a).

To validate the efficiency of the biosensor energy transfer in the presence of either GDP or GTP, the fluorescence emission profiles of AS-Rab11 were monitored using a fluorometric assay (*see Materials and Methods*). In comparison with the wild type form, constitutively active mutant versions of Rab11 lacking GTPase activity (AS-Rab11^{Q70L} and AS-Rab11^{S20V}) showed decreased fluorescence emission intensity at 475 nm and a concomitant increase at 525nm (Figure 1b, Supplementary Fig. 1c red line). Consequently, the FRET/CFP ratio of AS-Rab11^{Q70L} and AS-Rab11^{S20V} were found significantly higher than the wild-type and the nucleotide-free (AS-Rab11^{N124I}) forms (Figure 1b, Supplementary Fig. 1c). In contrast, a dominant negative version of this biosensor (AS-Rab11^{S25N}, Supplementary Fig. 1c blue line) displayed 475 nm and associated 525nm emission higher and lower than the control, respectively (Figure 1b, Supplementary Fig. 1c cyan line, Supplementary Fig. 1d). A similar observation was made after proteinase-K treatment of AS-Rab11 wild-type (Supplementary Fig. 1c black line) that induced the cleavage of the amino acidic linker connecting the two fluorophores required to promote the energy transfer. Consequently, both AS-Rab11^{S25N} and proteinase-K-treated AS-Rab11^{wt} showed decreased FRET emission ratio (Figure 1b, Supplementary Fig. 1c blue and black lines), and similarly to a Rab11-

GTP binding mutant (AS-Rab11$^{RBD\ mutant}$) (Figure 1b). In line with these results, increased FRET emission ratio and Rab11-GTP content were detected after co-expression of AS-Rab11^{wt} with SH3BP5, a Rab11-GEF (Sakaguchi et al., 2015) (Figures 1b, Supplementary Fig. 1e). On the contrary, co-expression of TBC1D9B, a Rab11-GAP (Gallo et al., 2014) decreased FRET emission ratio and Rab11-GTP content in cells (Figures 1b, Supplementary Fig. 1e). A similar emission was obtained by co-expression of RabGDI, a Rab11 dissociation inhibitor (Chen et al., 1998), and was reverted by the use of a GDI-insensitive biosensor mutant (AS-Rab11^{N206X})(Figure 1b). This regulation was found specific, as co-expression of AS-Rab11^{wt} with either Rac1 or Rab5 GEFs and GAPs had no effect on biosensor response (Figure 1b). Next, AS-Rab11 binding to guanine nucleotides was assessed by thin layer chromatography. Equal amounts of GDP and GTP associated with the wild-type biosensor form, whereas either GTP or GDP bound the constitutively active (Q70L) or the dominant negative (S25N) biosensor forms, respectively (Supplementary Fig. 1f). At the same time, AS-Rab11 was able to bind and replace GDP with GTP similarly to Rab11 (Supplementary Fig. 1g). The biosensor was found to interact with recombinant FLAG-RabGDI, FLAG-SH3BP5, and FLAG-TBC1D9B (Supplementary Figs. 2a-c). Whereas AS-Rab11$^{RBD\ mutant}$ interacted with endogenous FIP2 and FIP4, AS-Rab11^{WT} did not, indicating that the probe in its active conformation is not able to compete for endogenous targets (Supplementary Fig. 2d). Finally, As-Rab11 localized with markers of early and recycling endosomes but was absent from cis-Golgi and late endosome structures (Supplementary Figs. 3a-e), thus showing a pattern consistent with the functions of unmodified, endogenous Rab11.

Increased FRET emission ratio was detected both on tubulovesicular structures situated in the proximity of the nucleus and on small membrane-bound organelles positioned at the cell periphery (Figures 1c, d). To exclude the possibility that such high FRET efficiency was caused by random probe accumulation, a correlation plot of the sensitized FRET (i.e. the measure of FRET efficiency corrected for excitation and emission crosstalk) versus the CFP intensities was generated. Sensitized FRET was higher in endosomes than in cytosol (Figure 1e), as indicated by the 2 different slopes of the regression line that correlates the sensitized FRET and the CFP intensities measured in endosomes and cytosol, respectively. Moreover, to assess the spatial distribution of active Rab11 in cells, the FRET/CFP ratio of structures was measured as a function of the distance from the nucleus and FRET emission ratio appeared significantly higher on the ERC than on PE (Figure 1f).

Overall, these results demonstrate that this biosensor can monitor the nucleotide binding status of Rab11 and that active Rab11 is spatially restricted in both peripheral and juxtanuclear endosomal structures.

Activated-Rab11 labels PtdIns(3)P$^+$ endosomes.

To examine the subcellular distribution and the identity of membrane-bound structures displaying active Rab11, AS-Rab11-expressing cells were analyzed by confocal microscopy after the internalization of fluorescent transferrin (Tf-647), an early-recycling endosome marker (Sonnichsen et al., 2000). In line with previous studies (Ren et al., 1998; Ullrich et al., 1996), perinuclear accumulation of active Rab11 (Figure 2a left panel, pseudocolor map) and Tf-647 (Figure 2a left panel, gray scale) was observed. In addition, enlargement of the peri-plasmalemmal region showed overlap between the highest FRET signal (Figure 2a right panel, red line) and Tf-647 (Figure 2a right panel, black line). Accordingly, two-dimensional representation of pixel intensities (Figure 2a right panel, line intensity profile) along a line starting from the nucleus and reaching the plasma membrane (Figure 2a left panel, white line) showed almost perfect overlap between FRET ratio (Figure 2a righ panel, red line) and Tf-647 (Figure 2a right panel, black line) signals in both the perinuclear and peripheral region. In further agreement, analysis of colocalization, as determined by Pearson's coefficient, showed high correlation between FRET ratio and Tf-647 positivity both in the ERC and PE (Figure 2a right panel), indicating that active Rab11 is equally distributed in perinuclear and peripheral Tf-positive compartments.

To gain insight into the localization of active Rab11, early and recycling endosome specific markers were similarly studied by analyzing a red fluorescent tagged versions of either Rab4, Rab5 or the PtdIns(3)*P* probe mCherry-FYVE2X. Identical distribution and strong colocalization were observed by fine mapping of active-Rab11 and mRFP-Rab4-positive structures, in pseudocolor and grayscale, respectively (Figure 2b). Conversely, endosomal membranes labelled by mRFP-Rab5 colocalized with active Rab11 at the cell periphery but not at the perinuclear recycling compartment (Figure 2c). Similarly, active-Rab11 strongly co-localized with the early endosome marker PtdIns(3)*P*, as detected with the mCherry-FYVE2X probe, on peripheral but not on perinuclear membrane-bound structures (Figure 2d). These results indicate that PEs, in which active Rab11 colocalized with PtdIns(3)*P*, correspond to early endosomes.

Exit from endosome relies on Rab11 and PtdIns(3)P

To examine the relationship between Rab11, PtdIns(3)*P* and recycling cargo in peripheral endosomes, the localization of Rab11 and Transferrin receptor (TfR) on PtdIns(3)*P*-positive structures was monitored during the continuous uptake of Tf. Confocal microscopy analysis revealed a frequent growth of tubular $Rab11^+$/mCherry-TfR^+ structures from PEs (Figure 3a). Furthermore, Tf uptake increased Rab11 activity (Supplementary Figs. 4a, b) and expression of a Rab11 dominant negative form inhibited Tf recycling and promoted its accumulation (Supplementary Figs. 4c-e), thus indicating that removal of recycling cargo from endosomes requires Rab11 activation. In agreement, increased FRET/CFP signal on the nascent vesicle began 5 seconds before fission, concomitantly with a PtdIns(3)*P* burst, and reached maximal signal at the time of fission (Figures 3b, c, Supplementary Figs. 4f-h). Such activation kinetics did not rely on biosensor abundance as both temporal assessment and titration of AS-Rab11 level on endosomes showed robust and coherent biosensor response at various probe expression levels (Figure 3c grey line, Supplementary Figs. 4i). Unexpectedly, on the nascent recycling structure, Rab11 activation was initially preceded by the increase of PtdIns(3)*P*-levels but was later followed by a PtdIns(3)*P* decrease, starting at the time of fission (Figures 3b, c, Supplementary Figs. 4f-h). These results show that, on peripheral endosomes, PtdIns(3)*P* peaks concomitantly with Rab11 activation and declines with the fission of recycling cargo-containing vesicles.

To gain insight into this process, COS-7 cells expressing perinuclear localized AS-Rab11 were bleached to avoid contaminating signals from the ERC region and movement of active $Rab11^+$ vesicles was analyzed after Tf addition (Figure 3d). $Rab11^+$ vesicles followed long-range linear movements and then eventually collapsed into ERC membranes (Figure 3d), thus indicating that juxtanuclear AS-Rab11-positive structures derived in part from peripheral endosomes. Accordingly, AS-Rab11-positive endosomal structures accumulated in the perinuclear region during the continuous uptake of Tf and resulted in a steady state after 15 minutes (Supplementary Figs. 5a-e). By interfering with microtubule polymerization using a treatment with Nocodazole, vesicles carrying an active Rab11 failed to appear as a linear series of dots over time (Supplementary Fig. 5f). This indicated that disruption of microtubule-dependent transport abolished long-range movements of AS-Rab11-positive membranes without compromising Tf accumulation (Supplementary Figs. 5f-h). Consistently, displacement of endocytic structures, as

well as Rab11 activation were decreased upon Nocodazole treatment (Figures 3e, f). These data suggested that minus end-directed microtubule motor transport is required for endocytic structure movement. To test this hypothesis, acute inactivation of retrograde transport using Ciliobrevin D, a Dynein inhibitor (Firestone et al., 2012), was performed. Ciliobrevin D treatment decreased long-range retrograde motion of active Rab11$^+$ vesicles and had a minor impact on vesicle linear movement/displacement (Figures 3e, g, h) consistently with multiple Rab11/microtubule-dependent trafficking routes (Delevoye et al., 2014). Finally, both Nocodazole and Ciliobrevin D treatments decreased juxtanuclear accumulation of endocytosed transferrin (Figures 3i, j).

Overall, these data indicate that transferrin receptor is removed from PEs and transported to the ERC through a local increase of PtdIns(3)*P*, the activation of Rab11, the hydrolysis of PtdIns(3)*P*, and eventually the dynein-mediated vesicular transport.

PI3K-C2α controls Rab11 activity on PtdIns(3)P$^+$ endosomes

In early endosomes, PtdIns(3)*P* is mainly produced by Class III PI3K. However, a small but significant amount of PtdIns(3)*P*, ranging up to 20%, derives from Class II PI3Ks (Devereaux et al., 2013) and is putatively required for Rab11 activation (Franco et al., 2014a; Franco et al., 2016). To further determine whether the activation of Rab11 preferentially depended on either Class II or III PI3K, modulation of the AS-Rab11 probe was studied after either PI3K-C2α or Vps34 knock-down or Vps34 inhibition (Supplementary Figs. 6a-c). As expected, knock-down of PI3K-C2α induced a 20% loss of PtdIns(3)*P* as well as a 50% drop in Rab11 activity (Figures 4a, b). On the contrary, knock-down or inhibition of Vps34 by VPS34-IN1 decreased PtdIns(3)*P* cell content by 80% but failed to significantly reduce the levels of active Rab11 (Figures 4a, b). This highlights the distinct role of PI3K-C2α in controlling Rab11 activity in PE. In addition, PI3K-C2α localization during cargo release from PtdIns(3)*P*$^+$ structures was imaged. GFP-PI3K-C2α co-localized with mCherry-FYVE2X during the fission of mECFP-Rab11 positive structures (Figures 4c, Supplementary Figs. 6d-f), while it was undetected in the newly formed mECFP-Rab11$^+$/mCherry-TfR$^+$ membranes (Supplementary Figs. 6e-g). Interestingly, such PI3K-C2α localization strictly depended on its N-terminal Clathrin binding domain (Gaidarov et al., 2001), as loss of this domain (Gulluni et al., 2017a) resulted in a diffuse cytosolic distribution around the PE (Figure 4d).

Number, displacement and direction of Rab11-positive vesicles leaving PEs were analyzed in PI3K-C2α-knock-down cells to further characterize the role of PI3K-C2α in the control of Rab11-mediated intracellular trafficking. Reduction of PI3K-C2α abundance as well as the expression of GFP-Rab11^{S25N} lowered the number of Rab11^{+} vesicles emerging from PEs (Figure 4e). In further support, increased residence time of Rab11 at the PEs was observed in both PI3K-C2α-KD and Rab11^{S25N} expressing cells (Figure 4f). On the contrary, pharmacological inhibition of Vps34 did not alter either the number of fission events or the residence time of Rab11 on PEs (Figures 4e, f), strengthening the idea that Vps34 and PI3K-C2α present non-redundant functions during the endocytic recycling of transferrin.

Next, to further confirm this evidence, quantitation and localization of labelled Tf were performed. PI3K-C2α-KD and GFP-Rab11^{S25N}-expressing cells displayed increased Tf accumulation and decreased Tf perinuclear storage, which was not affected by either inhibition or RNAi-mediated suppression of Vps34 (Figures 4g, h, Supplementary Figs. 6c, h). Such transferrin recycling delay did not depend on the efficiency of molecular motors, as similar distribution of linearity and vesicle speed between GFP-Rab11^{S25N} expressing cells, PI3K-C2α-KD and controls were measured by tracking of individual Rab11^{+} vesicles (Supplementary Figs. 6i, j). This Tf delivery defect in PI3K-C2α-KD cells was rescued by expression of a wild-type (PI3K-C2α^{WT}) or a PI3P-only producing PI3K-C2α form (PI3K-C2α^{CIII}) (Figure 4i). On the contrary, expression of a kinase inactive mutant (PI3K-C2α^{R1251P}) did not restore juxtanuclear Tf localization (Figure 4i), thus demonstrating that Tf delivery to perinuclear endosomes is controlled by the PI3K-C2α-dependent PI3P production. In line with these results, silencing of PI3K-C2α led to the intracellular entrapment of Tf (Supplementary Fig. 6k).

Altogether, these results indicated that removal of recycling cargo from early endosomes requires PI3K-C2α-mediated PI3P production, necessary for Rab11 activation. Nonetheless, PtdIns(3)*P* decreased prior fission and disappeared from the detached Rab11^{+} vesicle, suggesting that removal of recycling cargo from endosomes depends on PtdIns(3)*P* hydrolysis.

The PtdIns(3)P phosphatase MTM1 is a Rab11 effector

In order to identify the PtdIns(3)*P* phosphatase that connects the increase in Rab11 activity with the concomitant decrease of PtdIns(3)*P*, pull-down of potential PtdIns(3)*P* phosphatases

working as Rab11 effectors was performed. Five different PtdIns(3)*P* phosphatases, members of the Myotubularin protein family, were tested using immobilized Glutathione S-transferase (GST)-Rab11 as a probe. Among them, MTM1 was found to preferentially bind Rab11:GTP-γS rather than Rab11:GDP (Figure 5a). On the contrary, no interactions were detected for MTMR2, MTMR4, MTMR6, MTMR9 (Figure 5a). Remarkably, MTM1 was isolated from total cell extracts by pull-down of Rab11-GTP using a recombinant Rab11-GTP interacting protein (GST-RBD11) as a probe (Franco et al., 2014a) (Figure 5b), and by immunoprecipitation of endogenous Rab11 (Supplementary Fig. 7a), thus indicating that Rab11 is associated with MTM1 *in vivo*. In further agreement, an *in vitro* binding assay using purified GST-Rab11 and His-Flag-MTM1 showed preferential binding of recombinant MTM1 with Rab11:GTP-γS compared to Rab11:GDP or other Rabs (Figures 5c, Supplementary Fig. 7b). RNA-interference mediated downregulation of MTM1 (MTM1-KD) (Supplementary Fig. 7c) significantly increased PtdIns(3)*P* levels as well as Rab11 activity (Figures 5d, e). In MTM1-KD cells, additional silencing of PI3K-C2α but not of Vps34 reduced Rab11 activation (Figure 5e). These results indicated that active Rab11 is associated with the PtdIns(3)*P* phosphatase MTM1 which actively dephosphorylates the PtdIns(3)*P* present on the structures directed towards the ERC. In agreement with this view, confocal microscopy analysis showed that Rab11 and MTM1 colocalized both in PE and ERC membranes as well as in TfR^{+} vesicles (Figures 5f, g, Supplementary Fig. 7d). In line with these results, Rab11 silencing blocked perinuclear and peripheral MTM1 localization (Supplementary Fig. 7e).

To further characterize the impact of MTM1 in the control of Rab11-mediated intracellular trafficking, $Rab11^{+}$ vesicles detaching from PEs were analyzed after RNAi-mediated downregulation of MTM1 (MTM1-KD). Loss of MTM1 as well as expression of GFP-$Rab11^{S25N}$ decreased the number of Rab11 positive fission events from PEs (Figure 5h), without affecting vesicle speed (Supplementary Fig. 7f). Furthermore, the residence time of Rab11 positive structures on PEs increased in both conditions (Figure 5i). Therefore, either impaired activation of Rab11 or lack of the phosphatase activity delayed fission. In agreement, MTM1-KD and GFP-$Rab11^{S25N}$-expressing cells displayed increased Tf content and decreased perinuclear accumulation of the recycling cargo (Figures 5j, k, Supplementary Fig. 7g). To identify the lipid kinase that antagonizes MTM1 activity, the rescue of Tf uptake and Tf accumulation of the recycling cargo at the ERC were performed. Acute perturbation of PtdIns(3)*P* synthesis by Vps34 inhibition partially restored Tf accumulation and perinuclear storage in MTM1-KD cells (Figures

5j, k) without affecting the increase in Rab11 activation due to MTM1 loss (Figure 5e). In agreement, Rab11-mediated fission events appeared more frequent in MTM1-KD/VPS34-IN1 than in MTM1-KD cells (Figure 5h), thus indicating that fission requires a significant reduction of PtdIns(3)*P*. In the absence of MTM1, knock-down of either PI3K-C2α alone or in combination with Vps34 inhibition led to decreased Rab11 activity. Conversely, in the absence of MTM1, Vps34 inhibition alone was not able to restore increased Rab11 activity (Figure 5e). Therefore, PI3K-C2α is the main kinase driving PtdIns(3)*P* production required for Rab11 activation, consequent fission and Tf recycling (Figure 5h, j, k).

Taken together, these results show that removal of recycling cargo from peripheral endosomes depends on subsequent PI3K-C2α-mediated PtdIns(3)*P* production, Rab11 activation and MTM1-dependent PtdIns(3)*P* destruction, leading to fission of vesicles and their eventual dynein-mediated transport to the ERC.

Discussion

Removal of recycling cargo from peripheral PtdIns(3)P^+ endosome requires PtdIns(3)*P* hydrolysis and the activation of the small GTPase Rab11. However, whether these events are linked is unknown. Therefore, a genetically-encoded FRET biosensor for Rab11 was generated to detect spatial and temporal variations of Rab11 activity in endosomes. This biosensor named AS-Rab11 was proven to be effective into limited diffusional space, such as in membrane and vesicular compartments and its activity was found to depend on both positive and negative Rab11 regulators, such as Rab11 GEF, GAP and GDI (Chen et al., 1998; Gallo et al., 2014; Sakaguchi et al., 2015). Using AS-Rab11, we revealed that: (I) Rab11 activation is initiated on PtdIns(3)*P*-positive membranes where sorting of recycling cargo occurs; (II) Rab11 activation level determines the release rate of membranes destined to the ERC; and (III) such release required MTM1, a PtdIns(3)*P* phosphatase, which was found to interact with active Rab11. These results establish that removal of recycling cargo from peripheral PtdIns(3)P^+ endosome requires coupling of Rab11 activity and PtdIns(3)*P* turnover (Figure 6).

Extensive time lapse analyses and biochemical experiments revealed enrichment of active-Rab11 on juxtanuclear positioned ERC and peripheral PtdIns(3)P^+ endocytic structures. In addition, they evidenced a critical role of activated Rab11 in the release of Transferrin receptors (TfR) from PtdIns(3)P^+ membranes. Given that PtdIns(3)*P* is a bona-fide marker (Simonsen et al., 1998) of EE, a compartment where recycling cargoes are sorted and directed toward the ERC or plasma membrane (Campa and Hirsch, 2017; Ullrich et al., 1996), our data suggest that Rab11 activation is initiated on EE membranes where sorting of recycling cargoes occurs. In agreement, the direct visualization of active Rab11 patches localizing with TfR on PtdIns(3)P^+ membranes corroborate these evidences. Our experiments show that membranes decorated by active Rab11 are not maintained indefinitely on PtdIns(3)P^+ structures but are delivered from peripheral to juxtanuclear recycling compartment. These observations define that, differently from active Rab5 that mediates the expansion of Rab5 domain on early endosomes, active Rab11 critically affects cargo flow by recruiting the protein machinery involved in vesicle transport. In line with this view, our results evidenced that active Rab11 vesicles detaching from peripheral endosomes accumulate on ERC membranes in a dynein-dependent manner.

Our observations extend the previous identification of PI3K-C2α as a key controller of Rab11 activation on endosomes (Franco et al., 2014a) and define that localization of PI3K-C2α on

endosomes strictly depends on its clathrin binding domain (Campa et al., 2015; Gaidarov et al., 2001). Notably, depletion of PI3K-C2α delays the kinetic of vesicle release from PtdIns(3)P^+ structure where TfR sorting takes place (Maxfield and McGraw, 2004), thus linking the role of PI3K-C2α to endosomal sorting. Accordingly, depletion of PI3K-C2α, as well as loss of its catalytic activity, decreases both activity and fission of Rab11-positive vesicles from PtdIns(3)P^+ structures, thereby mimicking the phenotype observed in cells expressing dominant negative Rab11.

In light of the highly dynamic Rab11 activation on PtdIns(3)P^+ structures, and the distinct phosphoinositide composition of EE and the perinuclear recycling compartment (Marat and Haucke, 2016), a phosphoinositide conversion can be expected between these two Rab11 positive membrane domains. Our data demonstrated that this transition is controlled by MTM1, which was found to interact with active Rab11. MTM1 was shown to antagonize the Class II and Class III derived PtdIns(3)*P* pools in *D. melanogaster* and *C. elegans* and was demonstrated to be essential in the exit of cargos from PtdIns(3)*P* endosomes (Ketel et al., 2016; Velichkova et al., 2010a). Accordingly, $MTM1^+$/$Rab11^+$ vesicles were observed during removal of recycling cargo from PtdIns(3)*P* compartment, thus indicating that active Rab11 provides a signal to control MTM1 localization. Given that recycling vesicles require dynein to reach the ERC, removal of PI3P can be explained by the fact that the presence of this lipid, a well-known activator of centrifugal kinesin-mediated transport(Hoepfner et al., 2005), might disturb this centripetal trafficking.

The development and application of AS-Rab11 to quantitatively analyze Rab11 activity in living cells allowed to dissect and analyze the initial step of the PtdIns conversion mechanism (Marat and Haucke, 2016) required for the exit of recycling cargo from endosomes. Our data indicate that PI3K-C2α provides a spatially localized and temporally controlled PtdIns(3)*P* pool sufficient to activate Rab11 on early endosomes, allowing establishment and maintenance of receptor recycling towards the ERC. Activation of Rab11 eventually contributes to the recruitment of MTM1 and the ensuing reduction of PtdIns(3)*P* level on membranes destined to the perinuclear endosome.

Figures

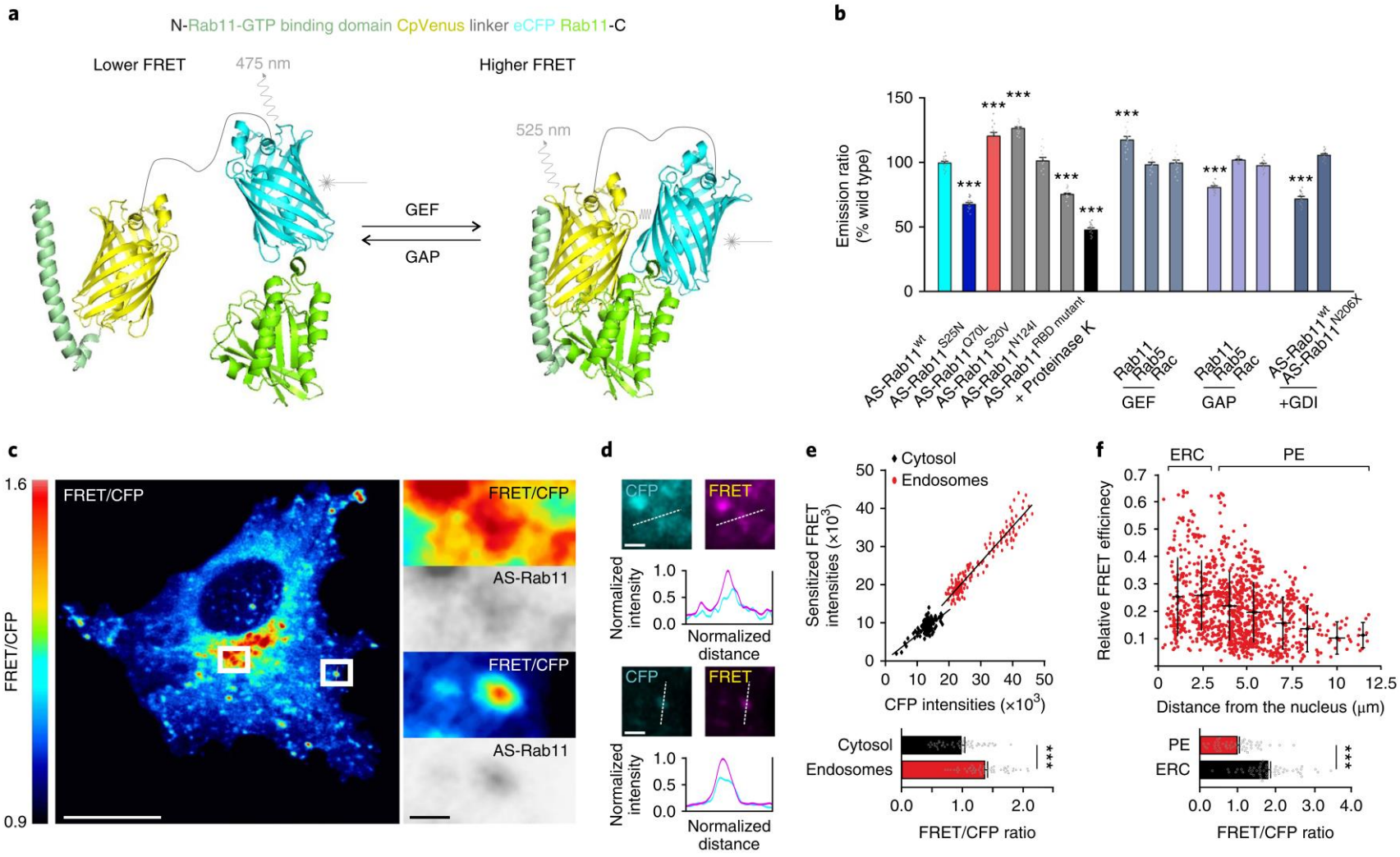
a
N-Rab11-GTP binding domain CpVenus linker eCFP Rab11-C
Lower FRET
475 nm
Higher FRET
525 nm
GEF
GAP
b
Emission ratio (% wild type)
150
100
50
0
AS-Rab11wt
AS-Rab11S25N
AS-Rab11Q70L
AS-Rab11S20V
AS-Rab11N124I
AS-Rab11RBD mutant
+ Proteinase K
Rab11
Rab5
Rac
GEF
GAP
AS-Rab11wt
AS-Rab11N206X
+GDI
c
1.6
0.9
FRET/CFP
AS-Rab11
d
CFP
FRET
Normalized intensity
Normalized distance
e
Cytosol
Endosomes
Sensitized FRET intensities (×10³)
CFP intensities (×10³)
FRET/CFP ratio
f
ERC
PE
Relative FRET efficinecy
Distance from the nucleus (μm)
FRET/CFP ratio

Fig. 1: The FRET biosensor AS-Rab11 specifically measures Rab11 nucleotide binding status.

a. Tridimensional representation of the genetically encoded fluorescence energy transfer (FRET) probe AS-Rab11 (activation sensor Rab11) in its inactive (bound to GDP, left) or active conformation (bound to GTP, right). Yellow and light blue β -barrels represent yellow- and cyan-emitting mutants of fluorescent proteins, respectively. Sea-green α -helix, black line, and green β -barrels structures indicate the Rab11-GTP-binding domain (C-terminal region of FIP3), the proteinase K sensitive linker domain and the Rab11a protein, respectively. In this probe design, an increase of Rab11 GTP loading promotes the binding of the C-terminal region of FIP3 to Rab11a, modifying the relative orientation of the two fluorophores and thereby increasing FRET signal.

b. Quantifications of FRET efficiency of AS-Rab11wt, AS-Rab11 mutant forms, and proteinase-K-treated AS-Rab11wt, as well as AS-Rab11wt co-expressed with the indicated GEFs and their target GTPases (SH3BP5, RABEX-5, and TIAM1, respectively), AS-Rab11wt co-expressed with the indicated GAPs and their target GTPases (TBC1D9B, RN-3, and ARHGAP15, respectively), and AS-Rab11wt or AS-Rab11N206X co-expressed with RabGDI (n = 12 independent experiments; data represent mean ± s.e.m.; ***P < 0.005; one-way ANOVA).

c. Representative FRET/CFP ratio images of the AS-Rab11 biosensor in COS-7 cells (pseudocolor images represent FRET/CFP ratio intensity values). The upper and lower limits of the FRET/CFP ratio are shown on the left side bar. Magnification of FRET/CFP ratio images and AS-Rab11 localization in juxtanuclear (upper) and peripheral endocytic structures (lower). Right panel, pseudocolor images represent FRET/CFP ratio intensity values; grayscale image indicates emission of mcpVenus (AS-Rab11) after its direct excitation). Scale bars, 10 μ m.

d. Representative line intensity profile of FRET sensitized (magenta) and CFP (cyan) signal detected in juxtanuclear (top) and peripheral (bottom) endocytic structures. The magenta and cyan images represent FRET sensitized and CFP signals, respectively. Scale bars, 1 μ m.

e. Top, scatter plot of sensitized FRET intensities as a function of CFP intensities in ASRab11-expressing cells (black and red dots represent the sensitized FRET and CFP intensity of cytosolic and membrane-bound structures, respectively; regression line is in black; n = 4 independent experiments). Bottom, quantification of the FRET/CFP ratio between cytosolic and

endocytic structures labeled by AS-Rab11 (n = 50 independent experiments; data represent mean ± s.e.m.; ***P < 0.005; two-tailed unpaired t-test).

f. Top, scatter plot of relative FRET efficiency as a function of distance from the nucleus for endocytic structures labeled by AS-Rab11 (n = 4 independent experiments; black line represents mean ± s.e.m.). Bottom, quantification of the FRET/CFP ratio between juxtanuclear (ERC, 0 to 3 μ m from nucleus) and peripheral (PE, 3 to 12 μ m from the nucleus) endocytic structures labeled by AS-Rab11 (n = 50 independent experiments; data represent mean ± s.e.m.; ***P < 0.005; t-test).

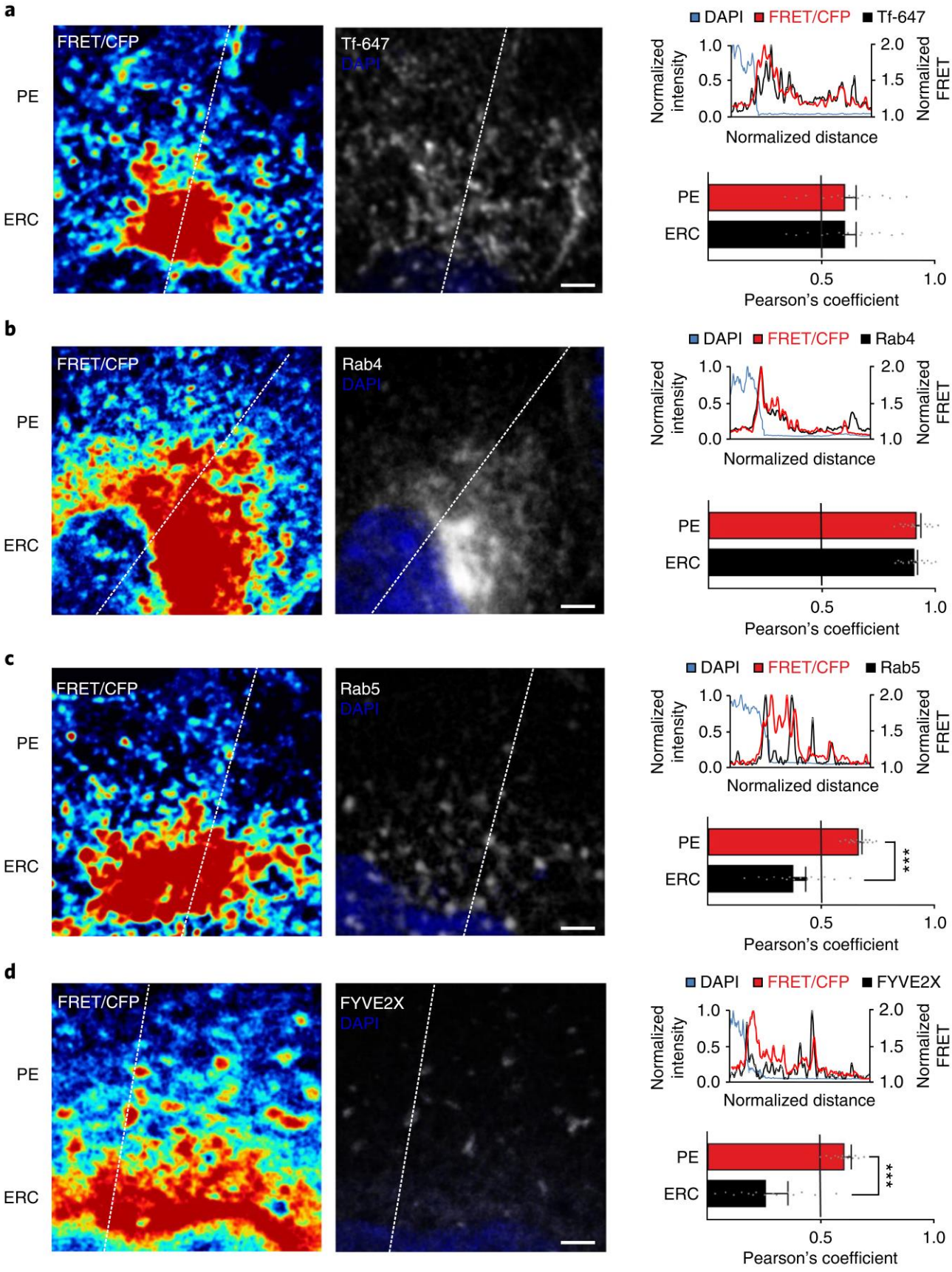
a
FRET/CFP
PE
ERC
Tf-647
DAPI
DAPI FRET/CFP Tf-647
Normalized intensity
Normalized FRET
Normalized distance
PE
ERC
Pearson's coefficient
b
FRET/CFP
PE
ERC
Rab4
DAPI
DAPI FRET/CFP Rab4
Normalized distance
Pearson's coefficient
c
FRET/CFP
PE
ERC
Rab5
DAPI
DAPI FRET/CFP Rab5
Normalized distance
***
Pearson's coefficient
d
FRET/CFP
PE
ERC
FYVE2X
DAPI
DAPI FRET/CFP FYVE2X
Normalized distance
***
Pearson's coefficient

Fig. 2: Juxtanuclear and peripheral localization of active Rab11 on distinct endosome populations.

a. Representative localization of active Rab11 on transferrin-positive endosomes. FRET/CFP ratio images (pseudocolor mode) of the AS-Rab11 biosensor on endosomes labeled by fluorescent transferrin (gray scale). White line defines the region over which the FRET/CFP ratio and fluorescence transferrin signal were measured. Scale bar, 1 μ m. Top right, line intensity profile of the FRET/CFP ratio (red), labeled transferrin (black) and nuclei (blue). Bottom right, quantification in juxtanuclear (ERC) and peripheral (PE) endosomes of colocalization percentage (Pearson's correlation coefficient) between FRET/CFP signal and transferrin-labeled endocytic structures (n = 15 independent experiments; data represent mean ± s.e.m.; two-tailed, unpaired t-test).

b. Representative localization of active Rab11 on Rab4-positive endosomes. FRET/CFP ratio images (pseudocolor mode) of AS-Rab11 biosensor on endosomes labeled by mRFP-Rab4 (gray scale). The white line defines the region over which the FRET/CFP ratio and mRFP-Rab4 signal were measured. Scale bar, 1 μ m. Top right, Line intensity profile of the FRET/CFP ratio (red), mRFP-Rab4 (black) and nuclei (blue). Bottom right, quantification in juxtanuclear (ERC) and peripheral (PE) endosomes of colocalization percentage (Pearson's correlation coefficient) between FRET/CFP signal and Rab4-labeled endocytic structures (n = 15 independent experiments; data represent mean ± s.e.m.; t-test).

c. Representative localization of active Rab11 on Rab5-positive endosomes. FRET/CFP ratio images (pseudocolor mode) of AS-Rab11 biosensor on endosomes labeled by mCherry-Rab5 (gray scale). White line defines the region over which the FRET/CFP ratio and mCherry-Rab5 signal were measured. Scale bar, 1 μ m. Top right, line intensity profile of FRET/CFP ratio (red), mCherry-Rab5 (black) and nuclei (blue). Bottom right, quantification in juxtanuclear (ERC) and peripheral (PE) endosomes of colocalization percentage (Pearson's correlation coefficient) between FRET/CFP signal and Rab5-labeled endocytic structure (n = 15 independent experiments; data represent mean ± s.e.m.; ***$P < 0.005$; t-test).

d. Representative localization of active Rab11 on PtdIns(3)P-positive endosomes. FRET/CFP ratio images (pseudocolor mode) of AS-Rab11 biosensor on endosomes labeled by mCherry-

FYVE2X (gray scale). White line defines the region over which FRET/CFP ratio and Cherry-FYVE2X signal were measured. Scale bar, 1 μ m. Line intensity profile of FRET/CFP ratio (red), mCherry-FYVE2X (black) and nuclei (blue). Quantification in juxtanuclear (ERC) and peripheral (PE) endosomes of colocalization percentage (Pearson's correlation coefficient) between FRET/CFP signal and PtdIns(3)P-labeled endocytic structures (n = 15 independent experiments; data represent mean ± s.e.m.; ***P < 0.005; t-test).

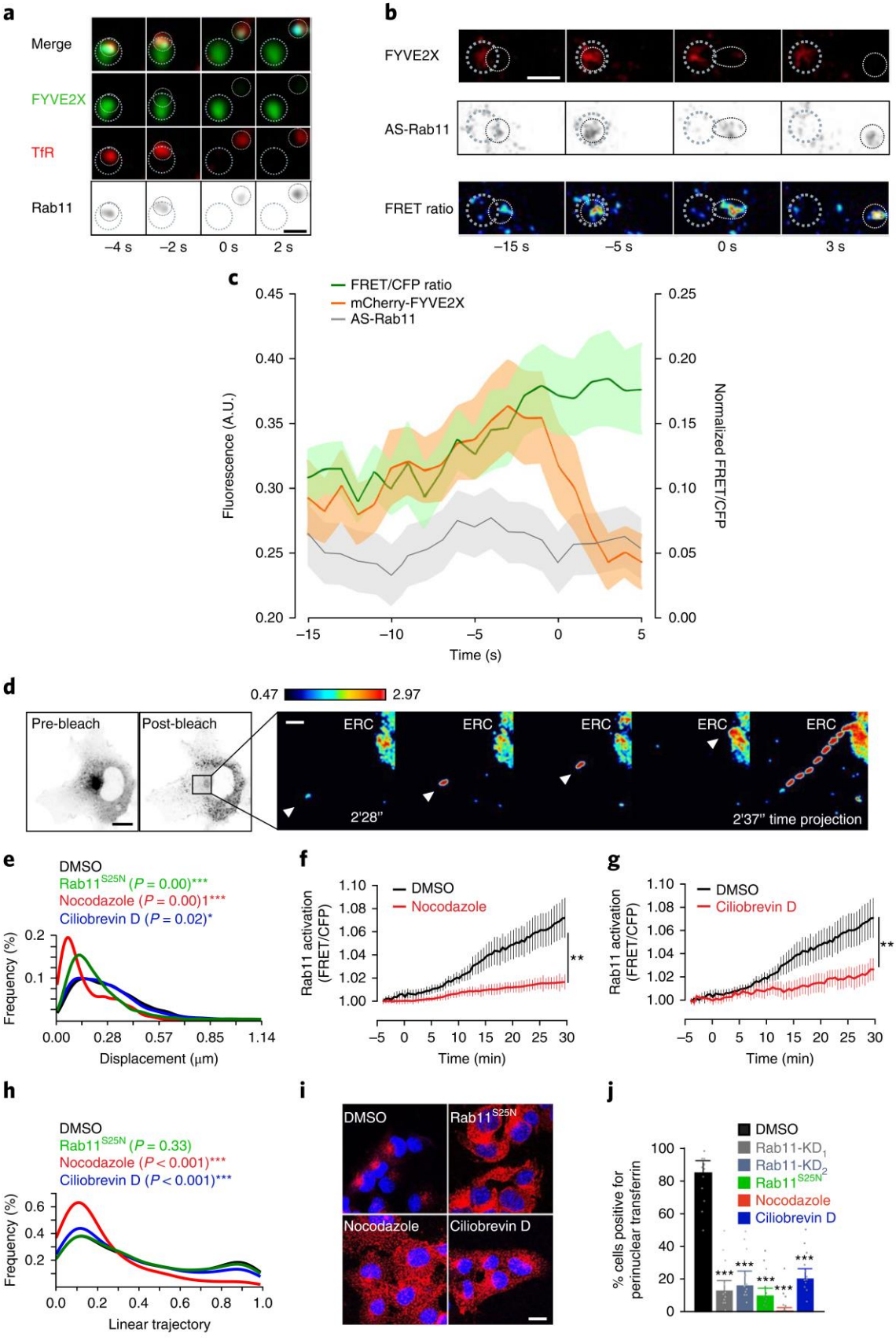
a
Merge
FYVE2X
TfR
Rab11
−4 s
−2 s
0 s
2 s
b
FYVE2X
AS-Rab11
FRET ratio
−15 s
−5 s
0 s
3 s
c
FRET/CFP ratio
mCherry-FYVE2X
AS-Rab11
Fluorescence (A.U.)
Normalized FRET/CFP
Time (s)
d
0.47
2.97
Pre-bleach
Post-bleach
ERC
2'28"
2'37" time projection
e
DMSO
Rab11S25N (P = 0.00)***
Nocodazole (P = 0.00)1***
Ciliobrevin D (P = 0.02)*
Frequency (%)
Displacement (μm)
f
DMSO
Nocodazole
Rab11 activation (FRET/CFP)
Time (min)
g
DMSO
Ciliobrevin D
Rab11 activation (FRET/CFP)
Time (min)
h
DMSO
Rab11S25N (P = 0.33)
Nocodazole (P < 0.001)***
Ciliobrevin D (P < 0.001)***
Frequency (%)
Linear trajectory
i
DMSO
Rab11S25N
Nocodazole
Ciliobrevin D
j
DMSO
Rab11-KD1
Rab11-KD2
Rab11S25N
Nocodazole
Ciliobrevin D
% cells positive for perinuclear transferrin

Fig. 3: Rab11 activation kinetics on PtdIns(3)P-positive endosomes

a. Representative time-lapse series of cells co-expressing the mCherry-transferrin receptor (TfR), mECFP-Rab11 and GFP- FYVE2X. White circles represent membrane-bound structures. Scale bar, 1 μ m.

b. Representative time-lapse series of cells co-expressing AS-Rab11 and mCherry-FYVE2X. White circles represent membrane-bound structures. The pseudocolor mode represents the FRET/ CFP ratio; gray scale indicates the emission of mcpVenus after its direct excitation. Scale bar, 1 μ m.

c. Quantification of the FRET/CFP ratio (green line), mCherry-FYVE2X fluorescence emission (orange line) and AS-Rab11 mcpVenus emission (gray line) as a function of time in 28 individual vesicle tracks directed toward the ERC. The time point of detachment from early endosomes was recorded and used to shift the time courses so that all 28 detachment events were synchronized at the chosen time point of 0 s. The normalized FYVE2X is shown on the primary y axis. The normalized value of FRET/CFP ratio is shown on the secondary y axis (n = 4 independent experiments).

d. Representative time-lapse series of long-range transport of an active Rab11 vesicle toward the ERC. Gray scale represents mcpVenus fluorescence emission intensities before and after bleaching (left; scale bar, 5 μ m). Magnification shows the juxtanuclear region and time projection (right; scale bar, 1 μ m). Pseudocolor mode represents the FRET/CFP ratio (n = 10 independent experiments).

e. Frequency distribution of Rab11+ vesicle displacement from the origin in cells expressing GFP-Rab11S25N or GFP-Rab11 treated with either vehicle (DMSO), nocodazole (a microtubule depolymerizing drug) or the dynein inhibitor, ciliobrevin D (n = 4 independent experiments; ***P < 0.005; *P < 0.05; two-way ANOVA).

f. Quantification of Rab11 activation in the perinuclear area. Cells were treated with either vehicle (DMSO) or nocodazole (n = 14 independent experiments; data represent mean ± s.e.m.; **P < 0.01; two-tailed unpaired t-test).

g. Quantification of Rab11 activation in the perinuclear area. Cells were treated with either vehicle (DMSO) or ciliobrevin D (n = 14 independent experiments; data represent mean ± s.e.m.; **P < 0.01; t-test).

h. Frequency distribution of linearity of movement of Rab11+ vesicles in cells expressing GFP-Rab11S25N or GFP-Rab11 treated with either vehicle (DMSO), nocodazole or ciliobrevin D (n = 4 independent experiments; data represent mean ± s.e.m.; ***P < 0.005; two-way ANOVA).

i. Representative image of endocytosed transferrin localization in cells expressing GFP-Rab11S25N or GFP-Rab11 treated with either vehicle (DMSO), nocodazole, or ciliobrevin D (n = 4 independent experiments). Scale bar, 10 μ m.

j. Quantification of perinuclear localization of fluorescent transferrin in cells expressing GFP-Rab11S25N or treated with either DMSO/scramble siRNA, Rab11 siRNA 1 (RAB11-KD1), Rab11 siRNA 2 (RAB11-KD2), nocodazole or the dynein inhibitor, ciliobrevin D (n = 12 independent experiments; data represent mean ± s.e.m.; ***P < 0.005; one-way ANOVA).

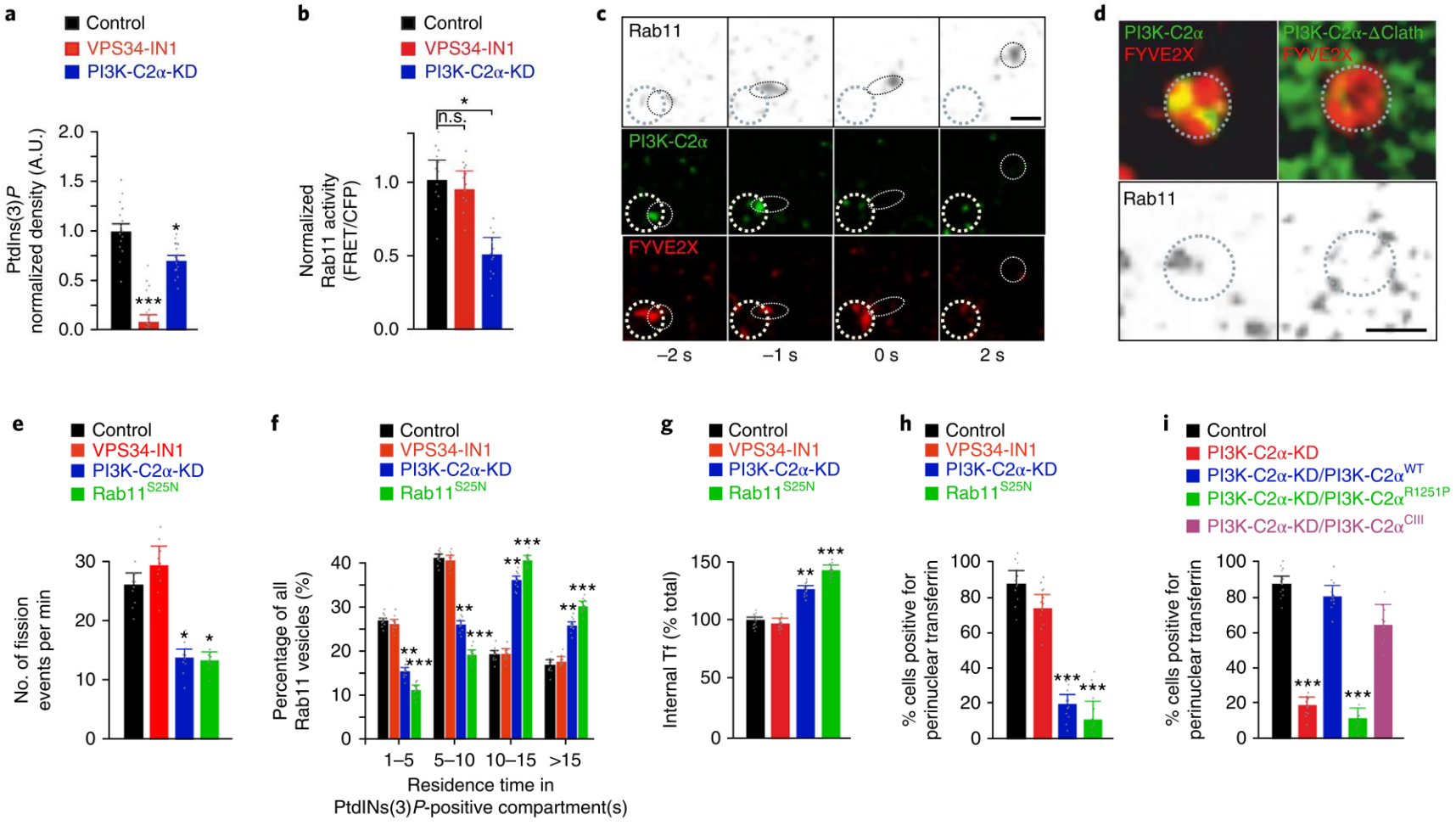
a
Control
VPS34-IN1
PI3K-C2α-KD
PtdIns(3)P normalized density (A.U.)
2.0
1.5
1.0
0.5
0.0
***
*
b
Control
VPS34-IN1
PI3K-C2α-KD
n.s.
*
Normalized Rab11 activity (FRET/CFP)
1.0
0.5
0.0
c
Rab11
PI3K-C2α
FYVE2X
–2 s
–1 s
0 s
2 s
d
PI3K-C2α
FYVE2X
PI3K-C2α-ΔClath
FYVE2X
Rab11
e
Control
VPS34-IN1
PI3K-C2α-KD
Rab11S25N
No. of fission events per min
30
20
10
0
*
*
f
Control
VPS34-IN1
PI3K-C2α-KD
Rab11S25N
Percentage of all Rab11 vesicles (%)
40
30
20
10
0
1–5
5–10
10–15
>15
Residence time in PtdINs(3)P-positive compartment(s)
g
Control
VPS34-IN1
PI3K-C2α-KD
Rab11S25N
Internal Tf (% total)
150
100
50
0
**
***
h
Control
VPS34-IN1
PI3K-C2α-KD
Rab11S25N
% cells positive for perinuclear transferrin
100
80
60
40
20
0
***
***
i
Control
PI3K-C2α-KD
PI3K-C2α-KD/PI3K-C2αWT
PI3K-C2α-KD/PI3K-C2αR1251P
PI3K-C2α-KD/PI3K-C2αCIII
% cells positive for perinuclear transferrin
100
80
60
40
20
0
***
***

Fig. 4: PI3K-C2α-dependent Rab11 activation on PtdIns(3)P-positive endosomes.

a. Quantification of PtdIns(3)P abundance in COS-7 cells treated with either DMSO/Scramble siRNA (control), VPS34 inhibitor (VPS34-IN1), or PI3K-C2α siRNA (PI3KC2α -KD) (n = 15 independent experiments; data represent mean ± s.e.m.; ***P < 0.005, *P < 0.05; one-way ANOVA).

b. Quantification of Rab11 activity in COS-7 cells treated with either DMSO/Scramble siRNA (control), VPS34 inhibitor (VPS34-IN1), or PI3K-C2α siRNA (PI3KC2α -KD). (n = 12 independent experiments; data represent mean ± s.e.m.; *P < 0.05; one-way ANOVA).

c. Representative time-lapse series of cells co-expressing mCherry-FYVE2X, GFP-PI3K-C2α, and mECFP-Rab11 (gray scale). White circles represent membrane-bound structures (n = 6 independent experiments). Scale bar, 1 μ m.

d. Representative image of cells co-expressing mCherry-FYVE2X, mECFP-Rab11 (gray scale) and GFP-PI3K-C2α (PI3K-C2α) or its mutant version GFP-PI3K-C2α -Δ clathrin (PI3K-C2α -Δ Clath). White circles represent membrane-bound structures (n = 6 independent experiments). Scale bar, 1 μ m.

e. Quantification of the number of Rab11-associated fission events generated from mCherry-FYVE2X-positive membranes. COS-7 cells expressing GFP-Rab11S25N or GFP-Rab11 treated with either DMSO/ Scramble siRNA (control), VPS34 inhibitor (VPS34-IN1), or PI3K-C2α siRNA (PI3KC2α -KD, blue bar). (n = 10 independent experiments; data represent mean ± s.e.m.; *P < 0.05; one-way ANOVA).

f. Residence time of GFP-Rab11S25N or GFP-Rab11 structures on mCherry-FYVE2X-positive membranes (black, blue, and red bars). GFP-Rab11-expressing cells were treated with either DMSO/Scramble siRNA (control), VPS34 inhibitor (VPS34-IN1), or PI3K-C2α siRNA (PI3KC2α -KD). (n = 10 independent experiments; data represent mean ± s.e.m.; ***P < 0.005, **P < 0.01; two-way ANOVA.)

g. Quantification of internal transferrin percentage in cells expressing GFP-Rab11S25N or GFP-Rab11 treated with either DMSO/Scramble siRNA (control), VPS34 inhibitor (VPS34-IN1),

or PI3K-C2α siRNA (PI3KC2α -KD). (n = 12 independent experiments; data represent mean ± s.e.m.; **P < 0.01, ***P < 0.005; one-way ANOVA).

h. Quantification of perinuclear localization of fluorescent transferrin in cells expressing GFP-Rab11S25N or GFP-Rab11 treated with either DMSO/ Scramble siRNA (control), VPS34 inhibitor (VPS34-IN1), or PI3K-C2α siRNA (PI3KC2α -KD) (n = 12 independent experiments; data represent mean ± s.e.m.; ***P < 0.005; one-way ANOVA).

i. Quantification of perinuclear localization of fluorescent transferrin in cells expressing GFP-Rab11 treated with either DMSO/Scramble siRNA (control), PI3K-C2α siRNA (PI3KC2α -KD), PI3K-C2α siRNA and PI3K-C2α wt siRNA-resistant (PI3KC2α -KD/ PI3KC2α wt), PI3K-C2α siRNA and PI3K-C2α R1251P siRNA resistant (PI3KC2α -KD/ PI3KC2α 1251), or PI3K-C2α siRNA and PI3K-C2α CIII siRNA resistant (PI3KC2α -KD/ PI3KC2α CIII) (*n* = 12 independent experiments; data represent mean ± s.e.m.; ****P* < 0.005; one-way ANOVA).

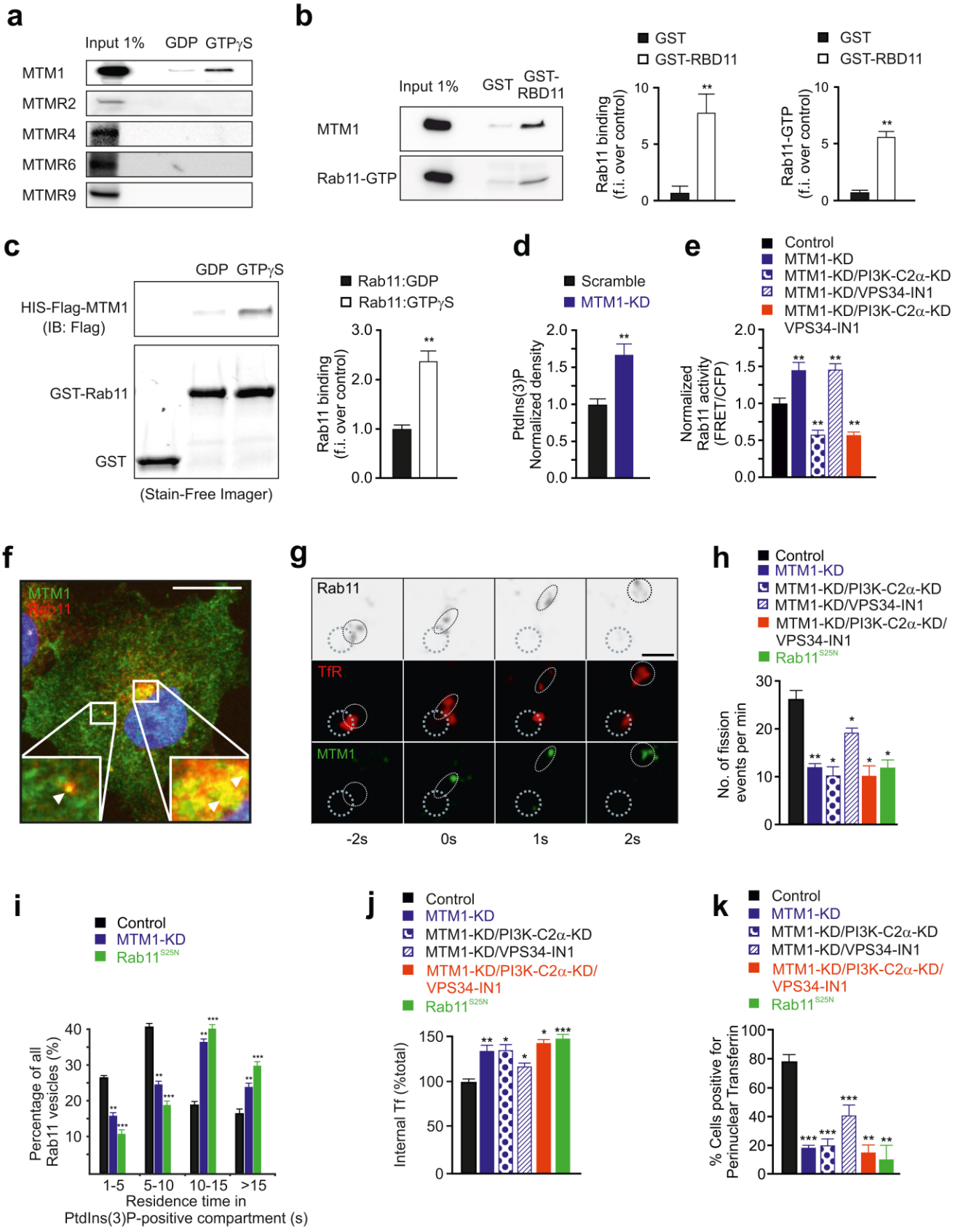
a
Input 1%
GDP
GTPγS
MTM1
MTMR2
MTMR4
MTMR6
MTMR9
b
Input 1%
GST
GST-RBD11
MTM1
Rab11-GTP
GST
GST-RBD11
Rab11 binding (f.i. over control)
Rab11-GTP (f.i. over control)
c
GDP
GTPγS
HIS-Flag-MTM1 (IB: Flag)
GST-Rab11
GST
(Stain-Free Imager)
Rab11:GDP
Rab11:GTPγS
Rab11 binding (f.i. over control)
d
Scramble
MTM1-KD
PtdIns(3)P Normalized density
e
Control
MTM1-KD
MTM1-KD/PI3K-C2α-KD
MTM1-KD/VPS34-IN1
MTM1-KD/PI3K-C2α-KD VPS34-IN1
Normalized Rab11 activity (FRET/CFP)
f
MTM1
Rab11
g
Rab11
TfR
MTM1
-2s
0s
1s
2s
h
Control
MTM1-KD
MTM1-KD/PI3K-C2α-KD
MTM1-KD/VPS34-IN1
MTM1-KD/PI3K-C2α-KD/ VPS34-IN1
Rab11S25N
No. of fission events per min
i
Control
MTM1-KD
Rab11S25N
Percentage of all Rab11 vesicles (%)
1-5
5-10
10-15
>15
Residence time in PtdIns(3)P-positive compartment (s)
j
Control
MTM1-KD
MTM1-KD/PI3K-C2α-KD
MTM1-KD/VPS34-IN1
MTM1-KD/PI3K-C2α-KD/ VPS34-IN1
Rab11S25N
Internal Tf (%total)
k
Control
MTM1-KD
MTM1-KD/PI3K-C2α-KD
MTM1-KD/VPS34-IN1
MTM1-KD/PI3K-C2α-KD/ VPS34-IN1
Rab11S25N
% Cells positive for Perinuclear Transferrin

Fig. 5: The PtdIns(3)P phosphatase MTM1 is a Rab11 effector.

a. Affinity chromatography of Rab11-GTP effectors. Representative western blot of both Rab11-GDP and Rab11-GTPγ S column eluate probed with anti-MTM1, anti-MTMR2, anti-MTMR4, anti-MTMR6, and anti-MTMR9 antibodies (n = 5 independent experiments)

b. Pull down of the endogenous Rab11-GTP and MTM1 complex. Representative western blot of Rab11-GTP pull-down assay probed with anti-MTM1 antibody (n = 5 independent experiments). Quantification of endogenous MTM1 (center) and Rab11-GTP (right) pulled down by GST or GST-RBD11 probe (n = 5 independent experiments; data represent mean ± s.e.m.; **P < 0.01; two-tailed unpaired t-test)

c. In vitro assessment of the association between recombinant Rab11-GTP and MTM1. Left, representative western blot of recombinant Rab11 loaded with GDP or GTPγ S and probed for MTM1 interaction. Right, quantification of recombinant MTM1 pulled down by recombinant Rab11 loaded with GDP or GTPγ S (n = 4 independent experiments, data represent mean ± s.e.m.; **P < 0.01; t-test)

d. Quantification of PtdIns(3)P abundance in COS-7 cells treated with either Scramble siRNA (control) or MTM1 siRNA (MTM1-KD). (n = 12 independent experiments; data represent mean ± s.e.m.; **P < 0.01, t-test.)

e. Quantification of active Rab11 levels in COS-7 cells treated with either Scramble siRNA (control), MTM1 siRNA (MTM1-KD), MTM1 siRNA and PI3KC2α siRNA (MTM1-KD/PI3K-C2α -KD), MTM1 siRNA and VPS34 inhibitor (MTM1-KD/VPS34-IN1), or MTM1 siRNA in combination with PI3K-C2α siRNA and VPS34 inhibitor (MTM1-KD/PI3K-C2α -KD/VPS34-IN1). (n = 12 independent experiments; data represent mean ± s.e.m.; **P < 0.01; one-way ANOVA.)

f. Representative immunofluorescence of COS-7 cells, showing peripheral and perinuclear colocalization of MTM1 with Rab11. Peripheral (left) and perinuclear (right) magnification are shown at the bottom (n = 6 independent experiments). White arrows highlight colocalization. Scale bar, 15 μ m.

g. Representative time-lapse series of cells co-expressing mCherry-transferrin receptor (TfR), mECFP-Rab11 (gray scale) and GFP-MTM1. White circles represent membrane-bound structures (n = 6 independent experiments). Scale bar, 1 μ m.

h. Quantification of the number of Rab11-associated fission events generated from mCherry-FYVE2X-positive membranes. Cells expressing GFP-Rab11S25N or GFP-Rab11 treated with either DMSO/Scramble siRNA (control), MTM1 siRNA (MTM1-KD), MTM1 siRNA and PI3K-C2α siRNA (MTM1-KD/PI3K-C2α -KD), MTM1 siRNA and VPS34 inhibitor (MTM1-KD/VPS34-IN1), or MTM1 siRNA in combination with PI3K-C2α siRNA and VPS34 inhibitor (MTM1-KD/PI3K-C2α -KD/VPS34-IN1) (n = 12 independent experiments; data represent mean ± s.e.m., ** P < 0.01, *P < 0.05; one-way ANOVA).

i. Residence time of GFP-Rab11S25N or GFP-Rab11 structures on mCherry-FYVE2X-positive membranes (black and blue bars). Cells expressing GFP-Rab11 were treated with either Scramble siRNA (control) or MTM1 siRNA (MTM1-KD). (n = 12 independent experiments; data represent mean ± s.e.m.; ***P < 0.005, **P < 0.01, two-way ANOVA).

j. Quantification of internal transferrin percentage in COS-7 cells expressing GFP-Rab11S25N or GFP-Rab11 treated with either DMSO/Scramble siRNA (control), MTM1 siRNA (MTM1-KD), MTM1 siRNA and PI3K-C2α siRNA (MTM1-KD/PI3K-C2α -KD), MTM1 siRNA and VPS34 inhibitor (MTM1-KD/VPS34-IN1), or MTM1 siRNA in combination with PI3KC2α siRNA and VPS34 inhibitor (MTM1-KD/PI3K-C2α -KD/VPS34-IN1) (n = 12 independent experiments; data represent mean ± s.e.m.; ***P < 0.005, **P < 0.01, *P < 0.05; one-way ANOVA).

k. Quantification of perinuclear localization of fluorescent transferrin in COS-7 cells expressing GFP-Rab11S25N or GFP-Rab11 treated with either DMSO/Scramble siRNA (control), MTM1 siRNA (MTM1-KD), MTM1 siRNA and PI3K-C2α siRNA (MTM1-KD/PI3K-C2α -KD), MTM1 siRNA and VPS34 inhibitor (MTM1-KD/VPS34-IN1), or MTM1 siRNA in combination with PI3K-C2α siRNA and VPS34 inhibitor (MTM1-KD/ PI3K-C2α -KD/VPS34-IN1) (*n* = 12 independent experiments; data represent mean ± s.e.m.; ***P < 0.005, **P < 0.01; one-way ANOVA).

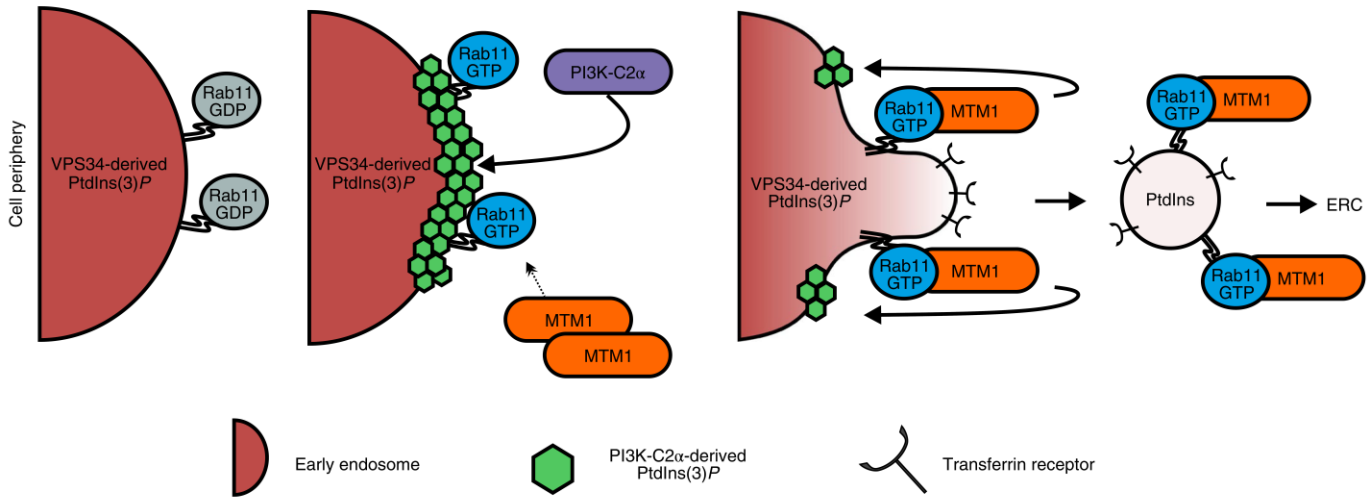

Fig.6: Trafficking of recycling cargo from peripheral endosome to ERC require Rab11 activation and PtdIns(3)P turnover.

On a peripheral PtdIns(3)*P* membrane a transient and local burst of PI3K-C2α -derived PtdIns(3)*P* triggers Rab11 activation (first and second panel from the left). Active Rab11 (Rab11-GTP) recruits MTM1, a PtdIns(3)*P* phosphatase, which catalyzes PtdIns(3)*P* hydrolysis (third panel from the left). PtdIns(3)*P* reduction allows vesicle fission and trafficking of cargo toward the ERC (rightmost panel).

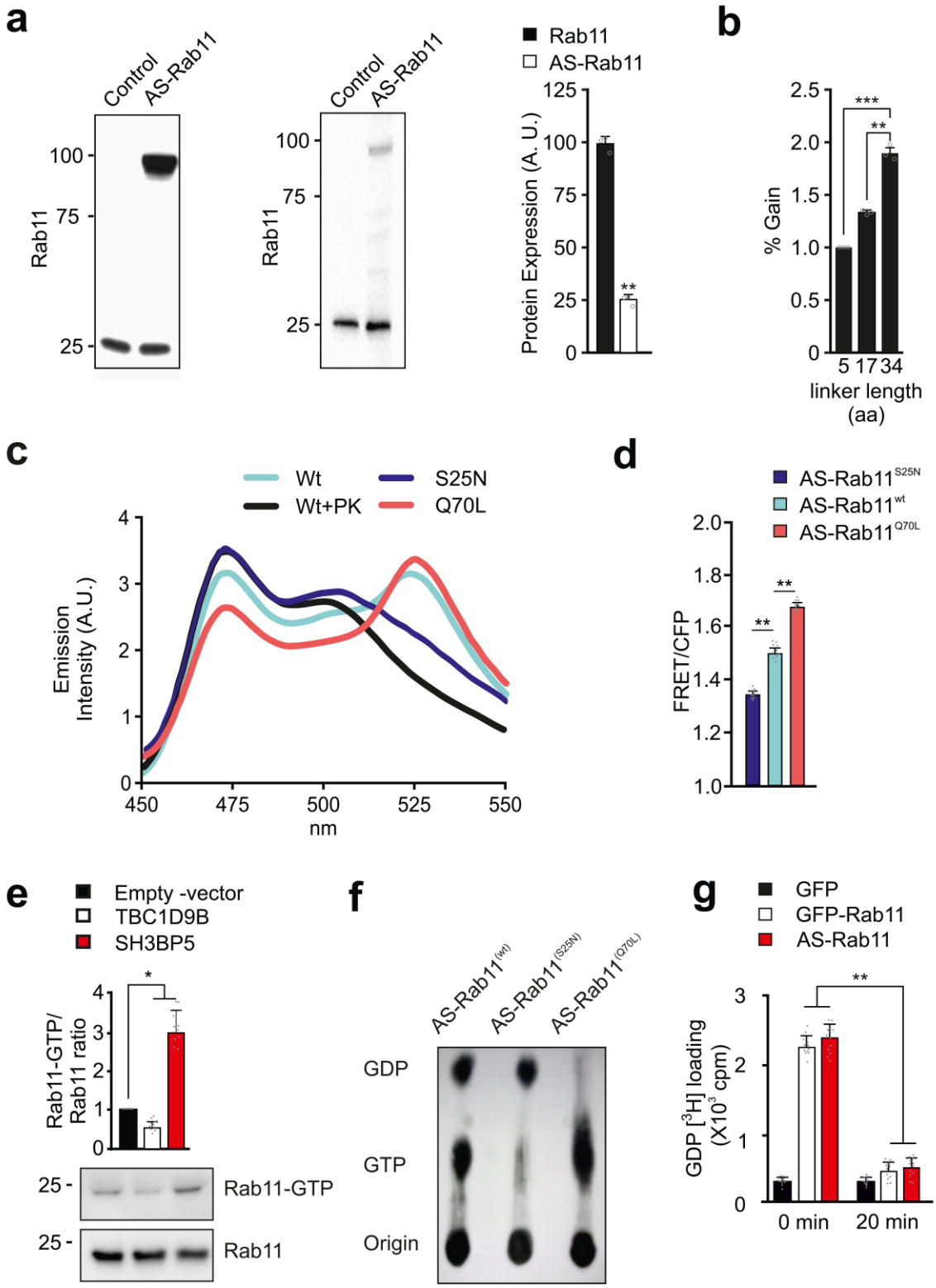
a
Control
AS-Rab11
Rab11
100
75
25
Control
AS-Rab11
Rab11
100
75
25
Rab11
AS-Rab11
Protein Expression (A. U.)
125
100
75
50
25
0
**
b
% Gain
2.5
2.0
1.5
1.0
0.5
0
***
**
5 17 34
linker length
(aa)
c
Wt
Wt+PK
S25N
Q70L
Emission
Intensity (A.U.)
4
3
2
1
0
450
475
500
525
550
nm
d
AS-Rab11S25N
AS-Rab11wt
AS-Rab11Q70L
FRET/CFP
2.0
1.8
1.6
1.4
1.2
1.0
**
**
e
Empty -vector
TBC1D9B
SH3BP5
Rab11-GTP/
Rab11 ratio
4
3
2
1
0
*
25
Rab11-GTP
25
Rab11
f
AS-Rab11(wt)
AS-Rab11(S25N)
AS-Rab11(Q70L)
GDP
GTP
Origin
g
GFP
GFP-Rab11
AS-Rab11
GDP [3H] loading
(X103 cpm)
3
2
1
0
**
0 min
20 min

Suppl. Fig. 1: Biochemical characterization of the FRET biosensor AS-Rab11.

a. Representative immunoblot of AS-Rab11 expressed in HEK293T cells (left panel). Representative immunoblot of AS-Rab11 expressed in COS-7 cells (middle panel), and quantification of endogenous Rab11 (black bar) and transfected AS-Rab11 in a typical time lapse experiment (white bar) (n=3 independent experiments) (uncropped blots are shown in Supplementary Figure 8).

b. Quantification of FRET efficiency gain (AS-Rab11Q70L (n)/AS-Rab11S25N (n), (n=linker length)) measured for three different AS-Rab11 constructs containing 5, 17 and 34 amino acids linkers (n=3 independent experiments; data represent mean ± SEM, ** $p< 0.01$, t-test).

c. Representative fluorescence emission spectra of AS-Rab11wt (cyan line), AS-Rab11wt treated with proteinase K (black line), dominant negative (AS-Rab11S25N, blue line) and constitutively active (AS-Rab11Q70L, red line) mutants excited at 433 nm (n=6 independent experiments).

d. Quantification of FRET/CFP emission ratio in cells expressing AS-Rab11 wild-type (cyan bar) and its dominant active (As-Rab11Q70L, red bar) and inactive (As-Rab11S25N, blue bar) form by confocal microscopy (n=10 independent experiments; data represent mean ± SEM, ** $p< 0.01$, *** $p< 0.005$, One-way ANOVA).

e. Quantification and representative immunoblot of Rab11-GTP content in HEK293T cells expressing the Rab11 GEF SH3BP5 (red bar) and the Rab11 GAP TBC1D9B (white bar) or empty plasmid vector (black bar) (n=10 independent experiments; data represent mean ± SEM, * $p< 0.05$, One-way ANOVA) (uncropped blots are shown in Supplementary Figure 8).

f. Analysis of AS-Rab11-GDP and AS-Rab11-GTP levels in cell transfected with either wildtype (AS-Rab11WT) or constitutively active (AS-Rab11Q70L) or dominant negative (AS-Rab11S25N) biosensor versions. Separation of labelled 32Pi nucleotides was performed by TLC (Thin layer chromatography) and imaged by autoradiography (n=3 independent experiments) (uncropped blots are shown in Supplementary Figure 8).

g. Guanine nucleotide displacement assay of immunoprecipitated GFP, GFP-Rab11 and ASRab11 (n=12 independent experiments, data represent mean ± SEM, ** $p< 0.01$, Two-way ANOVA).

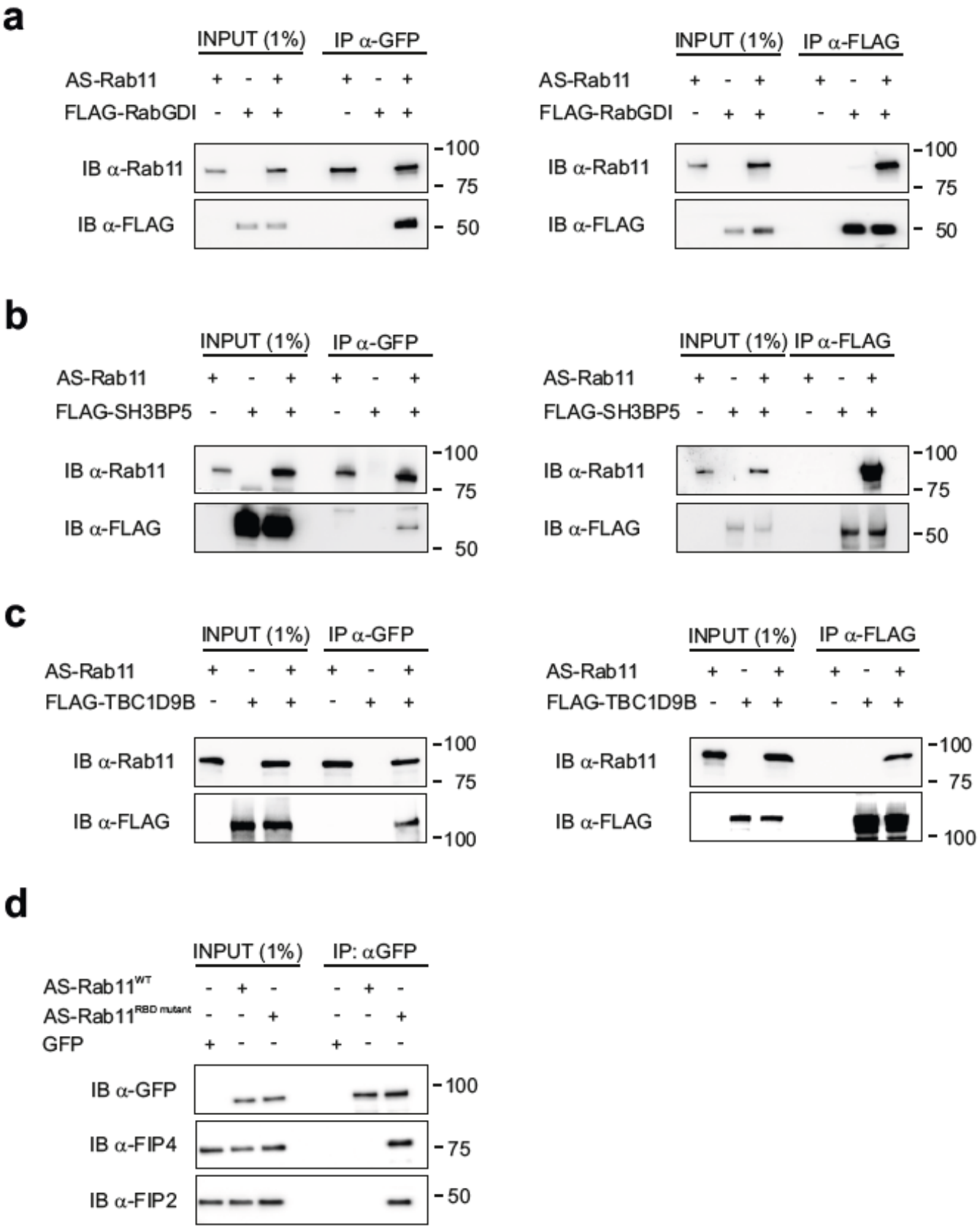
a
INPUT (1%)
IP α-GFP
AS-Rab11 + - + + - +
FLAG-RabGDI - + + - + +
IB α-Rab11
IB α-FLAG
100
75
50
INPUT (1%)
IP α-FLAG
AS-Rab11 + - + + - +
FLAG-RabGDI - + + - + +
IB α-Rab11
IB α-FLAG
100
75
50
b
INPUT (1%)
IP α-GFP
AS-Rab11 + - + + - +
FLAG-SH3BP5 - + + - + +
IB α-Rab11
IB α-FLAG
100
75
50
INPUT (1%)
IP α-FLAG
AS-Rab11 + - + + - +
FLAG-SH3BP5 - + + - + +
IB α-Rab11
IB α-FLAG
100
75
50
c
INPUT (1%)
IP α-GFP
AS-Rab11 + - + + - +
FLAG-TBC1D9B - + + - + +
IB α-Rab11
IB α-FLAG
100
75
100
INPUT (1%)
IP α-FLAG
AS-Rab11 + - + + - +
FLAG-TBC1D9B - + + - + +
IB α-Rab11
IB α-FLAG
100
75
100
d
INPUT (1%)
IP: αGFP
AS-Rab11WT - + - - + -
AS-Rab11RBD mutant - - + - - +
GFP + - - + - -
IB α-GFP
IB α-FIP4
IB α-FIP2
100
75
50

Suppl. fig. 2: AS-Rab11 interacts with positive and negative Rab11 regulators.

a. Representative immunoblot of AS-Rab11^{wt} co-immunoprecipitation with FLAG-tagged RabGDI performed in HEK293T cells transfected with either AS-Rab11^{wt} or FLAG-RabGDI or both (n=4 independent experiments, left and right panel).

b. Representative immunoblot of AS-Rab11^{wt} co-immunoprecipitation with FLAG-tagged SH3BP5, a Rab11 GEF, performed in HEK293T cells transfected with either AS-Rab11^{wt} or FLAG-SH3BP5 or both (n=4 independent experiments, left and right panel).

c. Representative immunoblot of AS-Rab11^{wt} co-immunoprecipitation with FLAG-tagged TBC1D9B, a Rab11 GAP, performed in HEK293T cells transfected with either AS-Rab11^{wt} or FLAG-TBC1D9B or both (n=4 independent experiments, left and right panel).

d. Representative immunoblot of AS-Rab11^{wt} and AS-Rab11$^{RBD\ mutant}$ co-immunoprecipitation with endogenous Rab11-FIP2 and Rab11-FIP4 performed in HEK293T cells transfected with either AS-Rab11^{wt} or AS-Rab11$^{RBD\ mutant}$ (n=4 independent experiments).

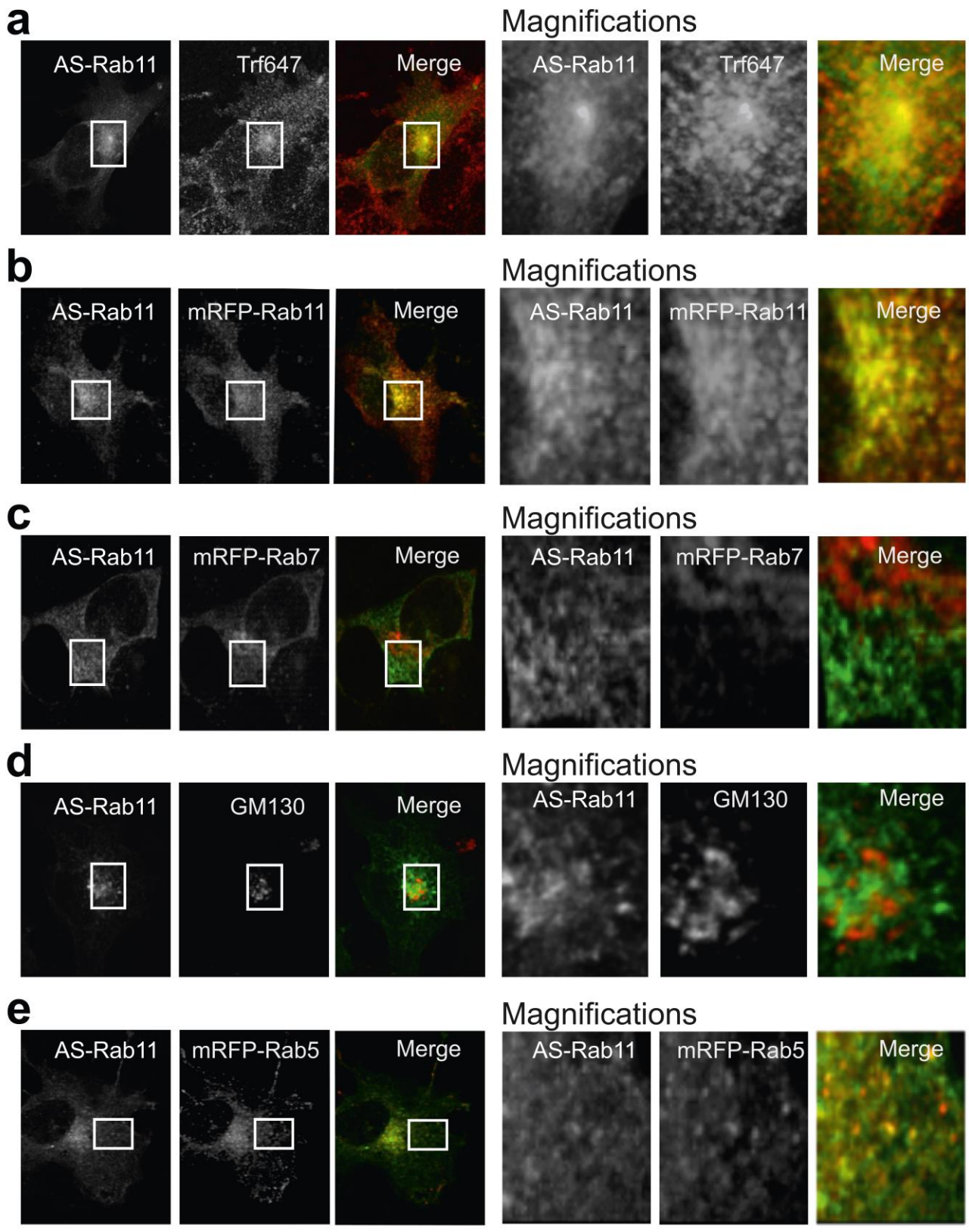
a
AS-Rab11
Trf647
Merge
Magnifications
AS-Rab11
Trf647
Merge
b
AS-Rab11
mRFP-Rab11
Merge
Magnifications
AS-Rab11
mRFP-Rab11
Merge
c
AS-Rab11
mRFP-Rab7
Merge
Magnifications
AS-Rab11
mRFP-Rab7
Merge
d
AS-Rab11
GM130
Merge
Magnifications
AS-Rab11
GM130
Merge
e
AS-Rab11
mRFP-Rab5
Merge
Magnifications
AS-Rab11
mRFP-Rab5
Merge

Suppl. fig. 3: Characterization of the FRET biosensor AS-Rab11 localization.

a. Representative images of AS-Rab11 localization on fluorescent transferrin positive structures. Magnification of the surrounded region is shown on the right (n=3 independent experiments).

b. Representative images of AS-Rab11 localization on mRFP-Rab11 positive structures. Magnification of the surrounded region is shown on the right (n=3 independent experiments).

c. Representative images of AS-Rab11 localization on mRFP-Rab7 positive structures. Magnification of the surrounded region is shown on the right (n=3 independent experiments).

d. Representative images of AS-Rab11 localization on GM-130 positive structures. Magnification of the surrounded region is shown on the right (n=3 independent experiments).

e. Representative images of AS-Rab11 localization on mRFP-Rab5 positive structures. Magnification of the surrounded region is shown on the right (n=3 independent experiments).

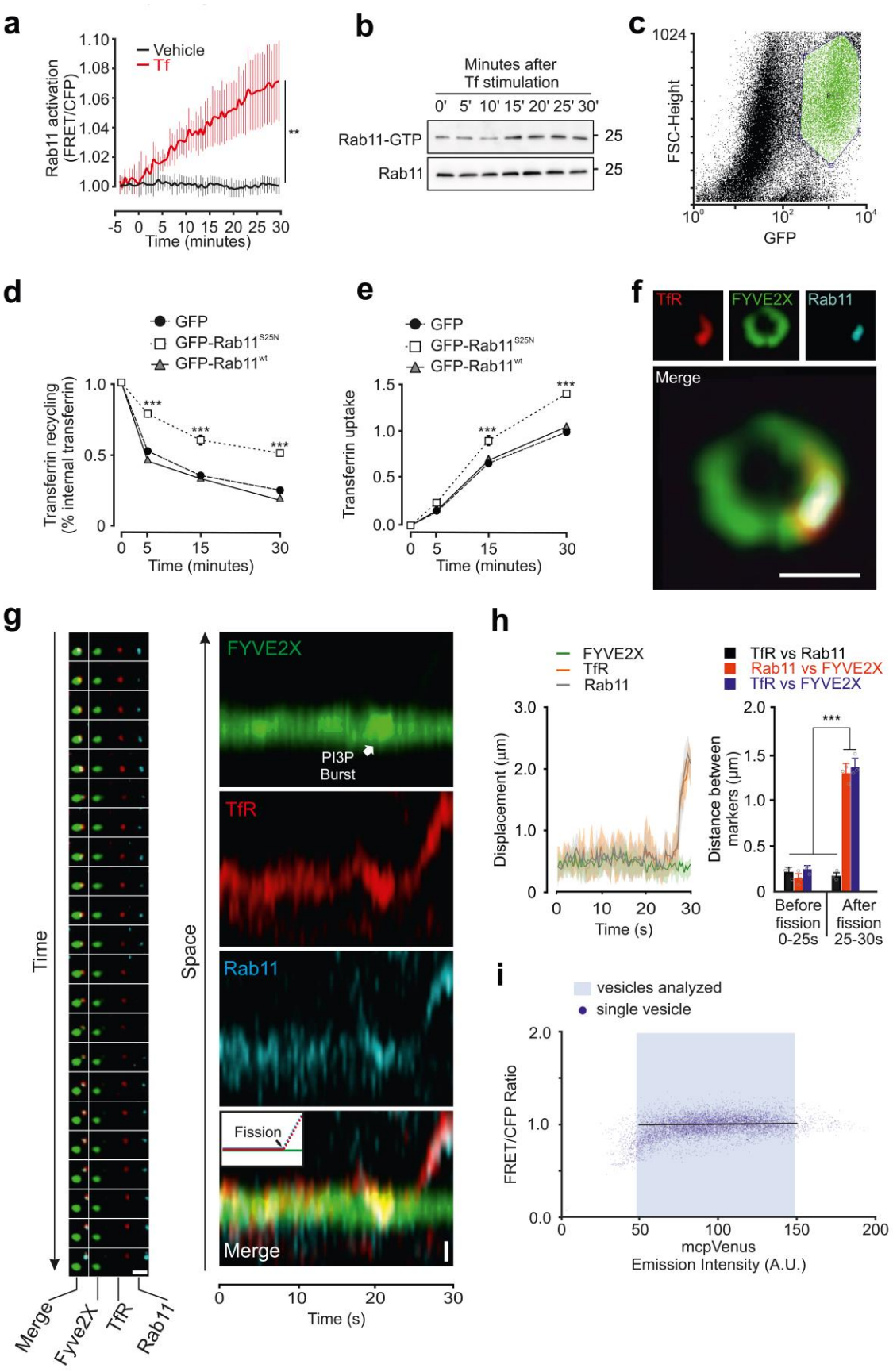
a
Rab11 activation (FRET/CFP)
Vehicle
Tf
Time (minutes)
b
Minutes after Tf stimulation
0' 5' 10' 15' 20' 25' 30'
Rab11-GTP
Rab11
c
FSC-Height
GFP
d
GFP
GFP-Rab11S25N
GFP-Rab11wt
Transferrin recycling (% internal transferrin)
Time (minutes)
e
Transferrin uptake
Time (minutes)
f
TfR
FYVE2X
Rab11
Merge
g
Time
Space
FYVE2X
PI3P Burst
TfR
Rab11
Fission
Merge
Time (s)
Merge
Fyve2X
TfR
Rab11
h
FYVE2X
TfR
Rab11
TfR vs Rab11
Rab11 vs FYVE2X
TfR vs FYVE2X
Displacement (µm)
Time (s)
Distance between markers (µm)
Before fission 0-25s
After fission 25-30s
i
vesicles analyzed
single vesicle
FRET/CFP Ratio
mcpVenus Emission Intensity (A.U.)

Suppl. fig. 4: Rab11 activation controls Tf recycling.

a. Quantification of Rab11 activation in COS-7 cells. Cells were treated with either vehicle (black line), or transferrin at 0 minutes (red line) (n=14 independent experiments; data represent mean ± SEM, ** $p< 0.01$, Two-way ANOVA).

b. Representative immunoblot of Rab11-GTP content in COS-7 cells treated for 0, 5, 10, 15, 20, 25, and 30 minutes with transferrin (n=4 independent experiments).

c. Representative scatter plot for the gating strategy used on transferrin treated cells. GFP fluorescence intensity and forward scatter (FSC) area were used as an initial gate for untransfected cells, cell debris and aggregates.

d. Transferrin recycling in cells expressing either GFP, GFP-Rab11^{S25N} or GFP-Rab11^{wt}. Transferrin recycling was analyzed by flow cytometry at 0, 5, 15 and 30 minutes after transferrin treatment (n=4 independent experiments; data represent mean ± SEM, *** $p< 0.005$, Two-way ANOVA).

e. Transferrin uptake in cells expressing either GFP, GFP-RAB11^{S25N} or GFP-RAB11^{wt}. Transferrin uptake was analyzed by flow cytometry at 0, 5, 15 and 30 minutes after transferrin treatment (n=4 independent experiments; data represent mean ± SEM, *** $p< 0.005$, Two-way ANOVA).

f. Representative image of a double positive TfR (mCherry-TfR) and Rab11 (mECFP-Rab11) membrane domain on PtdIns(3)P$^+$ (GFP-FYVE2X) structure (scale bar 1µm).

g. Representative time-lapse series of a double positive TfR (mCherry-TfR) and Rab11 (mECFP-Rab11) vesicle detaching from a PtdIns(3)P$^+$ (GFP-FYVE2X) structure (left panel). Corresponding kymograph from 30 seconds time series imaged every 1 s by confocal microscopy. (the fission event correspond to the time series shown in Fig. 3a) (n=3 independent experiments; scale bar 500 nm).

h. Distance from the origin (Displacement) of mCherry-Transferrin Receptor (TfR), GFP-FYVE2X (FYVE2X) and mECFP-Rab11 (Rab11) positive structures as a function of time (left panel) and the distance between couples of markers, before and after the fission event (right panel).

(n=20 fission events from 3 independent experiments; data represent mean ± SEM, *** $p < 0.005$, One-way ANOVA).

i. Titration of FRET/CFP ratio as a function of AS-Rab11 biosensor abundance (mcpVenus emission intensity) in AS-Rab11 expressing cells (blue dots represent single vesicles analyzed) (n=4 independent experiments).

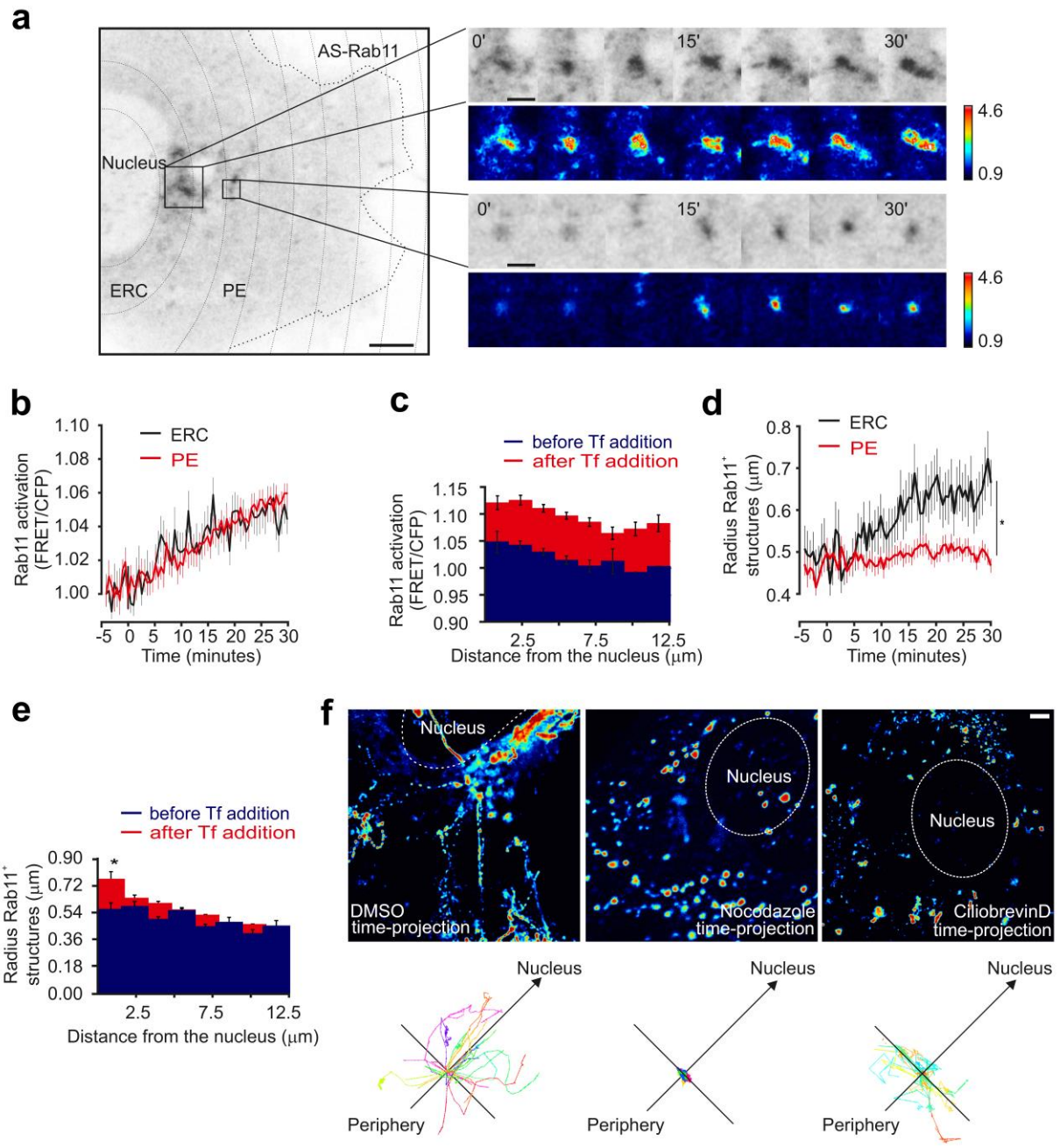
a
AS-Rab11
Nucleus
ERC
PE
0'
15'
30'
4.6
0.9
b
ERC
PE
Rab11 activation (FRET/CFP)
Time (minutes)
c
before Tf addition
after Tf addition
Rab11 activation (FRET/CFP)
Distance from the nucleus (μm)
d
ERC
PE
Radius Rab11+ structures (μm)
Time (minutes)
e
before Tf addition
after Tf addition
Radius Rab11+ structures (μm)
Distance from the nucleus (μm)
f
Nucleus
DMSO time-projection
Nocodazole time-projection
CiliobrevinD time-projection
Periphery
g
DMSO
Nocodazole
CiliobrevinD
Rab11S25N
Internal Tf (%total)
Time (minutes)
h
DMSO
Nocodazole
CiliobrevinD
Rab11S25N
Internal Tf (%total)

Suppl. fig. 5: Rab11 is activated on both peripheral and juxtanuclear membranes.

a. Representative images of Rab11 membrane-bound structures (the scale bar represents 5 µm) and their magnifications (the scale bar represents 1 µm) in perinuclear and peripheral area at 0, 5, 10, 15, 20 ,25, and 30 minutes after transferrin stimulation. AS-Rab11 and FRET/CFP images are shown.

b. Rab11 activation calculated as FRET/CFP ratio for ERC (black curve) and PE (red curve) membrane bound Rab11 structures plotted as a function of time, after transferrin stimulation at 0 minutes (n=14 independent experiments; data represent mean ± SEM, Two-way ANOVA).

c. Measurement of FRET/CFP ratio on Rab11 membrane-bound structures before (blue bars) and after (red bars) 30 minutes of transferrin stimulation plotted as a function of distance from nucleus (n=14 independent experiments; data represent mean ± SEM, Two-way ANOVA)

d. Measurement of radius for ERC (black curve) and PE (red curve) membrane-bound Rab11 structures plotted as a function of time, after transferrin stimulation at 0 minutes. (n=14 independent experiments; data represent mean ± SEM, * $p< 0.05$, Two-way ANOVA).

e. Measurement of radius of membrane-bound Rab11 structures before (blue bars) and after (red bars) 30 minutes of transferrin stimulation plotted as a function of distance from nucleus (n=14 independent experiments; data represent mean ± SEM, * $p< 0.05$, Two-way ANOVA).

f. Representative time-projection of active-Rab11 (pseudocolor mode) vesicle trafficking towards the ERC treated with either vehicle (DMSO), microtubule depolymerizing agents (Nocodazole) or dynein inhibitor (Ciliobrevin D) (upper panel). Both direction and trajectory of an active Rab11 vesicle are represented as a line starting from the intersection between the two axes, in which the longest represents the peripheral to nuclear direction (lower panel) (n=10 independent experiments). The scale bar represents 1 µm.

g. Quantification of internal transferrin in cells treated with either DMSO (black curve), Nocodazole (red curve), Ciliobrevin D (blue curve) or expressing GFP-Rab11S25N (green curve). Internalized transferrin was analyzed by flow cytometry at 0, 5, 15 and 30 minutes after transferrin

treatment. (n=4 independent experiments; data represent mean ± SEM, *** p< 0.005, Two-way ANOVA).

h. Quantification of internal transferrin percentage in COS-7 cells treated with either DMSO (Control, black bar), Nocodazole (red bar), Ciliobrevin D (blue bar), or expressing GFP-Rab11S25N (green bar) after 30 minutes of transferrin treatment (n=12 independent experiments; data represent mean ± SEM, *** p< 0.005, One-way ANOVA).

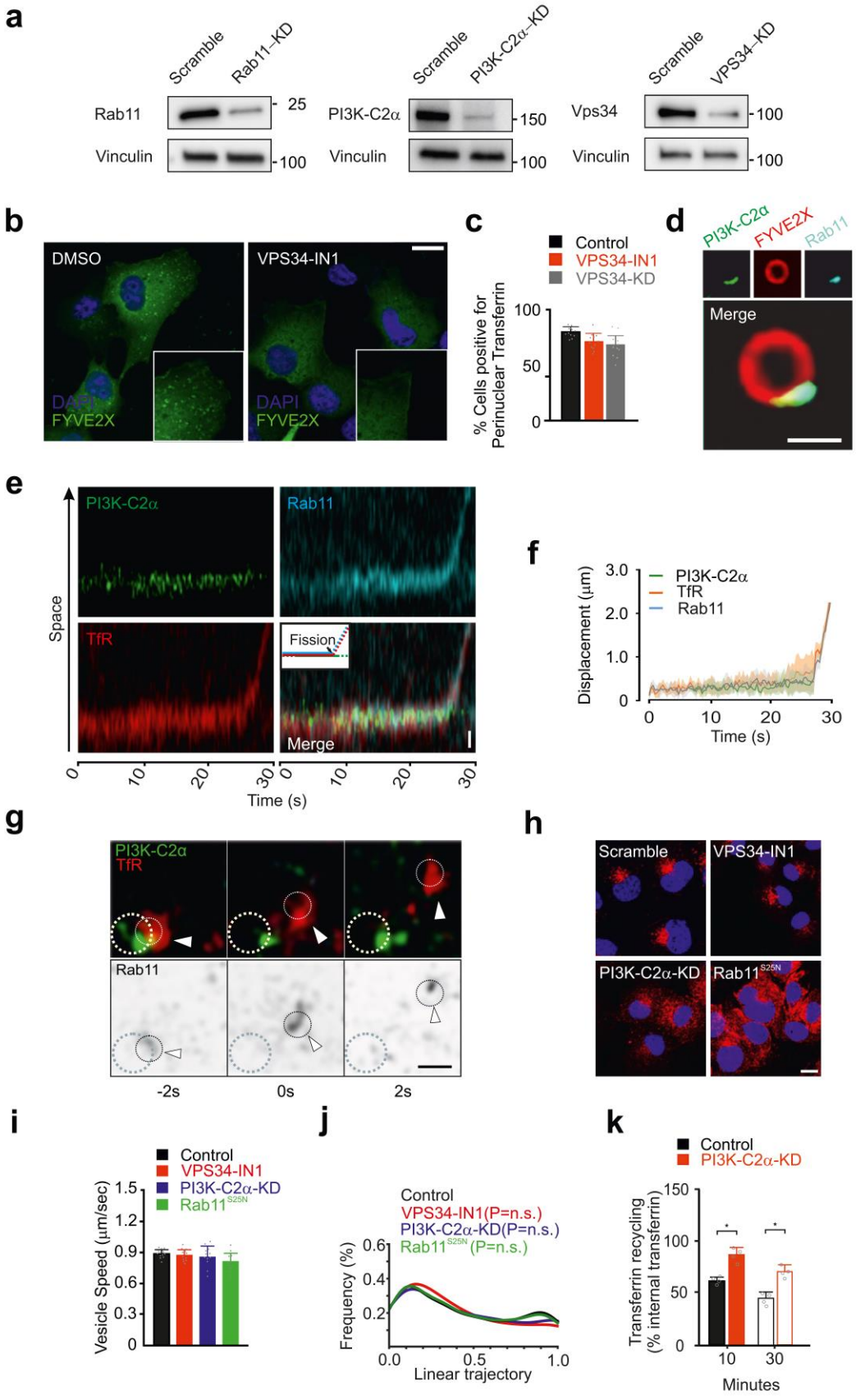
a
Scramble
Rab11-KD
Rab11
25
Vinculin
100
Scramble
PI3K-C2α-KD
PI3K-C2α
150
Vinculin
100
Scramble
VPS34-KD
Vps34
100
Vinculin
100
b
DMSO
VPS34-IN1
DAPI
FYVE2X
c
Control
VPS34-IN1
VPS34-KD
% Cells positive for Perinuclear Transferrin
100
50
0
d
PI3K-C2α
FYVE2X
Rab11
Merge
e
PI3K-C2α
Rab11
TfR
Fission
Merge
Space
0
10
20
30
Time (s)
f
PI3K-C2α
TfR
Rab11
Displacement (μm)
3.0
2.0
1.0
0
0
10
20
30
Time (s)
g
PI3K-C2α
TfR
Rab11
-2s
0s
2s
h
Scramble
VPS34-IN1
PI3K-C2α-KD
Rab11S25N
i
Control
VPS34-IN1
PI3K-C2α-KD
Rab11S25N
Vesicle Speed (μm/sec)
1.5
1.2
0.9
0.6
0.3
0
j
Control
VPS34-IN1(P=n.s.)
PI3K-C2α-KD(P=n.s.)
Rab11S25N (P=n.s.)
Frequency (%)
0.6
0.4
0.2
0.0
0.5
1.0
Linear trajectory
k
Control
PI3K-C2α-KD
Transferrin recycling (% internal transferrin)
150
100
50
0
10
30
Minutes

Suppl. fig. 6: PI3K-C2α controls Tf recycling without impacts on Rab11 vesicle speed and trajectory.

a. Representative immunoblot of Rab11 content in COS-7 cells treated with either scramble or Rab11 siRNAs (Rab11-KD) (left panel). Representative immunoblot of PI3K-C2α content in COS7 cells treated with either scramble or PI3K-C2α siRNAs (PI3K-C2α-KD) (middle panel). Representative immunoblot of Vps34 content in COS-7 cells treated with either scramble or Vps34 siRNAs (VPS34-KD) (right panel). (n=3 independent experiments) (uncropped blots are shown in Supplementary Figure 8).

b. Representative images of PtdIns(3)P content in COS-7 cells treated with either DMSO or VPS34 inhibitor (VPS34-IN1) (n=4 independent experiments). The scale bar represents 1 µm.

c. Quantification of perinuclear localization of fluorescent transferrin in cells treated with either scramble/DMSO (control, black bar), VPS34 inhibitor (VPS34-IN1, red bar), or VPS34 siRNA (VPS34-KD, grey bar) (n=12 independent experiments; data represent mean ± SEM, Oneway ANOVA).

d. Representative image of double positive Rab11 (mECFP-Rab11) and PI3K-C2α (GFPPI3K-C2α) membrane domain on a PtdIns(3)P+ (mCherry-FYVE2X) structure. The scale bar represents 1 µm.

e. Representative kymograph of a double positive Rab11 (mECFP-Rab11) and TfR (mCherryTfR) membrane detaching from PI3K-C2α (GFP-PI3K-C2α) positive structure. 30 seconds time series imaged every 1 s by confocal microscopy. (n=3 independent experiments). The scale bar represents 250 nm.

f. Distance from the origin (Displacement) of mCherry-Transferrin Receptor (TfR), GFPPI3K-C2α (PI3K-C2α) and mECFP-Rab11 (Rab11) positive structures as a function of time. (n=20 fission events from 3 independent experiments).

g. Representative time-lapse series of cells co-expressing mCherry-Transferrin receptor (TfR), mECFP-Rab11 (gray scale) and GFP-PI3K-C2α. White circles represent membrane bound

structures. White arrows indicate Rab11 positive vesicle separating from a peripheral endosome (n=6 independent experiments). The scale bar represents 1 μm. 10

h. Representative image of endocytosed transferrin localization in cells expressing GFPRab11S25N (Rab11S25N) or GFP-Rab11 treated with either scramble/DMSO (Scramble), VPS34 inhibitor (VPS34-IN1), or PI3K-C2α siRNAs (PI3K-C2α-KD) (n=4 independent experiments). The scale bar represents 10 μm.

i. Quantitation of Rab11+ vesicle speed in cells expressing GFP-Rab11S25N (green bar) or GFP-Rab11 treated with either Scramble/DMSO (black bar), VPS34 Inhibitor (red bar), or PI3KC2α siRNA (blue bar) (n=12 independent experiments; data represent mean ± SEM, One-way ANOVA).

j. Frequency percentage of Rab11 positive vesicle linearity of movement in cells expressing GFP-Rab11S25N (green curve) or GFP-Rab11 treated with either Scramble/DMSO (black curve), VPS34 Inhibitor (red curve), or PI3K-C2α siRNA (blue curve) (n=4 independent experiments; ttest).

k. Quantitation of transferrin recycling in cells treated either with scramble (Control) or PI3KC2α siRNA (PI3K-C2α-KD) at different time points (n=4 independent experiments; data represent mean ± SEM, * $p < 0.05$, Two-way ANOVA).

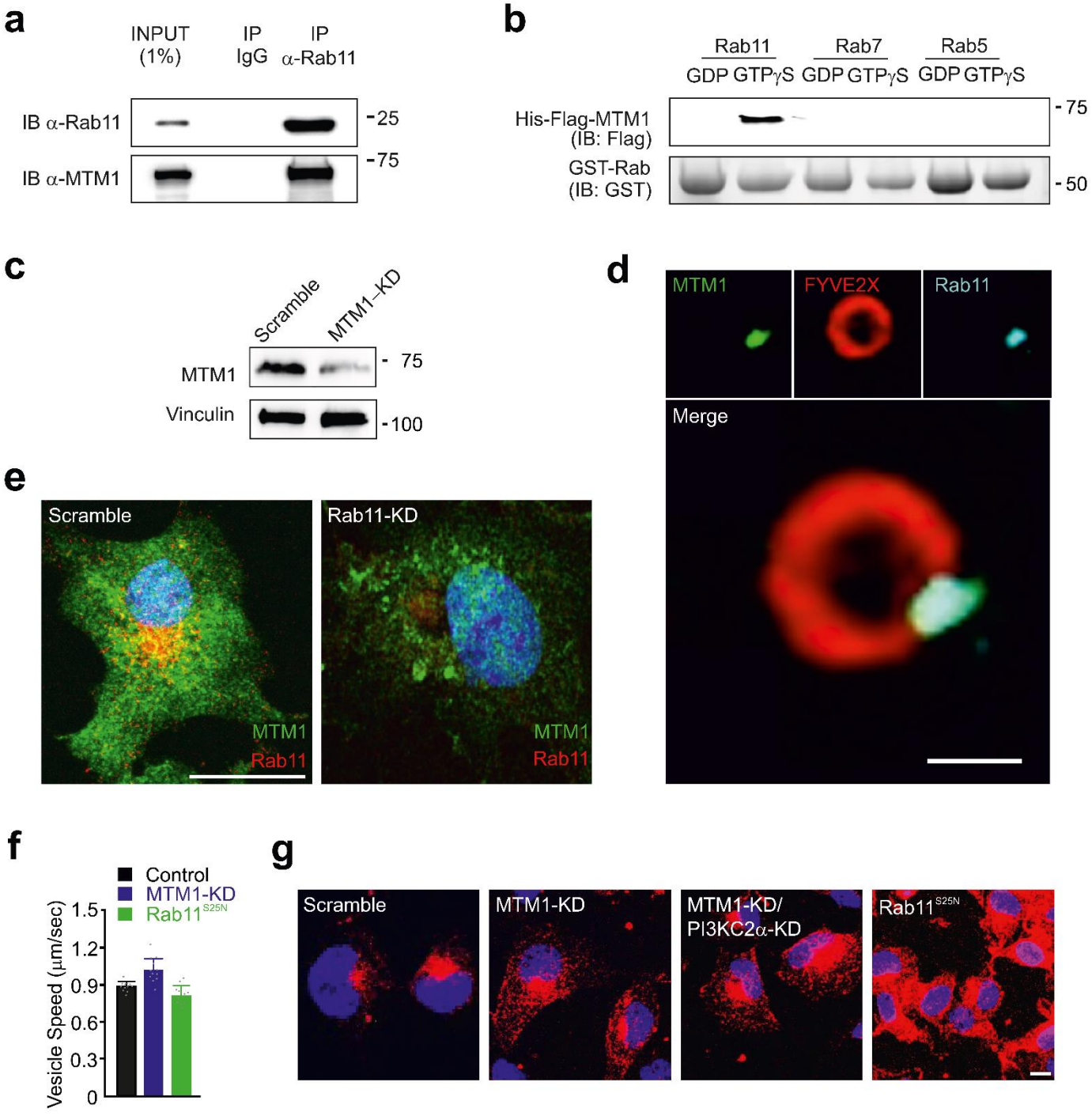
a
INPUT (1%)
IP IgG
IP α-Rab11
IB α-Rab11
IB α-MTM1
25
75
b
Rab11
Rab7
Rab5
GDP GTPγS GDP GTPγS GDP GTPγS
His-Flag-MTM1 (IB: Flag)
GST-Rab (IB: GST)
75
50
c
Scramble
MTM1-KD
MTM1
Vinculin
75
100
d
MTM1
FYVE2X
Rab11
Merge
e
Scramble
Rab11-KD
MTM1
Rab11
f
Control
MTM1-KD
Rab11S25N
Vesicle Speed (μm/sec)
1.5
1.2
0.9
0.6
0.3
0
g
Scramble
MTM1-KD
MTM1-KD/ PI3KC2α-KD
Rab11S25N

Suppl. fig. 7: MTM1 is a Rab11 effector controlling perinuclear Transferrin accumulation.

a. Representative immunoblot of Rab11 co-immunoprecipitation with MTM1 performed in COS-7 cells (n=4 independent experiments).

b. In vitro binding assay of MTM1 and Rabs interaction. Representative western blot of either recombinant Rab11 or Rab7 or Rab5 loaded with GDP or Rab11-GTP□S and probed for recombinant MTM1 interaction (n=4 independent experiments).

c. Representative immunoblot of MTM1 content in COS-7 cells treated with either scramble or MTM1 siRNAs (MTM1-KD) (n=3 independent experiments).

d. Representative image of double positive Rab11 (mECFP-Rab11) and MTM1 (GFP-MTM1) membrane domain on a PtdIns(3)P+ (mCherry-FYVE2X) structure (scale bar 1µm).

e. Representative images of Rab11 colocalization with MTM1 in COS-7 cells treated with either scramble (Control) or Rab11 siRNA (Rab11-KD) (n=4 independent experiments).

f. Quantification of $Rab11^{+}$ vesicle speed in cells expressing GFP-$Rab11^{S25N}$ (green bar) or GFP-Rab11 treated with either Scramble (black bar), or MTM1 siRNA (blue bar) (n=12 independent experiments; data represent mean ± SEM, One-way ANOVA).

g. Representative images of internalized transferrin in COS-7 cells expressing GFP-$Rab11^{S25N}$ ($Rab11^{S25N}$) or GFP-Rab11 treated with either Scramble siRNA (Scramble), MTM1 siRNA (MTM1-KD), or MTM1 and PI3K-C2α siRNAs (MTM1-KD/ PI3K-C2α) (n=12 independent experiments).

Chapter II

Elucidating the role of PI3K-C2α in modulating glucose homeostasis

Materials and Methods

Animals

Pi3kc2a conditional KO mice were generated using Knock-out first strategy. For this purpose, recombined mouse embryonic stem cells were received from International mouse phenotyping consortium (IMPC) carrying Knock-out first allele (Pik3c2a$^{tm1a(EUCOMM)Hmgu}$) . This allele contained LacZ, Neo cassettes along with FRT sites as well as loxP sites inserted in around exon 3 of *Pi3kc2a* gene as described in Figure 1, a. The neomycin cassette permitted G418 selection of transfected ES cells and the positive ES clones were then injected in the blastocyst. The resulting chimeric founder mice were then crossed with transgenic mice expressing the Flp recombinase under beta-actin promoter (B6.Cg-Tg(ACTFLPe)9205Dym/J), Jackson Laboratory) to eliminate lacZ and neomycin cassettes generating homozygous Pi3kc2a$^{fl/fl}$ mice. Subsequently, Pi3kc2a$^{fl/fl}$ mice were crossed with Cre transgenic mice (B6.Cg-Tg(CAG-cre/Esr1*)5Amc/J, Jackson Laboratory) in order to generate *Pi3kc2a*$^{fl/fl}$*Cre*$^{+}$ and *Pi3kc2a*$^{fl/fl}$*Cre*$^{-}$ mice. Cre recombinase was activated using 2 mg/kg tamoxifen (Sigma-aldrich, (10% ethanol + 90% corn oil) treatment through oral gavage for 4 consecutive days to induce systemic deletion of PI3K-C2α in 6-8 weeks old *Pi3kc2a*$^{fl/fl}$*Cre*$^{+}$ mice (KO mice). *Pi3kc2a*$^{fl/fl}$*Cre*$^{-}$ and *Pi3kc2a*$^{wt/wt}$*Cre*$^{+}$ mice received the same tamoxifen treatment and were used as experimental controls (Control mice).

For liver specific deletion of *Pi3kc2a*, 6-8 weeks old *Pi3kc2a*$^{fl/fl}$*Cre*$^{-}$ mice were injected with 1x10^{11} genome copies of AAV8-TBG-iCre (Vector Bioloabs, Rockville, MD, USA) to induce liver specific expression on Cre recombinase. *Pi3kc2a*$^{wt/wt}$*Cre*$^{-}$ mice received the same dosage of AAV8-TBG-iCre and were used as experimental controls.

All mice were from C57/Bl6 background. They were born healthy and according to mendelian ratio. Animals were kept in SPF rooms in temperature and light controlled environment and fed standard chow diet *ad libitum* (unless starved for experiments) and had free access to water. Mice were genotyped using genomic DNA isolated from tails and these PCR primers: Cre_Tmx Fwd: 5'-TTTGGGCCAGCTAAACATGC-3' Rev: 5'-TTACGTATATCCTGGCAGCG-3'; Pik3c2aFlox Fwd: 5'-AGTCCCAAATGAGCTTGCTCTCTTC-3' Rev: 5'-ACGTAGTAGCACCCACAAGC-3'. All the animal use followed institutional animal welfare guidelines and legislation, as approved by the local Animal Ethics Committee (Comitato di Bioetica e Valutazione, Torino, Italy). Glucose/ Insulin/ Glucagon/ Pyruvate tolerance tests and glucose measurement studies were performed on 3rd day of tamoxifen administration.

Histology and immunohistochemistry

Harvested mouse liver tissue were fixed in 4% Paraformaldehyde (PFA) and embedded in paraffin. 5-µm sections were processed with routine hematoxylin and eosin (H&E) staining method. Immunohistochemistry (IHC) analysis was performed with primary antibody specific for Phosphoinositide 3-Kinase-C2-Alpha (Pik3c2a) (Mouse IgG, Clone OTI2C11, Origene). For ORO (Oil Red O) staining, harvested liver samples were frozen in OCT compound (VWR BDH Prolabo) and 10-µm sections were cut with the help of cryostat. Cut frozen sections were stained with Oil Red O (Sigma) solution and counterstained with hematoxylin. TUNEL assay was performed to evaluate apoptosis in sections. 3-µm liver tissue sections were assessed using In Situ Cell Death Detection Kit, per the manufacturer's instructions (Roche, West Sussex, UK). Digital images for H and E, IHC and ORO staining were captured using Olympus BX41 Phase Contrast & Darkfield Microscope. TUNEL stained sections were examined using Zeiss Observer-Z1 microscope, equipped with the Apotome.

Glucose and insulin tolerance

Glucose and insulin tolerance test were performed on 3rd day of tamoxifen treatment. Mice were starved for 6 hours before injecting a glucose (Sigma) load of 2g/kg of body weight or with insulin (Sigma) dose of 0.75U/kg of body weight intraperitoneally, respectively. Blood glucose concentration was determined using blood collected from the tip of tail vein with the help of glucometer and Accu-Chek Active strips (Roche) at different timepoints of 0, 5, 15, 30, 45, 60, 90 and 120 mins.

Ketone bodies and insulin

Concentrations of ketone bodies in serum and in liver tissue samples were determined using a colorimetric diagnostic kit (Cayman Chemical Company, Ann Arbor, MI, USA). Ultra-Sensitive Mouse Insulin ELISA kit was used to access serum insulin concentration (Cat No. 90080, Crystal Chem).

Fatty acid β-oxidation

Long-chain fatty acid β-oxidation was measured as detailed in (Buondonno et al., 2016). Briefly, the precipitates, containing 14C-acid soluble metabolites (ASM), were collected. The radioactivity of each sample was counted by liquid scintillation. Results are expressed as nmol/min/mg cellular proteins. In each experimental set, liver homogenates were preincubated for 30 minutes with the carnitine palmitoyltransferase inhibitor etomoxir (1 mmol/L) or with the AMPkinase activator 5-aminoimidazole-4-carboxamide ribonucleotide (AICAR; 1 mmol/L), as negative and positive controls, respectively. In the presence of etoxomir, the rate of fatty acid β-oxidation was less than 10% than in its absence; in the presence of AICAR, the rate of fatty acid β-oxidation was increased 2-fold.

Cholesterol, cholesterol esters and triglyceride measurement in liver homogenates

The amount of cholesterol and cholesterol esters was measured spectrofluorimetrically using the Cholesterol/ Cholesteryl Ester Assay Kit - Quantitation Kit (Abcam; ab65359), following the producer's instructions. The amount of cholesteryl esters were obtained by subtracting the value of free cholesterol from the value of total cholesterol. Results were expressed as μmoles cholesteryl esters/mg cell proteins. The amount of triglycerides (TG) was measured specrofluorimetrically photometrically using the Triglyceride Assay Kit - Quantitation Kit (Abcam, ab65336), following the producer's instructions. Results were expressed as μmoles triglycerides/mg tissue proteins.

Serum metabolite measurement

The following kits were used to measure free fatty acids (FAAs), total cholesterol LDL and HDL cholesterol, and TG in serum, as per manufacturer's instructions: Free Fatty Acid Assay Kit – Quantification for free fatty acids (Abcam; ab65341); Cholesterol Assay Kit - HDL and LDL/VLDL (Abcam; ab65390); Triglyceride Assay Kit - Quantification (Abcam, ab65336). Results were expressed as mg/dl.

Quantitative real-time PCR

Total RNA was isolated from frozen liver tissues using TRIzol reagent (Invitrogen) according to the manufacturer's instructions. 1ug of total RNA was used to synthesize cDNA with

random primers (Superscript™ II Reverse Transcriptase kit, Invitrogen). Quantitative real-time reverse transcriptase PCR (qRT-PCR) was performed on 7900HT Fast Real-Time PCR System. Gene expression data were normalized to 18S expression levels were analyzed using the $2^{-\Delta\Delta CT}$ method.

Hepatic glycogen determination

150 mg of liver incubated 1mL of 30% KOH for 20-30 mins at 95 °C until the complete digestion of tissue. The lysates were neutralized by adding 0.2 ml of saturated Na_2SO_4 and glycogen was subsequently precipitated by adding 2mL of 95% ethanol. Samples were vortexed, kept on ice for 30 mins and were centrifuged at 550g for 30mins. Resulting glycogen pellet was dissolved in 1mL of ddH_2O and 1mL of 5% phenol was added to the re-dissolved pellet and glycogen standards (0, 1, 2, 4, 8 and 10 mg/ml in ddH2O). 5mL of 96-98% H_2SO_4 was then pipetted directly to the standards and unknown sample tubes and the samples were incubated on ice for 30mins before measuring absorbance at 490 nm. Triplicate samples per liver were analysed and data are presented as μg of glycogen units per mg of liver.

BODIPY staining

Cells were plated on collagen coated sterile glass coverslip two days prior to staining. To enhance lipid droplet formation and facilitate detection, cells were supplemented with 300uM oleate for 6 hrs before lipid droplet staining. Cells were washed twice with 1X PBS and fixed with 4% paraformaldehyde (PFA) for 30 mins at room temperature. Cells were then treated with 1 μg/ml $BODIPY^{493/503}$ (Life Technologies, Cat D3922) in 150mM NaCl for 10 min at room temperature. After washing twice with 1X PBS, cells were counterstained with Hoechst 33342 (Sigma, Cat B2261) and the coverslips were mounted on a glass slide with mounting media. Images were obtained with the help of Leica TCS-II SP5 confocal microscope.

Western blot analysis

Protein from frozen liver sections was extracted in cell lysis buffer. Approximately 50ug of protein was separated by SDS– polyacrylamide gel electrophoresis (SDS–PAGE) and transferred to PVDF membranes. Western blot detection was performed using antibodies specific for PI3K-C2α (Mouse IgG, Clone OTI2C11, Origene), Phospho-Akt (Ser473, Cell signalling, 9271), Akt,

pan (C67E7, Cell signalling, 4691), GAPDH (Santa Cruz Biotechnology, CA, USA). The specific signals were amplified by addition of horseradish peroxidase-conjugated secondary antibodies and visualized with enhanced chemiluminescence (ECL from Millipore). The specific signals were amplified by addition of horseradish peroxidase-conjugated secondary antibodies and visualized with enhanced chemiluminescence (ECL from Millipore). Western blotting images were processed using a ChemiDoc XRS digital imaging system with Quantity One 1-D analysis software (Bio-Rad Laboratories, Inc.)

Statistical analysis

All data are expressed as the mean ± SD. Statistical calculations were analyzed with GRAPHPAD PRISM version 6 (Graph- Pad Software, San Diego, CA, USA). Datasets were compared for statistical significance using the two-tailed Student's t test or ANOVA, where appropriate. Statistical significance is indicated as follows: *$p < 0.05$; **$p < 0.01$; ***$p < 0.001$; ****$p<0.0001$. The number of animals in each group is indicated by n.

Results

Systemic deletion of PI3K-C2α impairs the survival in Pi3kc2a$^{fl/fl}$Cre^{+} (KO) mice

There are currently no published data available assessing the organismal role of PI3K-C2α. It has been previously demonstrated that the PI3K-C2α loss causes embryonic lethality during the gestation period due to complex sets of phenotypes (Franco et al., 2014; Yoshioka et al., 2012). In order to bypass this hurdle, a conditional knockout mouse model containing a genetically engineered PI3K-C2α (*Pi3kc2a*) flox/flox allele was generated (Figure 1a). Although neomycin selection cassette served an important purposes during generation of this mouse model, it was argued that it may cause issues in later stages of mouse development and affect the phenotype (Xu et al., 2001). For this reason, neomycin selection cassette was removed my mating the chimeric founder mice (*see materials and methods)* with transgenic mice expressing the FLP recombinase (Supplementary fig 1a). Subsequently, *Pi3kc2a$^{fl/fl}$* mice were crossed with Cre transgenic mice to receive *Pi3kc2a$^{fl/fl}$Cre^{+}* and *Pi3kc2a$^{fl/fl}$Cre^{-}* mice. The off sprigs were born according to Mendelian frequency. To induce Cre recombinase expression and subsequent whole body homozygous inactivation of PI3K-C2α, 6-8 weeks old *Pi3kc2a$^{fl/fl}$Cre^{+}* (hereon referred to as KO mice) mice were treated with tamoxifen for four consecutive days using oral gavage. While, *Pi3kc2a$^{fl/fl}$Cre^{-}* and *Pi3kc2a$^{wt/wt}$Cre^{+}* (hereon referred to as WT mice) mice, that received the same treatment, were used as experimental controls.

Knockout efficiency was accessed in different organs at protein level using western blot and immunohistochemistry analysis. We noticed that, except for heart tissue, all the vital organs of KO mice including liver, testis, spleen, pancreas, kidney, muscle and brain showed significant down regulation of PIKC2A protein compared to WT, confirming a total body knock-out (Figure 1b, Supplementary figure 1b). This systemic deletion of PI3K-C2α severely impacted the survival rate of KO mice, which died or showed severe signs of weakness within 5-6 days of first tamoxifen treatment (Figure 1c). On the other hand, WT mice remained unaffected without exhibiting any phenotype. No changes in body weight, food or water intake were observed between the KO and the WT mice (Supplementary Figure 1c). These results revealed the non-redundant post-natal physiological role of this isoform in adult mice.

PI3K-C2α deletion triggers a phenotype similar to Non-alcoholic fatty liver disease

In order to evaluate the lethal effect of PI3K-C2α deletion, whole blood analysis was performed to uncover any changes in complete blood count (Supplementary figure 2a). Additionally, flow cytometric analysis of bone marrow populations including monocytes, leukocytes, granulocytes and lymphocytes was also carried out in order to identify any haematopoietic pathologies. However, no significant differences were observed in these parameters between KO and WT mice (Supplementary figure 2b). Transthoracic echocardiography also ruled out any alterations in cardiac parameters (Supplementary figure 2c). Nevertheless, hematoxylin and eosin (H&E) morphology analysis revealed liver to be the only organ severely affected by PI3K-C2α deletion. Liver tissue displayed damaged nuclei and increased vacuolation in hepatocytes (Figure 2a). By indicating elevated levels of apoptosis, TUNEL analysis confirmed the damaged nuclei while, on the other hand, Oil red O (ORO) staining confirmed the latter by showing enrichment in lipid droplet accumulation (Figure 2b,c). In line with this view, KO liver tissue also appeared to be pale compared to WT liver tissue (Figure 2d). This liver morphology resembled to Non-alcoholic fatty liver disease (NAFLD) characterized by hepatic triglyceride accumulation and resulting lipotoxicity. Furthermore, siRNA-mediated knockdown of PI3K-C2α in HepG2 cells challenged with oleic acid resulted in elevated levels of lipid deposits accumulation, accessed with the help of BODIPY495/503 staining (Figure 2e). After establishing this phenotype, ratio of of aspartate and alanine aminotransferases (AST and ALT) levels were evaluated. Higher AST/ALT ratio in KO mice corresponded to liver damage (Figure 2f). To validate if the observed phenotype is due to systemic inactivation PI3K-C2α or if it is only associated with liver tissue, we injected *Pi3kc2a*$^{fl/fl}$*Cre*$^{-}$ mice with adeno-associated virus (AAV) containing Cre recombinase under the liver specific human thyroid hormone-binding globulin (TBG) promoter (AAV-TBG-iCre) to induce the expression of Cre recombinase specific to hepatic tissue. In this study, *Pi3kc2a* $^{wt/wt}$ *Cre*$^{-}$ mice were used as experimental controls. Survival curve of *Pi3kc2a*$^{fl/fl}$*Cre*$^{-}$ mice treated with AAV-TBG-iCre showed mortality at around day 17 to day 20 confirming the impact of liver PI3K-C2α loss on mice survival (Figure 2g). In summary, these results suggested that PI3K-C2α deficiency resulted in a liver specific phenotype with lipid droplet enrichment in hepatic cells and subsequent liver damage due to lipotoxicity.

KO mice exhibit severe hypoglycaemia

PIK3C2α overexpression and RNA interference (RNAi)-based studies in cell lines previously documented a role for PI3K-C2α in insulin-stimulated glucose uptake (falasca et al., 2007) and insulin secretion (Leibiger et al., 2010). Moreover, as liver act as a hub for glucose metabolism and homeostasis, we decided to examine the impact of *in vivo* PI3K-C2α inactivation on glucose homeostasis. Accordingly, starved and basal blood glucose (Figure 3a,b) as well as plasma insulin levels in KO mice were examined (Supplementary figure 3a). KO mice showed a gradual decrease in blood glucose levels. On the 4th day of tamoxifen treatment, blood glucose levels in KO mice corresponded to severe hypoglycaemia. Similar pattern of gradual hypoglycaemia was observed in *Pi3kc2a*$^{fl/fl}$*Cre*$^{-}$ mice treated with adeno-associated virus (AAV-TBG-iCre) (Figure 3c). Next, we examined the effect of glucose supplementation on the survival. Glucose treatment in the form of glucose gels, kept in the cages on the 4th day of tamoxifen treatment, prolonged the survival of KO mice. Subsequently, removal of these glucose gels subsequently lead to their demise after 3-4 days (figure 3d), proving critical role of PI3K-C2α in modulating glucose homeostasis. Apart from this, plasma insulin levels were significantly lowered in KO mice compared to WT controls. This was in line with involvement of PI3K-C2α in glucose stimulated insulin secretion as well as in insulin granule exocytosis (Dominguez et al., 2011; Leibiger et al., 2010). By definition, insulin hypersensitivity must be suspected in the presence of combined hypoglycaemia associated with low plasma insulin levels. Subsequently, glucose and insulin tolerance tests (GTT and ITT) were performed in order to determine response to glucose as well as to assess insulin sensitivity, respectively. Surprisingly, glucose clearance upon injection of glucose or insulin was not significantly affected in KO mice (Figure 3e,f). Similarly, phosphorylation of Akt in liver was similar between KO mice and WT mice upon injection of insulin at different time points (Supplementary figure 3b). Furthermore, given their role in regulating glucose uptake and hepatic glucose homeostasis, we decided to analyze the expression levels of key glucose transporter genes. However, we did not observe any significant differences in their expression levels in liver and muscles samples (Supplementary figure 3c). Overall, these results pointed out that, although loss of PI3K-C2α lead to severe hypoglycemia in KO mice, organismal glucose uptake and insulin signalling were not critically dependent on PI3K-C2α activity.

Knock-out of PI3K-C2α impairs endogenous glucose output and hepatic fatty acid β-oxidation

In case of starvation or hypoglycaemia, liver is responsible for generation of glucose either from non-carbohydrate sources such as proteins and lipids through the process of gluconeogenesis or from carbohydrate sources like glycogen through the process of glycogenolysis. Impairment in one of these pathways can lead to different metabolic disorders. We hypothesized that the hepatic lipid accumulation, if not caused due to defective glucose uptake or insulin signaling, could be a consequence of defects in endogenous glucose production pathways. In agreement, biochemical determination studies revealed elevated levels of glycogen deposits in KO liver samples compared to WT controls. (Figure 4a). Additionally, expression levels of pyruvate carboxylase (PC) and phosphoenolpyruvate kinase (PEPCK), key rate limiting enzymes involved in the metabolic pathway of gluconeogenesis, were significantly down-regulated in KO liver compared to respective controls (Figure 4b). Subsequently, we analyzed level of ketone bodies secreted by liver. Ketone bodies are produced and secreted by the liver as a result of intense gluconeogenesis. They are important source of energy for vital organs such as heart and brain in case of hypoglycaemia or starvation. We discovered that, compared to WT controls, KO mice secreted considerably lower amounts of ketone bodies from the liver (Figure 4c). Consistent with this data, KO liver displayed reduction in fatty acid β-oxidation rate, since Acetyl CoA, a precursor for ketone body production, is supplied through the process of fatty acid β-oxidation (Figure 4d). Accordingly, KO mice exhibited elevated levels of triglycerides and cholesterol esters in their liver (Figure 4e) as well as elevated serum triglycerides (Figure 4f). While, on the other hand, serum concentration of free fatty acids (FFA) and Low density lipoproteins (LDL) were significantly reduced in KO mice compared to WT controls (Figure 4g). This observed reduction in the rate of fatty acid β-oxidation was further supported by RT–PCR analysis showing down-regulation in the expression of key regulators of hepatic lipid metabolism; PPARα, HNF4α and their downstream effectors (Figure 4h). Hepatic lipid accumulation has been shown to induce endocrine changes that dysregulate adipose tissue lipolysis (Armstrong et al., 2014). In support of this view, we noticed enhanced tissue weights of inguinal white adipose tissue (iWAT) and epididymal white adipose tissue (eWAT) in KO mice compared to WT controls (Figure 4i). Apart from this, we did not observe any significant changes in expression levels of genes involved in fatty acid transport (Supplementary figure 4a) and *de novo* lipogenesis (Supplementary figure 4b). Overall, this data suggested that homozygous inactivation of PI3K-C2α in KO mice liver resulted in hypoketotic

hypoglycemia due to defects in glycogenolysis, gluconeogenesis and mitochondrial fatty acid β-oxidation.

Discussion

Much progress has been made in understanding the signaling roles of the PI3K isoforms, but many questions on their physiological and pathological roles still remain, especially for class II PI3Ks. In the past few years, we have learned that the α isoform of class II PI3Ks is linked to a broad panel of cellular functions (Gulluni et al., 2019). Apart from this, various transgenic mouse models have provided great insights into the physiological functions of PI3K-C2α. However, the postnatal functions of PI3KC2α have so far been inferred only from mice with heterozygous loss or partial deletion of the protein. Homozygous inactivation of whole protein or its kinase dead mutant results in lethality around embryonic day 10.5-11.5, with multiple defects underlying this phenotype (Alliouachene et al., 2016; Franco et al., 2014b; Yoshioka et al., 2012). Overall, PI3KC2α is clearly essential for embryonic development in mice yet its postnatal physiological functions remain poorly understood. Therefore in this present study, in order to access the organismal role of PI3K-C2α in postnatal physiology, we targeted its expression in adult mice by introducing *loxp* sites around exon 3. Using this conditional knock-out strategy, systemic deletion of PI3KC2α was possible at any developmental stage of choice.

Our data reveals that systemic ablation of PI3KC2α in 6-8 weeks old KO mice impacted their survival. These mice exhibited hepatic damage due lipid droplet accumulation caused by lipotoxicity. This phenotype is analogous with the pathological condition of non-alcoholic fatty liver disease (NAFLD). The severity of fatty liver disease is directly related to classic components of the metabolic syndrome including central obesity, hyperinsulinemia, insulin resistance and hyperglycemia (Bedogni et al., 2005; Byrne and Targher, 2015; Geisler and Renquist, 2017). However, unlike NAFLD, our KO mice exhibited hypoinsulinemia and hypoglycemia despite normal body weight and food intake. Lower plasma insulin levels in KO mice was in line with critical role of PI3K-C2α in glucose mediated insulin secretion and insulin granules exocytosis (Dominguez et al., 2011; Leibiger et al., 2010). It could also be possible that lower serum insulin levels are the consequence of hypoglycemia due to insulin feedback mechanism. By definition, insulin hypersensitivity must be suspected in the presence of hypoglycemia associated with low plasma insulin levels (Templeman et al., 2017). On the contrary, our data shows that PI3K-C2α ablation does not affect insulin signaling in adult KO mice. Indeed, KO mice did not show any alterations in systemic glucose tolerance and insulin sensitivity. Similarly, phosphorylation of Akt in KO mice liver upon insulin stimulation remained unaffected. These findings are in sharp

contrast with the previous cell-based studies that reported a positive role for PI3K-C2α in insulin signaling and glucose uptake (Brown et al., 1999; Falasca et al., 2007). The reason for these functional divergence are not clear at the moment. Although it can be argued that data obtained in tissue culture cells does not translate to primary tissues. It is also possible that compensatory mechanism exerted by other isoforms of PI3Ks are at play. PI3K-C2β and PI3K-C2γ were shown to play a role in glucose metabolism and insulin signaling *in vivo* (Alliouachene et al., 2015; Braccini et al., 2015b). Moreover, the roles of the class I PI3Ks on metabolism and energy homeostasis have been well-documented (Foukas et al., 2006; Knight et al., 2006; Sopasakis et al., 2010). In humans, fibroblasts derived from patients with homozygous PI3KC2α deficiency display increased expression of PI3K-C2β (Tiosano et al., 2019); raising the possibility of observing comparable effects in mice. Nevertheless, a recent study involving kinase dead PI3K-C2α mice also reported no significant changes in insulin signaling and glucose tolerance. However, it is important to mention that, unlike our KO mice, these mice were heterozygous for kinase dead mutant allele, while still maintaining potential scaffolding functions of PI3K-C2α (Alliouachene et al., 2016).

Our findings also suggest that homozygous inactivation of PI3K-C2α is responsible for defects in endogenous glucose production as well as hepatic fatty acid β-oxidation. In case of starvation or hypoglycemia, liver supplies the body with energy by breaking down non-carbohydrate sources such as proteins and lipids through the process of gluconeogenesis or from carbohydrate sources like glycogen through the process of glycogenolysis (Geisler et al., 2016). We observed that KO mice exhibited elevated hepatic glycogen stores compared to WT mice, a phenotype similar to Fanconi–Bickel Syndrome (Sharari et al., 2020). This was quite unexpected as glycogen stores are rapidly utilized within 12 hours of starvation or in this case, hypoglycemia. Moreover, previous study involving a class II PI3K-deficient mice has reported otherwise (Braccini et al., 2015b). On the other hand, gluconeogenic genes displayed significant reduction in KO liver samples. This was accompanied by reduction in ketogenesis and hepatic fatty acid β-oxidation. This effect might seem in contrast with the fact that, in response to lipid accumulation, hepatic fatty acid β-oxidation prevents lipotoxicity and supports gluconeogenesis and ketogenesis (Männistö et al., 2015; Sunny et al., 2010). Mice that are unable to normally upregulate lipid oxidative genes exhibit severe hepatic steatosis and display hypoketotic hypoglycemia (Merritt et

al., 2020). Consistent with these observations, hepatic expression of peroxisome proliferator receptor alpha (PPARα) showed down-regulation in KO liver samples. Hepatic PPARα expression and transcriptional activity are induced by elevated hepatic fatty acid accumulation which, in turn, regulates expression of target genes involved in fatty acid catabolism and clearance (Nakajima et al., 2017; Wang et al., 2020). PPARα-mediated upregulation of lipid oxidative genes also encourages maximal hepatic glucose output during fasting, since acetyl-CoA serves as an ample source of carbons for oxidation in the TCA cycle, which allows for flux of gluconeogenic substrates toward gluconeogenesis and away from TCA cycle oxidation (González-Manchón et al., 1992). Accordingly, adult mice lacking PPARα ($PPAR\alpha^{-/-}$) bears a phenotype similar to what we observed in our KO mice. In line with this observation, PPARα expression is involved in increasing transcription of target genes involved in gluconeogenesis (phosphoenolpyruvate carboxykinase; PEPCK, glucose 6-phosphatase; G6Pase) (Contreras et al., 2015; Im et al., 2011) and ketogenesis (hydroxy-3-methyl glutaryl CoA synthase 2; HMGCS2)(Rodríguez et al., 1994). Furthermore, blunted G6Pase upregulation in fasted PPARα null mice directs glucose 6-phosphate toward glycogen synthesis rather than hepatic export (Bandsma et al., 2004), further explaining elevated glycogen storage in KO mice liver. Apart from this, we observed reduction in another key regulators of liver lipid metabolism; HNF4α (hepatic nuclear factor 4, α isotype). A recent study has described a functional link between a regulatory subunit of PI3K (PIK3R3) and hepatic lipid metabolism through PIK3R3–HNF4α–PPARα axis (Yang et al., 2018). On the other hand, down-regulation of genes involved in *de-novo* lipogenesis, sterol response element-binding protein 1c (SCREBP1c) and fatty acid synthase (FASN), was consistent with observed hypoinsulinemia and hypoglycemia in our KO mice; since insulin and glucose have critical roles in stimulation of SCREBP1c and its downstream effectors(Dif et al., 2006).

Several limitations of the present study needs to be addressed. The intracellular mechanism through which PI3K-C2α modulates endogenous glucose production and hepatic fatty acid β-oxidation is not clear at the moment. During hypoglycemia and starvation, hyperglycemic hormones such as glucagon, epinephrine and cortisol promote glycogenolysis and gluconeogenesis in liver as well as lipolysis in the adipose tissues. This leads to improved hepatic glucose production and its release into the bloodstream as well as increased free fatty acid release from the adipose tissues and its subsequent utilization in the production of ketone bodies in the liver, respectively. Although glucagon and pyruvate tolerance tests did not show any significant

differences between KO and WT (data not shown), future experiments are needed to be performed to decipher the role of these hormones and their respective signaling pathways in the contribution towards the observed phenotype in KO mice. Moreover, it is unclear if observed hypoglycemia in KO mice is the sole cause for their demise. It is also important to mention that, sudden death phenotype was also observed by two separate research groups using an identical transgenic cre mice for the generation of conditional KO line for their gene of interest (data not shown). There are previous reports suggesting common pitfalls of Cre-loxp system such as cre toxicity, cre mis-recombination and cre non-specificity (Qiu et al., 2011; Sandlesh et al., 2018; Schmidt-Supprian and Rajewsky, 2007). Additionally, another lab from university college of London working on conditional knock-out mice for PI3KC2α didn't observe any phenotype, thereby greatly contrasting our data (data not shown).

In summary, our studies describe the phenotypic characterization of the first mouse model with a conditional systemic deletion of PI3K-C2α and reveal a role for this isoform in organismal regulation of glucose homeostasis.

Figures

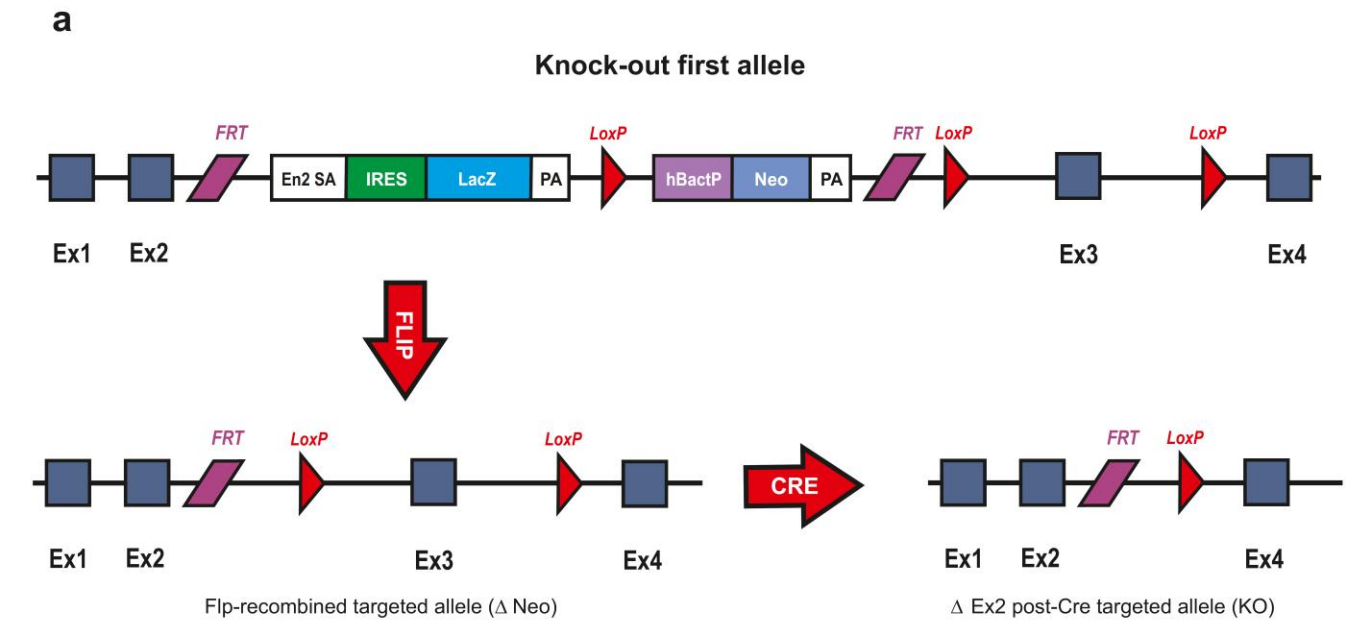
a
Knock-out first allele
FRT
LoxP
FRT
LoxP
LoxP
En2 SA
IRES
LacZ
PA
hBactP
Neo
PA
Ex1
Ex2
Ex3
Ex4
FLIP
FRT
LoxP
LoxP
CRE
FRT
LoxP
Ex1
Ex2
Ex3
Ex4
Ex1
Ex2
Ex4
Flp-recombined targeted allele (Δ Neo)
Δ Ex2 post-Cre targeted allele (KO)

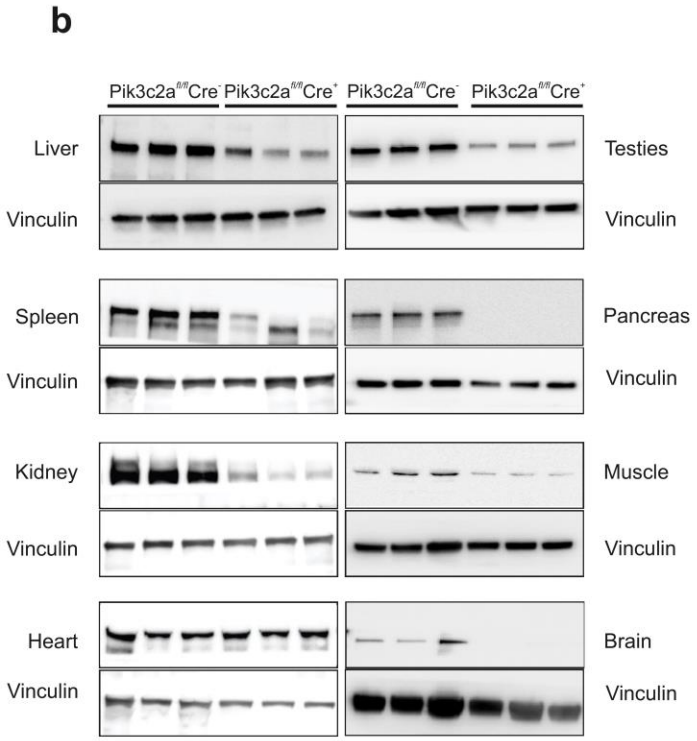
b
Pik3c2a fl/fl Cre- Pik3c2a fl/fl Cre+ Pik3c2a fl/fl Cre- Pik3c2a fl/fl Cre+
Liver
Vinculin
Testies
Vinculin
Spleen
Vinculin
Pancreas
Vinculin
Kidney
Vinculin
Muscle
Vinculin
Heart
Vinculin
Brain
Vinculin

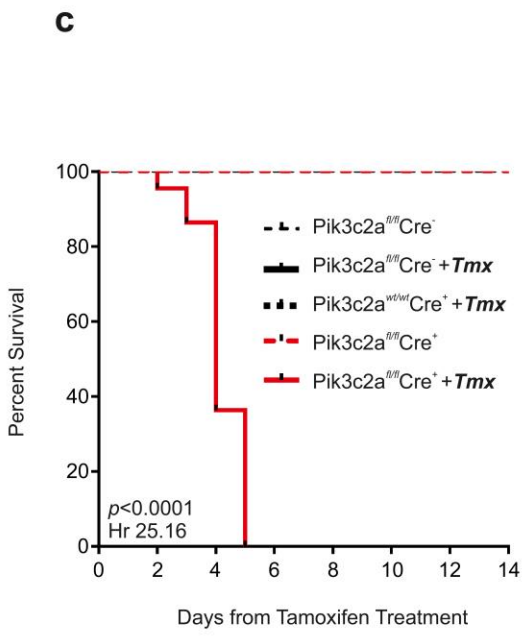
c
Percent Survival
100
80
60
40
20
0
p<0.0001
Hr 25.16
0
2
4
6
8
10
12
14
Days from Tamoxifen Treatment
Pik3c2a fl/fl Cre-
Pik3c2a fl/fl Cre- +Tmx
Pik3c2a wt/wt Cre+ +Tmx
Pik3c2a fl/fl Cre+
Pik3c2a fl/fl Cre+ +Tmx

Figure 1: Systemic deletion of PI3K-C2α strongly impairs the survival in Pi3kc2a$^{fl/fl}$Cre^{+} (KO) mice

a) Schematic diagram of gene targeting vector for generating the conditional knock-out mice for PI3K-C2α gene using Knock-out first strategy. The FRT flanked cassette encoding LacZ and Neomycin selection markers was first eliminated *in-vivo* by crossing into transgenic mice expressing FLP recombinase under beta-actin promoter. The resulting Pi3kc2a$^{fl/fl}$ mice were then crossed with Cre transgenic mice in order to generate *Pi3kc2a$^{fl/fl}$Cre^{+}* (KO) and *Pi3kc2a$^{fl/fl}$Cre^{-}* (WT) mice. En2 SA= En2 splice acceptor; IRES = internal ribosome entry site; hBactP =human beta actin promoter.

b) Western blot analysis of PI3K-C2α protein expression in different tissues isolated from KO and WT mice. Vinculin was used as a loading control. 60µg of protein was loaded per lane.

c) Kaplan–Meier survival curves of showing survival rates of *Pi3kc2a$^{fl/fl}$Cre^{+}*, *Pi3kc2a$^{wt/wt}$Cre^{+}* and *Pi3kc2a$^{fl/fl}$Cre^{-}* mice treated either with corn oil (n=6) or with tamoxifen (80 mg/kg/day, n=20) using oral gavage. KO mice were found dead or frail after 4-5 days of first tamoxifen treatment.

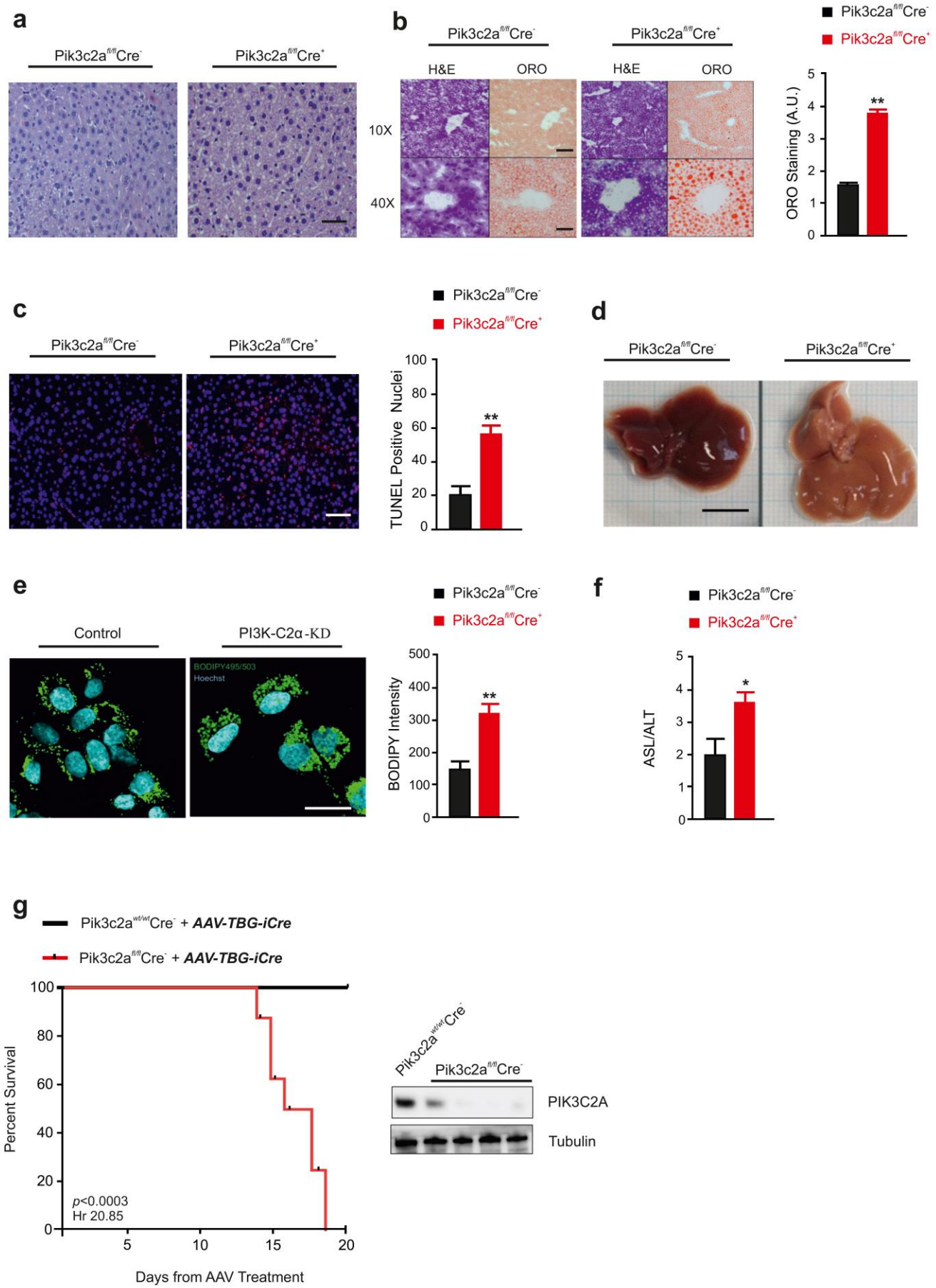
a
Pik3c2a^fl/fl Cre^-
Pik3c2a^fl/fl Cre^+
b
Pik3c2a^fl/fl Cre^-
Pik3c2a^fl/fl Cre^+
H&E
ORO
10X
40X
ORO Staining (A.U.)
**
c
TUNEL Positive Nuclei
**
d
e
Control
PI3K-C2α-KD
BODIPY495/503
Hoechst
BODIPY Intensity
**
f
ASL/ALT
*
g
Pik3c2a^wt/wt Cre^- + AAV-TBG-iCre
Pik3c2a^fl/fl Cre^- + AAV-TBG-iCre
Percent Survival
p<0.0003
Hr 20.85
Days from AAV Treatment
PIK3C2A
Tubulin

Figure 2: KO mice liver exhibits a phenotype similar to Non-alcoholic fatty liver disease

a) Representative images of Hematoxylin and Eosin (H&E) stained livers from WT and KO mice to visualize tissue morphology and steatosis. Scale bar=100µm (n=8)
b) Oil red O (ORO) staining to visualize lipid droplet accumulation in WT and KO livers (Magnification 10X, Scale bar=500 µm and 40X, Scale bar=100 µm). Quantification of the area of lipid droplet accumulation using Image J (n=6)
c) Terminal deoxynucleotidyl transferase-mediated nick end labelling (TUNEL) staining of the WT and steatotic liver. Average number of TUNEL positive cells were evaluated Scale bar=100 µm (n=8)
d) Macroscopic appearance of livers from WT and KO mice on 5^{th} day of tamoxifen treatment. Scale bar= 1cm
e) Lipid staining of HepG2 cells treated either with scrambled control or with PI3K-C2α siRNA. Subsequently, these cells were treated with 0.5 mM concentration of oleic acid for 12 hrs after which they were fixed and stained with BODIPY 493/503 (green), Hoechst (Cyan) dyes. Fluorescence images were captured using Leica SP8 microscope. Scale bar=5 µm (n=3)
f) Serum Alanine Transaminase (ALT) and Aspartate transaminase (AST) levels were measured and plotted as a ratio to evaluate the liver injury in WT and KO mice (n=8)
g) Kaplan–Meier survival curves of showing survival rates of $Pi3kc2a^{wt/wt}Cre^{-}$ and $Pi3kc2a^{fl/fl}Cre^{-}$ mice treated with adeno-associated virus (AAV) containing Cre recombinase under the liver specific human thyroid hormone-binding globulin (TBG) promoter (AAV-TBG-iCre) to induce the expression of Cre recombinase specific to hepatic tissue (n=8) . Western blot analysis showing PI3K-C2α protein expression of $Pi3kc2a^{wt/wt}Cre^{-}$ and $Pi3kc2a^{fl/fl}Cre^{-}$ liver lysates treated with liver specific adeno-associated virus.

   * $p< 0.05$, ** $p < 0.01$

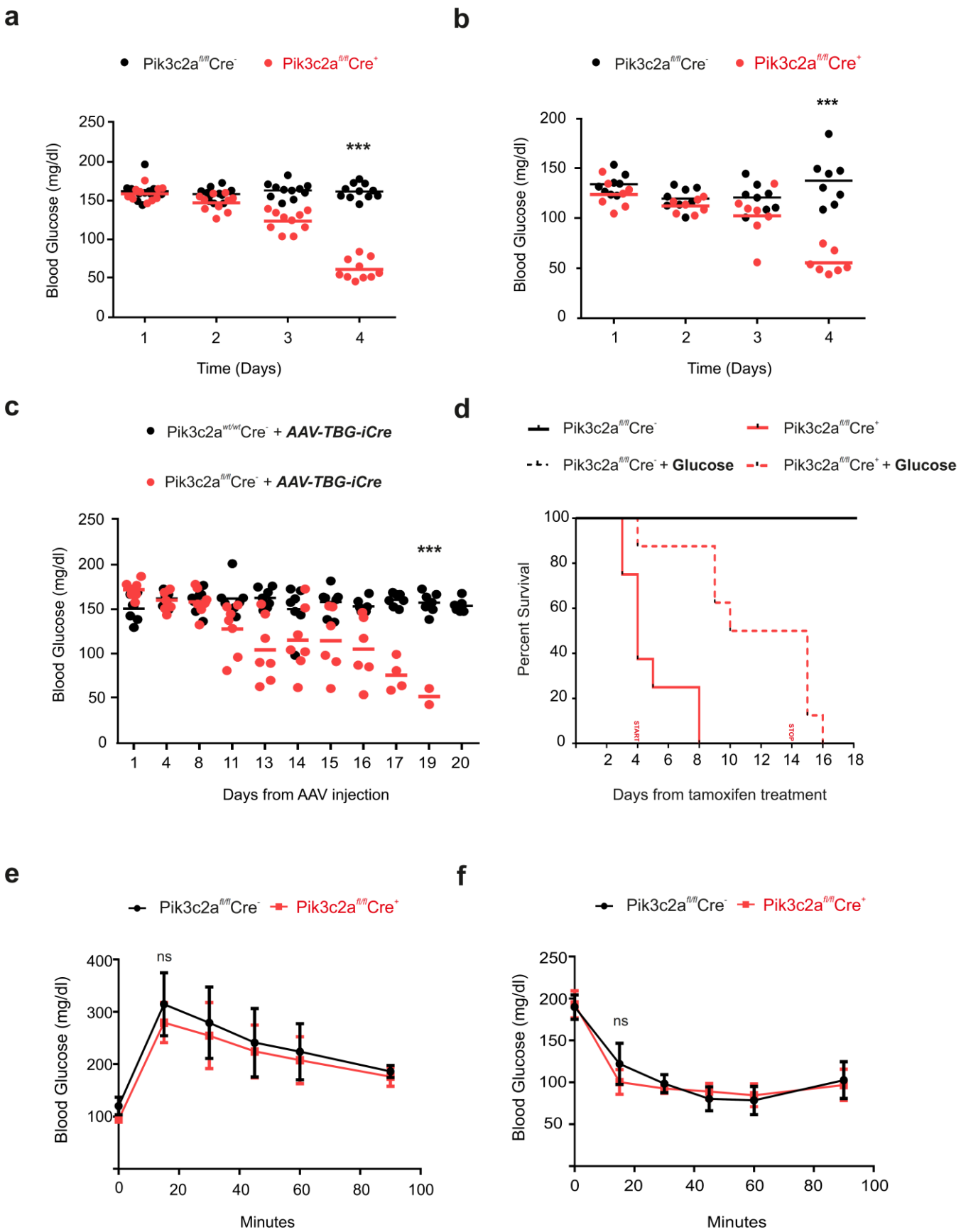
a
Pik3c2a^fl/fl Cre^-
Pik3c2a^fl/fl Cre^+
Blood Glucose (mg/dl)
Time (Days)
***
b
Pik3c2a^fl/fl Cre^-
Pik3c2a^fl/fl Cre^+
Blood Glucose (mg/dl)
Time (Days)
***
c
Pik3c2a^wt/wt Cre^- + AAV-TBG-iCre
Pik3c2a^fl/fl Cre^- + AAV-TBG-iCre
Blood Glucose (mg/dl)
Days from AAV injection
***
d
Pik3c2a^fl/fl Cre^-
Pik3c2a^fl/fl Cre^+
Pik3c2a^fl/fl Cre^- + Glucose
Pik3c2a^fl/fl Cre^+ + Glucose
Percent Survival
START
STOP
Days from tamoxifen treatment
e
Pik3c2a^fl/fl Cre^-
Pik3c2a^fl/fl Cre^+
Blood Glucose (mg/dl)
ns
Minutes
f
Pik3c2a^fl/fl Cre^-
Pik3c2a^fl/fl Cre^+
Blood Glucose (mg/dl)
ns
Minutes

Figure 3: PI3K-C2α inactivation results in severe hypoglycemia

a) Blood glucose levels in basal condition of WT and KO mice taken on consecutive days after the first tamoxifen treatment (n=10)
b) Blood glucose levels in starved condition of WT and KO mice taken on consecutive days after the first tamoxifen treatment (n=8)
c) Nonfasting blood glucose levels of *Pi3kc2a*$^{wt/wt}$*Cre*$^{-}$ and *Pi3kc2a*$^{fl/fl}$*Cre*$^{-}$ taken on consecutive days after the first intravenous injection of liver specific adeno-associated virus (AAV-TBG-iCre) (n=8).
d) Survival of WT and KO mice plotted as Kaplan–Meier curves suplemented with or without glucose gels (n=8).
e) Glucose tolerance test performed on day 3rd of tamoxifen treatment on WT and KO mice starved for 6hrs before injecting a glucose load of 2g/kg body weight intraperitoneally. Blood glucose levels were determined at different time points of 0, 15, 30, 45, 60, 90 mins (n=24)
f) Insulin tolerance test performed on day 3rd of tamoxifen treatment on WT and KO mice starved for 6hrs before injecting insulin dose of of 0.75U/kg body weight intraperitoneally. Blood glucose levels were determined at different time points of 0, 15, 30, 45, 60, 90 mins (n=24)

*** $p < 0.001$, ns= non-significant

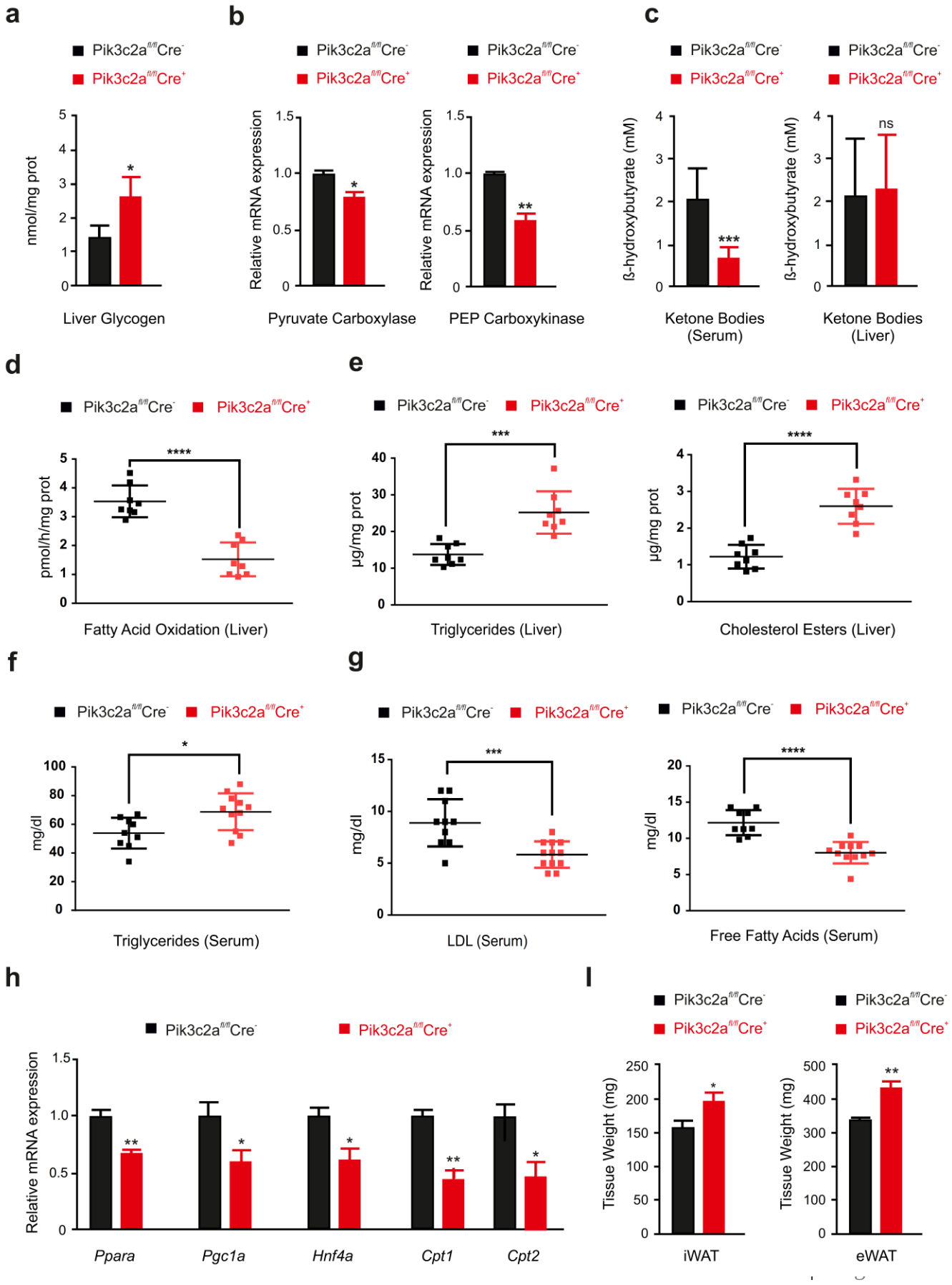
a
b
c
Pik3c2a fl/fl Cre-
Pik3c2a fl/fl Cre+
nmol/mg prot
Liver Glycogen
Relative mRNA expression
Pyruvate Carboxylase
PEP Carboxykinase
ß-hydroxybutyrate (mM)
Ketone Bodies (Serum)
Ketone Bodies (Liver)
ns
d
e
pmol/h/mg prot
Fatty Acid Oxidation (Liver)
µg/mg prot
Triglycerides (Liver)
Cholesterol Esters (Liver)
f
g
mg/dl
Triglycerides (Serum)
LDL (Serum)
Free Fatty Acids (Serum)
h
i
Ppara
Pgc1a
Hnf4a
Cpt1
Cpt2
Tissue Weight (mg)
iWAT
eWAT

Figure 4: Homozygous inactivation of PI3K-C2α impairs endogenous glucose output and hepatic fatty acid β-oxidation

a) Hepatic glycogen content determined by acid hydrolysis method in livers obtained from WT and KO mice (n=12)
b) Relative m-RNA expression of target genes involved in regulating rate-limiting step of gluconeogenesis measured via real time PCR in liver extracts of WT and KO mice (n=8)
c) Serum and liver content of total ketone bodies (β-hydroxybutyrate) determined with the help of colorimetric method. Serum was isolated from WT and KO mice using cardiac puncture on the 5^{th} day of tamoxifen treatment (n=18)
d) Hepatic fatty acid β-oxidation rate measured via colorimetric assay in liver extracts of WT and KO mice (n=8)
e) Hepatic lipid profile; Triglycerides (TG) and Cholesterol esters content measured spectrofluorimetrically in livers extracts of WT and KO mice (n=8)
f) Serum triglyceride content of WT and KO mice (n=10)
g) Serum Lipid profile; Free fatty acids (FFA), low-density lipoprotein (LDL) content in the serum collected using cardiac puncture (n=12)
h) Relative m-RNA expression of target genes involved in regulating hepatic fatty acid β-oxidation measured via real time PCR in liver extracts of WT and KO mice (n=14)
i) Tissue weights of inguinal white adipose tissue (iWAT) and epididymal white adipose tissue (eWAT) isolated from WT and KO mice (n=6)

* $p< 0.05$, ** $p < 0.01$, ***$p< 0.001$, ****$p< 0.0001$

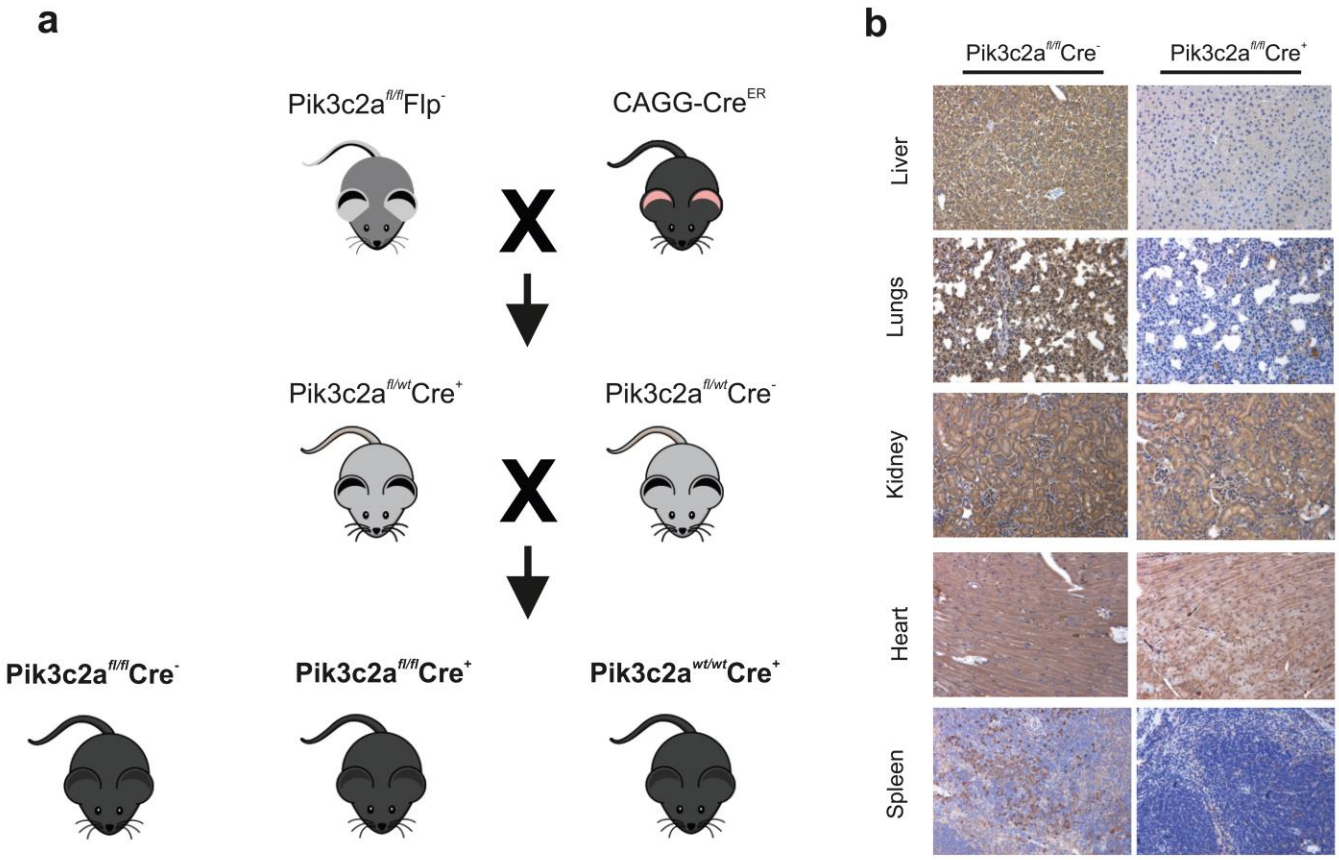
a
Pik3c2a fl/fl Flp-
CAGG-CreER
Pik3c2a fl/wt Cre+
Pik3c2a fl/wt Cre-
Pik3c2a fl/fl Cre-
Pik3c2a fl/fl Cre+
Pik3c2a wt/wt Cre+
b
Pik3c2a fl/fl Cre-
Pik3c2a fl/fl Cre+
Liver
Lungs
Kidney
Heart
Spleen

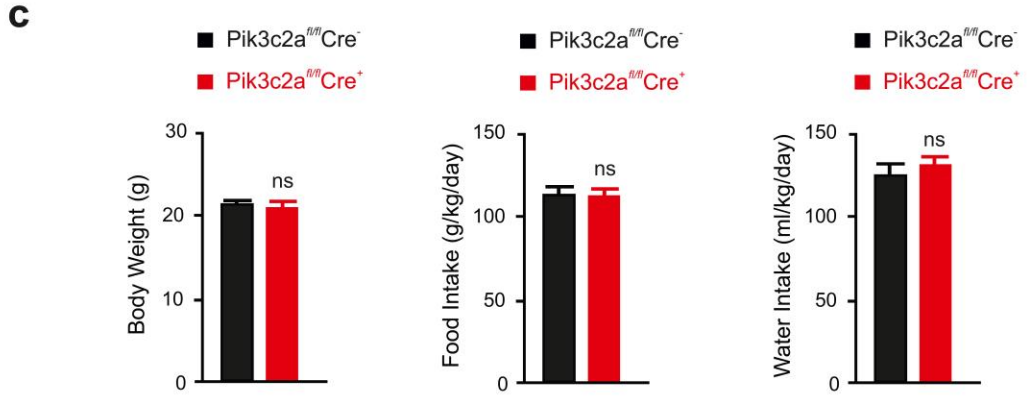
c
Pik3c2a fl/fl Cre-
Pik3c2a fl/fl Cre+
Body Weight (g)
30
20
10
0
ns
Food Intake (g/kg/day)
150
100
50
0
ns
Water Intake (ml/kg/day)
150
100
50
0
ns

Supplementary Figure 1: Generation of conditional Knock-out mice for PI3K-C2α

a) Schematic diagram of generating a conditional knock-out mice by breeding transgenic Cre mice (top right) with a mouse carrying homozygous floxed gene (exon 3 of PI3K-C2α) without the selection cassette (top left). A conditional Knock-out mice carrying a homozygous floxed gene and Cre (*Pi3kc2a*$^{fl/fl}$*Cre*$^{+}$, **KO***)* was obtained by crossing the F2 heterozygous progeny. *Pi3kc2a*$^{fl/fl}$*Cre*$^{-}$ (WT) and *Pi3kc2a*$^{wt/wt}$*Cre*$^{+}$ mice were obtained during the same cross used as experimental controls against KO mice.

b) Representative immunohistochemistry staining for PI3K-C2α in liver, Lung, Kidney, Heart and Spleen in WT and KO mice 4 days after the tamoxifen treatment. Magnification 10x, Scale bar=50µm.

c) Body weight, food intake and water intake from WT and KO mice after 4 days of tamoxifen treatment (n=6), ns= not significant

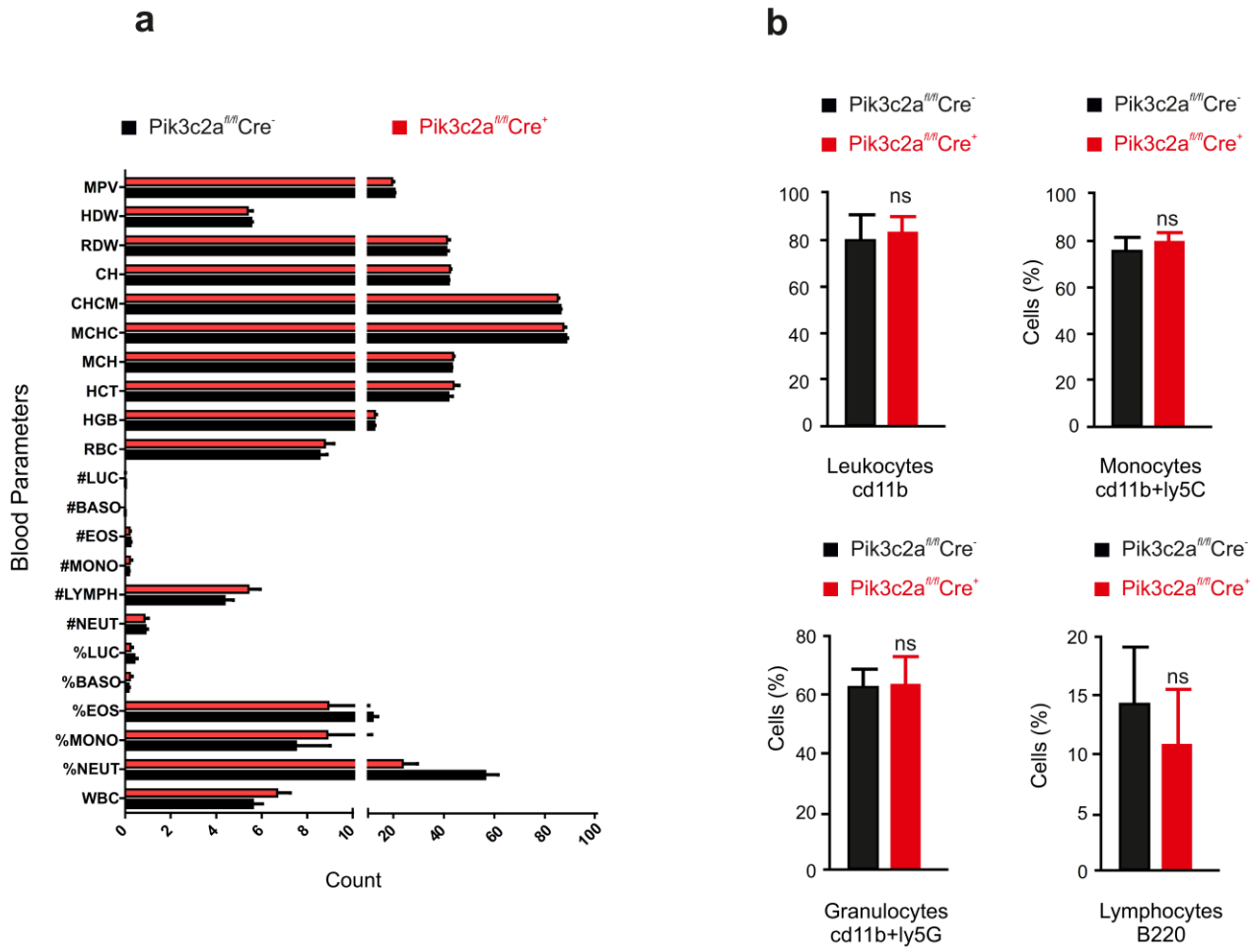
a
Pik3c2a fl/fl Cre-
Pik3c2a fl/fl Cre+
Blood Parameters
MPV
HDW
RDW
CH
CHCM
MCHC
MCH
HCT
HGB
RBC
#LUC
#BASO
#EOS
#MONO
#LYMPH
#NEUT
%LUC
%BASO
%EOS
%MONO
%NEUT
WBC
0 2 4 6 8 10 20 40 60 80 100
Count
b
Pik3c2a fl/fl Cre-
Pik3c2a fl/fl Cre+
ns
Cells (%)
Leukocytes cd11b
Monocytes cd11b+ly5C
Granulocytes cd11b+ly5G
Lymphocytes B220
c
Pik3c2a fl/fl Cre-
Pik3c2a fl/fl Cre+
A.U.
ns
EF
FS
LV Mass
LVOT CO
LVOT SV
RVOT CO
RVOT SV

Supplementary Figure 2: PI3K-C2α inactivation does not affect blood, cardiac and hematopoietic parameters

a) Blood parameters measured 4 days after the tamoxifen treatment. Blood was collected using cardiac puncture (n=8)
b) Flow symmetry analysis of hematopoietic parameters including Leukocytes, monocytes, Granulocytes and lymphocytes using appropriate antibodies. Bone marrow was isolated from mouse femur bone using a syringe. (n=6)
c) Echocardiographic measurements of cardiac parameters for anesthetized WT and KO mouse. Cardiac parameters analysed for ejection fraction (EF), fractional shortening (FS), left ventricle mass (LV mass), left ventricular outflow tract- cardiac output (LVOT CO), left ventricular outflow tract- stroke volume (LVOT SV), right ventricular outflow tract- cardiac output (RVOT CO), right ventricular outflow tract- stroke volume (RVOT SV) (n=8) ns= not significant

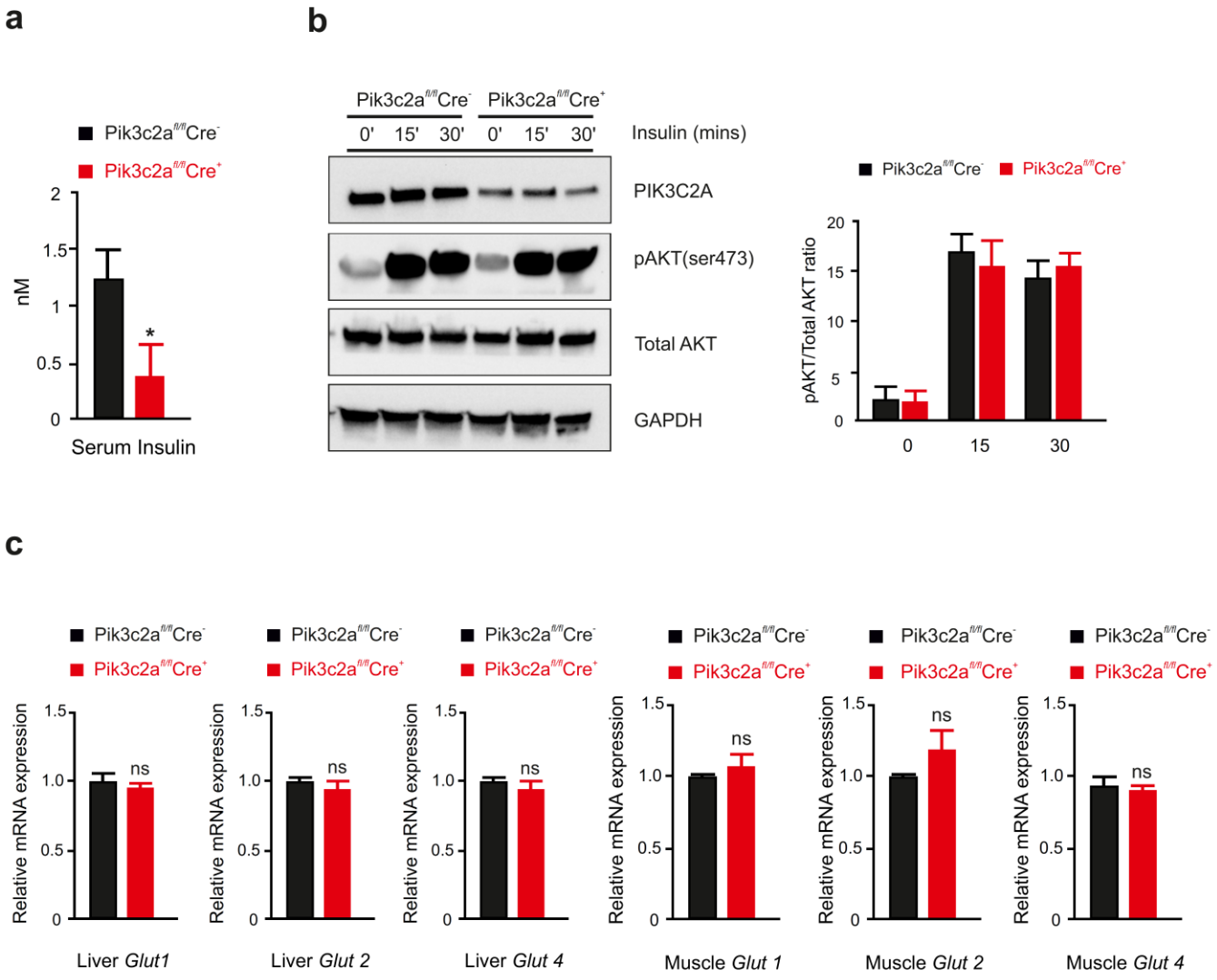
a
b
c
Pik3c2a fl/fl Cre-
Pik3c2a fl/fl Cre+
nM
Serum Insulin
0' 15' 30' 0' 15' 30'
Insulin (mins)
PIK3C2A
pAKT(ser473)
Total AKT
GAPDH
pAKT/Total AKT ratio
Relative mRNA expression
ns
Liver Glut1
Liver Glut 2
Liver Glut 4
Muscle Glut 1
Muscle Glut 2
Muscle Glut 4

Supplementary Figure 3: PI3K-C2α inactivation leads to hypoinsulinemia

a. Serum insulin levels determined with the help of colorimetric method. Serum was collected using cardiac puncture on the 5^{th} day of tamoxifen treatment (n=18)
b. Western blot analysis of Akt phosphorylation in liver extracts isolated from KO and WT mice. Mice were starved for 6 hours before injecting them with a 0.75U/kg dose of insulin intraperitoneally for 15 and 30 mins. GAPDH was used as a loading control. 60µg of protein was loaded per lane.
c. Relative m-RNA expression of glucose transporter genes involved facilitating glucose transport across plasma membrane measured via real time PCR in liver and muscle extracts of WT and KO mice (n=6) * $p < 0.05$, ns= not significant

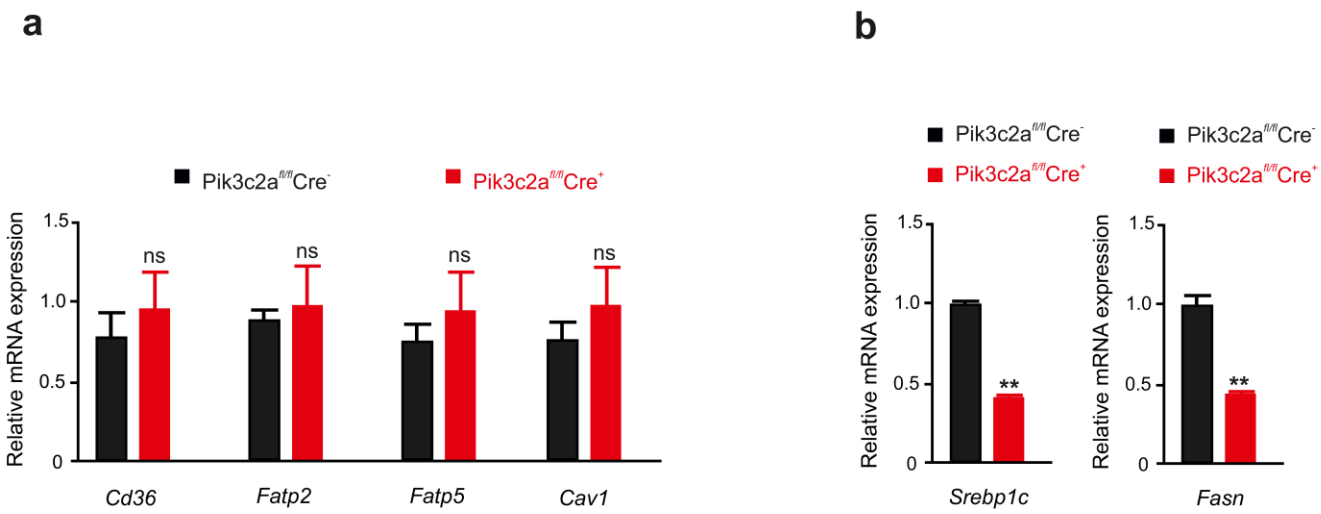
a
Pik3c2a^fl/fl Cre^-
Pik3c2a^fl/fl Cre^+
Relative mRNA expression
1.5
1.0
0.5
0
ns
ns
ns
ns
Cd36
Fatp2
Fatp5
Cav1
b
Pik3c2a^fl/fl Cre^-
Pik3c2a^fl/fl Cre^+
Pik3c2a^fl/fl Cre^-
Pik3c2a^fl/fl Cre^+
Relative mRNA expression
1.5
1.0
0.5
0
**
**
Srebp1c
Fasn

Supplemetary figure 4: Homozygous inactivation of Pi3kc2a does not affect de-novo lipogenesis and fatty acid uptake

a. Relative m-RNA expression of target genes involved in fatty acid uptake measured via real time PCR in liver extracts of WT and KO mice (n=6)
b. Relative m-RNA expression of target genes involved in *de-novo* lipogenesis measured via real time PCR in liver extracts of WT and KO mice (n=6)

   ** $p < 0.01$, ns= not significant

References

Alliouachene, S., Bilanges, B., Chaussade, C., Pearce, W., Foukas, L.C., Scudamore, C.L., Moniz, L.S., and Vanhaesebroeck, B. (2016). Inactivation of class II PI3K-C2α induces leptin resistance, age-dependent insulin resistance and obesity in male mice. Diabetologia *59*, 1503-1512.

Alliouachene, S., Bilanges, B., Chicanne, G., Anderson, K.E., Pearce, W., Ali, K., Valet, C., Posor, Y., Low, P.C., Chaussade, C., *et al.* (2015). Inactivation of the Class II PI3K-C2β Potentiates Insulin Signaling and Sensitivity. Cell reports *13*, 1881-1894.

Armstrong, M.J., Hazlehurst, J.M., Hull, D., Guo, K., Borrows, S., Yu, J., Gough, S.C., Newsome, P.N., and Tomlinson, J.W. (2014). Abdominal subcutaneous adipose tissue insulin resistance and lipolysis in patients with non-alcoholic steatohepatitis. Diabetes, Obesity and Metabolism *16*, 651-660.

Backer, J.M. (2008). The regulation and function of Class III PI3Ks: novel roles for Vps34. Biochem J *410*, 1-17.

Balla, T. (2013). Phosphoinositides: tiny lipids with giant impact on cell regulation. Physiol Rev *93*, 1019-1137.

Bandsma, R.H.J., Van Dijk, T.H., Harmsel At, A.t., Kok, T., Reijngoud, D.-J., Staels, B., and Kuipers, F. (2004). Hepatic de novo synthesis of glucose 6-phosphate is not affected in peroxisome proliferator-activated receptor alpha-deficient mice but is preferentially directed toward hepatic glycogen stores after a short term fast. The Journal of biological chemistry *279*, 8930-8937.

Bedogni, G., Miglioli, L., Masutti, F., Tiribelli, C., Marchesini, G., and Bellentani, S. (2005). Prevalence of and risk factors for nonalcoholic fatty liver disease: the Dionysos nutrition and liver study. Hepatology (Baltimore, Md) *42*, 44-52.

Bhattacharya, S., McElhanon, K.E., Gushchina, L.V., and Weisleder, N. (2016). Role of phosphatidylinositol-4,5-bisphosphate 3-kinase signaling in vesicular trafficking. Life sciences *167*, 39-45.

Bilanges, B., and Posor, Y. (2019). PI3K isoforms in cell signalling and vesicle trafficking. *20*, 515-534.

Braccini, L., Ciraolo, E., Campa, C.C., Perino, A., Longo, D.L., Tibolla, G., Pregnolato, M., Cao, Y., Tassone, B., Damilano, F., *et al.* (2015a). PI3K-C2gamma is a Rab5 effector selectively controlling endosomal Akt2 activation downstream of insulin signalling. Nat Commun *6*, 7400.

Braccini, L., Ciraolo, E., Campa, C.C., Perino, A., Longo, D.L., Tibolla, G., Pregnolato, M., Cao, Y., Tassone, B., Damilano, F., *et al.* (2015b). PI3K-C2gamma is a Rab5 effector selectively controlling endosomal Akt2 activation downstream of insulin signalling. *6*, 7400.

Broussard, J.A., Rappaz, B., Webb, D.J., and Brown, C.M. (2013). Fluorescence resonance energy transfer microscopy as demonstrated by measuring the activation of the serine/threonine kinase Akt. Nat Protoc *8*, 265-281.

Brown, R.A., Domin, J., Arcaro, A., Waterfield, M.D., and Shepherd, P.R. (1999). Insulin activates the alpha isoform of class II phosphoinositide 3-kinase. The Journal of biological chemistry *274*, 14529-14532.

Buondonno, I., Gazzano, E., Jean, S.R., Audrito, V., Kopecka, J., Fanelli, M., Salaroglio, I.C., Costamagna, C., Roato, I., Mungo, E., *et al.* (2016). Mitochondria-Targeted Doxorubicin: A New Therapeutic Strategy against Doxorubicin-Resistant Osteosarcoma. Molecular Cancer Therapeutics *15*, 2640-2652.

Byrne, C.D., and Targher, G. (2015). NAFLD: A multisystem disease. Journal of Hepatology *62*, S47-S64.

Campa, C.C., Franco, I., and Hirsch, E. (2015). PI3K-C2alpha: One enzyme for two products coupling vesicle trafficking and signal transduction. FEBS Lett *589*, 1552-1558.

Campa, C.C., and Hirsch, E. (2017). Rab11 and phosphoinositides: A synergy of signal transducers in the control of vesicular trafficking. Adv Biol Regul *63*, 132-139.

Cao, C., Backer, J.M., Laporte, J., Bedrick, E.J., and Wandinger-Ness, A. (2008). Sequential actions of myotubularin lipid phosphatases regulate endosomal PI(3)P and growth factor receptor trafficking. Mol Biol Cell *19*, 3334-3346.

Cao, C., Laporte, J., Backer, J.M., Wandinger-Ness, A., and Stein, M.P. (2007). Myotubularin lipid phosphatase binds the hVPS15/hVPS34 lipid kinase complex on endosomes. Traffic *8*, 1052-1067.

Chen, W., Feng, Y., Chen, D., and Wandinger-Ness, A. (1998). Rab11 is required for trans-golgi network-to-plasma membrane transport and a preferential target for GDP dissociation inhibitor. Mol Biol Cell *9*, 3241-3257.

Chenouard, N., Bloch, I., and Olivo-Marin, J.C. (2013). Multiple Hypothesis Tracking for Cluttered Biological Image Sequences. IEEE transactions on pattern analysis and machine intelligence.

Contreras, A.V., Rangel-Escareño, C., Torres, N., Alemán-Escondrillas, G., Ortiz, V., Noriega, L.G., Torre-Villalvazo, I., Granados, O., Velázquez-Villegas, L.A., Tobon-Cornejo, S., *et al.* (2015). PPARα via HNF4α regulates the expression of genes encoding hepatic amino acid catabolizing enzymes to maintain metabolic homeostasis. Genes & Nutrition *10*, 3.

Cullen, P.J. (2008). Endosomal sorting and signalling: an emerging role for sorting nexins. Nat Rev Mol Cell Biol *9*, 574-582.

de Chaumont, F., Dallongeville, S., Chenouard, N., Herve, N., Pop, S., Provoost, T., Meas-Yedid, V., Pankajakshan, P., Lecomte, T., Le Montagner, Y., *et al.* (2012). Icy: an open bioimage informatics platform for extended reproducible research. Nature methods *9*, 690-696.

Delevoye, C., Miserey-Lenkei, S., Montagnac, G., Gilles-Marsens, F., Paul-Gilloteaux, P., Giordano, F., Waharte, F., Marks, M.S., Goud, B., and Raposo, G. (2014). Recycling endosome tubule morphogenesis from sorting endosomes requires the kinesin motor KIF13A. Cell Rep *6*, 445-454.

Devereaux, K., Dall'Armi, C., Alcazar-Roman, A., Ogasawara, Y., Zhou, X., Wang, F., Yamamoto, A., De Camilli, P., and Di Paolo, G. (2013). Regulation of mammalian autophagy by class II and III PI 3-kinases through PI3P synthesis. PloS one *8*, e76405.

Dif, N., Euthine, V., Gonnet, E., Laville, M., Vidal, H., and Lefai, E. (2006). Insulin activates human sterol-regulatory-element-binding protein-1c (SREBP-1c) promoter through SRE motifs. The Biochemical journal *400*, 179-188.

DiPilato, L.M., and Zhang, J. (2009). The role of membrane microdomains in shaping beta2-adrenergic receptor-mediated cAMP dynamics. Molecular bioSystems *5*, 832-837.

Dominguez, V., Raimondi, C., Somanath, S., Bugliani, M., Loder, M.K., Edling, C.E., Divecha, N., da Silva-Xavier, G., Marselli, L., Persaud, S.J., *et al.* (2011). Class II phosphoinositide 3-kinase regulates exocytosis of insulin granules in pancreatic beta cells. The Journal of biological chemistry *286*, 4216-4225.

Eathiraj, S., Mishra, A., Prekeris, R., and Lambright, D.G. (2006). Structural basis for Rab11-mediated recruitment of FIP3 to recycling endosomes. J Mol Biol *364*, 121-135.

El Sheikh, S.S., Domin, J., Tomtitchong, P., Abel, P., Stamp, G., and Lalani, E.-N. (2003). Topographical expression of class IA and class II phosphoinositide 3-kinase enzymes in normal human tissues is consistent with a role in differentiation. BMC Clin Pathol *3*, 4-4.

Falasca, M., Hughes, W.E., Dominguez, V., Sala, G., Fostira, F., Fang, M.Q., Cazzolli, R., Shepherd, P.R., James, D.E., and Maffucci, T. (2007). The role of phosphoinositide 3-kinase C2alpha in insulin signaling. The Journal of biological chemistry *282*, 28226-28236.

Falasca, M., and Maffucci, T. (2012). Regulation and cellular functions of class II phosphoinositide 3-kinases. Biochem J *443*, 587-601.

Firestone, A.J., Weinger, J.S., Maldonado, M., Barlan, K., Langston, L.D., O'Donnell, M., Gelfand, V.I., Kapoor, T.M., and Chen, J.K. (2012). Small-molecule inhibitors of the AAA+ ATPase motor cytoplasmic dynein. Nature *484*, 125-129.

Foukas, L.C., Claret, M., Pearce, W., Okkenhaug, K., Meek, S., Peskett, E., Sancho, S., Smith, A.J.H., Withers, D.J., and Vanhaesebroeck, B. (2006). Critical role for the p110α phosphoinositide-3-OH kinase in growth and metabolic regulation. Nature *441*, 366-370.

Franco, I., Gulluni, F., Campa, C.C., Costa, C., Margaria, J.P., Ciraolo, E., Martini, M., Monteyne, D., De Luca, E., Germena, G., *et al.* (2014a). PI3K class II alpha controls spatially restricted

endosomal PtdIns3P and Rab11 activation to promote primary cilium function. Dev Cell *28*, 647-658.

Franco, I., Gulluni, F., Campa, C.C., Costa, C., Margaria, J.P., Ciraolo, E., Martini, M., Monteyne, D., De Luca, E., Germena, G., *et al.* (2014b). PI3K class II α controls spatially restricted endosomal PtdIns3P and Rab11 activation to promote primary cilium function. Developmental cell *28*, 647-658.

Franco, I., Margaria, J.P., De Santis, M.C., Ranghino, A., Monteyne, D., Chiaravalli, M., Pema, M., Campa, C.C., Ratto, E., Gulluni, F., *et al.* (2016). Phosphoinositide 3-Kinase-C2alpha Regulates Polycystin-2 Ciliary Entry and Protects against Kidney Cyst Formation. J Am Soc Nephrol *27*, 1135-1144.

Fruman, D.A., Chiu, H., Hopkins, B.D., Bagrodia, S., Cantley, L.C., and Abraham, R.T. (2017). The PI3K Pathway in Human Disease. Cell *170*, 605-635.

Gaidarov, I., Smith, M.E., Domin, J., and Keen, J.H. (2001). The class II phosphoinositide 3-kinase C2alpha is activated by clathrin and regulates clathrin-mediated membrane trafficking. Mol Cell *7*, 443-449.

Gaidarov, I., Zhao, Y., and Keen, J.H. (2005). Individual phosphoinositide 3-kinase C2alpha domain activities independently regulate clathrin function. The Journal of biological chemistry *280*, 40766-40772.

Gallo, L.I., Liao, Y., Ruiz, W.G., Clayton, D.R., Li, M., Liu, Y.J., Jiang, Y., Fukuda, M., Apodaca, G., and Yin, X.M. (2014). TBC1D9B functions as a GTPase-activating protein for Rab11a in polarized MDCK cells. Mol Biol Cell *25*, 3779-3797.

Geisler, C.E., Hepler, C., Higgins, M.R., and Renquist, B.J. (2016). Hepatic adaptations to maintain metabolic homeostasis in response to fasting and refeeding in mice. Nutr Metab (Lond) *13*, 62-62.

Geisler, C.E., and Renquist, B.J. (2017). Hepatic lipid accumulation: cause and consequence of dysregulated glucoregulatory hormones. The Journal of endocrinology *234*, R1-r21.

González-Manchón, C., Martín-Requero, A., Ayuso, M.S., and Parrilla, R. (1992). Role of endogenous fatty acids in the control of hepatic gluconeogenesis. Archives of Biochemistry and Biophysics *292*, 95-101.

Gulluni, F., De Santis, M.C., Margaria, J.P., Martini, M., and Hirsch, E. (2019). Class II PI3K Functions in Cell Biology and Disease. Trends Cell Biol *29*, 339-359.

Gulluni, F., Martini, M., De Santis, M.C., Campa, C.C., Ghigo, A., Margaria, J.P., Ciraolo, E., Franco, I., Ala, U., Annaratone, L., *et al.* (2017a). Mitotic Spindle Assembly and Genomic Stability in Breast Cancer Require PI3K-C2alpha Scaffolding Function. Cancer Cell *32*, 444-459 e447.

Gulluni, F., Martini, M., De Santis, M.C., Campa, C.C., Ghigo, A., Margaria, J.P., Ciraolo, E., Franco, I., Ala, U., Annaratone, L., *et al.* (2017b). Mitotic Spindle Assembly and Genomic Stability in Breast Cancer Require PI3K-C2alpha Scaffolding Function. Nature chemical biology *32*, 444-459.e447.

Harris, D.P., Vogel, P., Wims, M., Moberg, K., Humphries, J., Jhaver, K.G., DaCosta, C.M., Shadoan, M.K., Xu, N., Hansen, G.M., *et al.* (2011). Requirement for class II phosphoinositide 3-kinase C2alpha in maintenance of glomerular structure and function. Molecular and cellular biology *31*, 63-80.

Hnia, K., Vaccari, I., Bolino, A., and Laporte, J. (2012). Myotubularin phosphoinositide phosphatases: cellular functions and disease pathophysiology. Trends Mol Med *18*, 317-327.
Hoepfner, S., Severin, F., Cabezas, A., Habermann, B., Runge, A., Gillooly, D., Stenmark, H., and Zerial, M. (2005). Modulation of receptor recycling and degradation by the endosomal kinesin KIF16B. Cell *121*, 437-450.

Horgan, C.P., Hanscom, S.R., Jolly, R.S., Futter, C.E., and McCaffrey, M.W. (2010a). Rab11-FIP3 binds dynein light intermediate chain 2 and its overexpression fragments the Golgi complex. Biochem Biophys Res Commun *394*, 387-392.

Horgan, C.P., Hanscom, S.R., Jolly, R.S., Futter, C.E., and McCaffrey, M.W. (2010b). Rab11-FIP3 links the Rab11 GTPase and cytoplasmic dynein to mediate transport to the endosomal-recycling compartment. J Cell Sci *123*, 181-191.

Im, S.S., Kim, M.Y., Kwon, S.K., Kim, T.H., Bae, J.S., Kim, H., Kim, K.S., Oh, G.T., and Ahn, Y.H. (2011). Peroxisome proliferator-activated receptor {alpha} is responsible for the up-regulation of hepatic glucose-6-phosphatase gene expression in fasting and db/db Mice. The Journal of biological chemistry *286*, 1157-1164.

Jares-Erijman, E.A., and Jovin, T.M. (2003). FRET imaging. Nat Biotechnol *21*, 1387-1395.
Jean, S., Cox, S., Schmidt, E.J., Robinson, F.L., and Kiger, A. (2012). Sbf/MTMR13 coordinates PI(3)P and Rab21 regulation in endocytic control of cellular remodeling. Mol Biol Cell *23*, 2723-2740.

Jean, S., and Kiger, A.A. (2014). Classes of phosphoinositide 3-kinases at a glance. J Cell Sci *127*, 923-928.

Jovic, M., Kean, M.J., Dubankova, A., Boura, E., Gingras, A.C., Brill, J.A., and Balla, T. (2014). Endosomal sorting of VAMP3 is regulated by PI4K2A. J Cell Sci *127*, 3745-3756.

Jovic, M., Sharma, M., Rahajeng, J., and Caplan, S. (2010). The early endosome: a busy sorting station for proteins at the crossroads. Histol Histopathol *25*, 99-112.

Kardash, E., Bandemer, J., and Raz, E. (2011). Imaging protein activity in live embryos using fluorescence resonance energy transfer biosensors. Nat Protoc *6*, 1835-1846.

Ketel, K., Krauss, M., Nicot, A.S., Puchkov, D., Wieffer, M., Muller, R., Subramanian, D., Schultz, C., Laporte, J., and Haucke, V. (2016). A phosphoinositide conversion mechanism for exit from endosomes. Nature *529*, 408-412.

Knight, Z.A., Gonzalez, B., Feldman, M.E., Zunder, E.R., Goldenberg, D.D., Williams, O., Loewith, R., Stokoe, D., Balla, A., Toth, B., *et al.* (2006). A pharmacological map of the PI3-K family defines a role for p110alpha in insulin signaling. Cell *125*, 733-747.

Leibiger, B., Moede, T., Paschen, M., Yunn, N.O., Lim, J.H., Ryu, S.H., Pereira, T., Berggren, P.O., and Leibiger, I.B. (2015). PI3K-C2α Knockdown Results in Rerouting of Insulin Signaling and Pancreatic Beta Cell Proliferation. Cell Rep *13*, 15-22.

Leibiger, B., Moede, T., Uhles, S., Barker, C.J., Creveaux, M., Domin, J., Berggren, P.O., and Leibiger, I.B. (2010). Insulin-feedback via PI3K-C2alpha activated PKBalpha/Akt1 is required for glucose-stimulated insulin secretion. FASEB journal : official publication of the Federation of American Societies for Experimental Biology *24*, 1824-1837.

Lu, Q., Insinna, C., Ott, C., Stauffer, J., Pintado, P.A., Rahajeng, J., Baxa, U., Walia, V., Cuenca, A., Hwang, Y.S., *et al.* (2015). Early steps in primary cilium assembly require EHD1/EHD3-dependent ciliary vesicle formation. Nat Cell Biol *17*, 531.

Männistö, V.T., Simonen, M., Hyysalo, J., Soininen, P., Kangas, A.J., Kaminska, D., Matte, A.K., Venesmaa, S., Käkelä, P., Kärjä, V., *et al.* (2015). Ketone body production is differentially altered in steatosis and non-alcoholic steatohepatitis in obese humans. Liver international : official journal of the International Association for the Study of the Liver *35*, 1853-1861.

Marat, A.L., and Haucke, V. (2016). Phosphatidylinositol 3-phosphates-at the interface between cell signalling and membrane traffic. EMBO J *35*, 561-579.

Maxfield, F.R., and McGraw, T.E. (2004). Endocytic recycling. Nat Rev Mol Cell Biol *5*, 121-132.

Mazza, S., and Maffucci, T. (2011). Class II phosphoinositide 3-kinase C2alpha: what we learned so far. Int J Biochem Mol Biol *2*, 168-182.

Mellman, I., and Nelson, W.J. (2008). Coordinated protein sorting, targeting and distribution in polarized cells. Nat Rev Mol Cell Biol *9*, 833-845.

Merrill, N.M., Schipper, J.L., Karnes, J.B., Kauffman, A.L., Martin, K.R., and MacKeigan, J.P. (2017). PI3K-C2alpha knockdown decreases autophagy and maturation of endocytic vesicles. PloS one *12*, e0184909.

Merritt, J.L., MacLeod, E., Jurecka, A., and Hainline, B. (2020). Clinical manifestations and management of fatty acid oxidation disorders. Reviews in Endocrine and Metabolic Disorders.

Meunier, F.A., Osborne, S.L., Hammond, G.R., Cooke, F.T., Parker, P.J., Domin, J., and Schiavo, G. (2005). Phosphatidylinositol 3-kinase C2alpha is essential for ATP-dependent priming of neurosecretory granule exocytosis. Mol Biol Cell *16*, 4841-4851.

Miyawaki, A., and Tsien, R.Y. (2000). Monitoring protein conformations and interactions by fluorescence resonance energy transfer between mutants of green fluorescent protein. Methods in enzymology *327*, 472-500.

Mountford, J.K., Petitjean, C., Putra, H.W., McCafferty, J.A., Setiabakti, N.M., Lee, H., Tønnesen, L.L., McFadyen, J.D., Schoenwaelder, S.M., Eckly, A., *et al.* (2015). The class II PI 3-kinase, PI3KC2α, links platelet internal membrane structure to shear-dependent adhesive function. Nat Commun *6*, 6535.

Nakajima, T., Yang, Y., Lu, Y., Kamijo, Y., Yamada, Y., Nakamura, K., Koyama, M., Yamaguchi, S., Sugiyama, E., Tanaka, N., *et al.* (2017). Decreased Fatty Acid β-Oxidation Is the Main Cause of Fatty Liver Induced by Polyunsaturated Fatty Acid Deficiency in Mice. The Tohoku journal of experimental medicine *242*, 229-239.

Nigorikawa, K., Hazeki, K., Guo, Y., and Hazeki, O. (2014). Involvement of class II phosphoinositide 3-kinase alpha-isoform in antigen-induced degranulation in RBL-2H3 cells. PloS one *9*, e111698.

Pertz, O., Hodgson, L., Klemke, R.L., and Hahn, K.M. (2006). Spatiotemporal dynamics of RhoA activity in migrating cells. Nature *440*, 1069-1072.

Posor, Y., Eichhorn-Gruenig, M., Puchkov, D., Schoneberg, J., Ullrich, A., Lampe, A., Muller, R., Zarbakhsh, S., Gulluni, F., Hirsch, E., *et al.* (2013). Spatiotemporal control of endocytosis by phosphatidylinositol-3,4-bisphosphate. Nature *499*, 233-237.

Qiu, L., Rivera-Pérez, J.A., and Xu, Z. (2011). A Non-Specific Effect Associated with Conditional Transgene Expression Based on Cre-loxP Strategy in Mice. PloS one *6*, e18778.

Ren, M., Xu, G., Zeng, J., De Lemos-Chiarandini, C., Adesnik, M., and Sabatini, D.D. (1998). Hydrolysis of GTP on rab11 is required for the direct delivery of transferrin from the pericentriolar recycling compartment to the cell surface but not from sorting endosomes. Proc Natl Acad Sci U S A *95*, 6187-6192.

Rodríguez, J.C., Gil-Gómez, G., Hegardt, F.G., and Haro, D. (1994). Peroxisome proliferator-activated receptor mediates induction of the mitochondrial 3-hydroxy-3-methylglutaryl-CoA synthase gene by fatty acids. The Journal of biological chemistry *269*, 18767-18772.

Sakaguchi, A., Sato, M., Sato, K., Gengyo-Ando, K., Yorimitsu, T., Nakai, J., and Hara, T. (2015). REI-1 Is a Guanine Nucleotide Exchange Factor Regulating RAB-11 Localization and Function in C. elegans Embryos. Dev Cell *35*, 211-221.

Sandlesh, P., Juang, T., Safina, A., Higgins, M.J., and Gurova, K.V. (2018). Uncovering the fine print of the CreERT2-LoxP system while generating a conditional knockout mouse model of Ssrp1 gene. PloS one *13*, e0199785.

Schink, K.O., Raiborg, C., and Stenmark, H. (2013). Phosphatidylinositol 3-phosphate, a lipid that regulates membrane dynamics, protein sorting and cell signalling. BioEssays : news and reviews in molecular, cellular and developmental biology *35*, 900-912.

Schink, K.O., Tan, K.W., and Stenmark, H. (2016). Phosphoinositides in Control of Membrane Dynamics. Annual review of cell and developmental biology *32*, 143-171.

Schmidt-Supprian, M., and Rajewsky, K. (2007). Vagaries of conditional gene targeting. Nature Immunology *8*, 665-668.

Sharari, S., Abou-Alloul, M., Hussain, K., and Ahmad Khan, F. (2020). Fanconi–Bickel Syndrome: A Review of the Mechanisms That Lead to Dysglycaemia. International Journal of Molecular Sciences *21*, 6286.

Simonsen, A., Lippe, R., Christoforidis, S., Gaullier, J.M., Brech, A., Callaghan, J., Toh, B.H., Murphy, C., Zerial, M., and Stenmark, H. (1998). EEA1 links PI(3)K function to Rab5 regulation of endosome fusion. Nature *394*, 494-498.

Sonnichsen, B., De Renzis, S., Nielsen, E., Rietdorf, J., and Zerial, M. (2000). Distinct membrane domains on endosomes in the recycling pathway visualized by multicolor imaging of Rab4, Rab5, and Rab11. J Cell Biol *149*, 901-914.

Sopasakis, V.R., Liu, P., Suzuki, R., Kondo, T., Winnay, J., Tran, T.T., Asano, T., Smyth, G., Sajan, M.P., Farese, R.V., *et al.* (2010). Specific roles of the p110alpha isoform of phosphatidylinsositol 3-kinase in hepatic insulin signaling and metabolic regulation. Cell metabolism *11*, 220-230.

Sunny, N.E., Satapati, S., Fu, X., He, T., Mehdibeigi, R., Spring-Robinson, C., Duarte, J., Potthoff, M.J., Browning, J.D., and Burgess, S.C. (2010). Progressive adaptation of hepatic ketogenesis in mice fed a high-fat diet. American Journal of Physiology-Endocrinology and Metabolism *298*, E1226-E1235.

Takahashi, S., Kubo, K., Waguri, S., Yabashi, A., Shin, H.W., Katoh, Y., and Nakayama, K. (2012). Rab11 regulates exocytosis of recycling vesicles at the plasma membrane. J Cell Sci *125*, 4049-4057.

Templeman, N.M., Flibotte, S., Chik, J.H.L., Sinha, S., Lim, G.E., Foster, L.J., Nislow, C., and Johnson, J.D. (2017). Reduced Circulating Insulin Enhances Insulin Sensitivity in Old Mice and Extends Lifespan. Cell reports *20*, 451-463.

Tiosano, D., Baris, H.N., Chen, A., Hitzert, M.M., Schueler, M., Gulluni, F., Wiesener, A., Bergua, A., Mory, A., Copeland, B., *et al.* (2019). Mutations in PIK3C2A cause syndromic short stature,

skeletal abnormalities, and cataracts associated with ciliary dysfunction. PLOS Genetics *15*, e1008088.

Traer, C.J., Rutherford, A.C., Palmer, K.J., Wassmer, T., Oakley, J., Attar, N., Carlton, J.G., Kremerskothen, J., Stephens, D.J., and Cullen, P.J. (2007). SNX4 coordinates endosomal sorting of TfnR with dynein-mediated transport into the endocytic recycling compartment. Nat Cell Biol *9*, 1370-1380.

Ullrich, O., Reinsch, S., Urbe, S., Zerial, M., and Parton, R.G. (1996). Rab11 regulates recycling through the pericentriolar recycling endosome. J Cell Biol *135*, 913-924.

Ursø, B., Brown, R.A., O'Rahilly, S., Shepherd, P.R., and Siddle, K. (1999). The alpha-isoform of class II phosphoinositide 3-kinase is more effectively activated by insulin receptors than IGF receptors, and activation requires receptor NPEY motifs. FEBS Lett *460*, 423-426.

Vanhaesebroeck, B., Guillermet-Guibert, J., Graupera, M., and Bilanges, B. (2010). The emerging mechanisms of isoform-specific PI3K signalling. Nat Rev Mol Cell Biol *11*, 329-341.

Vanhaesebroeck, B., Whitehead, M.A., and Pineiro, R. (2016). Molecules in medicine mini-review: isoforms of PI3K in biology and disease. Journal of molecular medicine (Berlin, Germany) *94*, 5-11.

Velichkova, M., Juan, J., Kadandale, P., Jean, S., Ribeiro, I., Raman, V., Stefan, C., and Kiger, A.A. (2010a). Drosophila Mtm and class II PI3K coregulate a PI(3)P pool with cortical and endolysosomal functions. J Cell Biol *190*, 407-425.

Velichkova, M., Juan, J., Kadandale, P., Jean, S., Ribeiro, I., Raman, V., Stefan, C., and Kiger, A.A. (2010b). Drosophila Mtm and class II PI3K coregulate a PI(3)P pool with cortical and endolysosomal functions. J Cell Biol *190*, 407-425.

Wandinger-Ness, A., and Zerial, M. (2014). Rab proteins and the compartmentalization of the endosomal system. Cold Spring Harb Perspect Biol *6*, a022616.

Wang, Y., Nakajima, T., Gonzalez, F.J., and Tanaka, N. (2020). PPARs as Metabolic Regulators in the Liver: Lessons from Liver-Specific PPAR-Null Mice. International journal of molecular sciences *21*, 2061.

Welz, T., Wellbourne-Wood, J., and Kerkhoff, E. (2014). Orchestration of cell surface proteins by Rab11. Trends Cell Biol *24*, 407-415.

Whitlow, M., Bell, B.A., Feng, S.L., Filpula, D., Hardman, K.D., Hubert, S.L., Rollence, M.L., Wood, J.F., Schott, M.E., Milenic, D.E., *et al.* (1993). An improved linker for single-chain Fv with reduced aggregation and enhanced proteolytic stability. Protein Eng *6*, 989-995.

Winter, J.F., Hopfner, S., Korn, K., Farnung, B.O., Bradshaw, C.R., Marsico, G., Volkmer, M., Habermann, B., and Zerial, M. (2012). Caenorhabditis elegans screen reveals role of PAR-5 in RAB-11-recycling endosome positioning and apicobasal cell polarity. Nat Cell Biol *14*, 666-676.

Xu, X., Li, C., Garrett-Beal, L., Larson, D., Wynshaw-Boris, A., and Deng, C.X. (2001). Direct removal in the mouse of a floxed neo gene from a three-loxP conditional knockout allele by two novel approaches. Genesis (New York, NY : 2000) *30*, 1-6.

Yang, X., Fu, Y., Hu, F., Luo, X., Hu, J., and Wang, G. (2018). PIK3R3 regulates PPARα expression to stimulate fatty acid β-oxidation and decrease hepatosteatosis. Experimental & Molecular Medicine *50*, e431-e431.

Yoshioka, K., Yoshida, K., Cui, H., Wakayama, T., Takuwa, N., Okamoto, Y., Du, W., Qi, X., Asanuma, K., Sugihara, K., *et al.* (2012). Endothelial PI3K-C2alpha, a class II PI3K, has an essential role in angiogenesis and vascular barrier function. Nature medicine *18*, 1560-1569.